A New paradigm for Ultrasound-Based Tissue Typing in Prostate Cancer

by

Mehdi Moradi

A thesis submitted to the
School of Computing
in conformity with the requirements for
the degree of Doctor of Philosophy

Queen's University
Kingston, Ontario, Canada
September 2008

Copyright © Mehdi Moradi, 2008

Abstract

Prostate cancer is the most common malignancy among men. The gold standard clinical diagnosis method for prostate cancer is histopathologic analysis of biopsy samples acquired under ultrasound guidance. However, most prostate tumors lack visually distinct appearances on medical images. Therefore, pathologically significant cases of cancer can be missed during biopsy, resulting in false negative or repeated trials. The goal of our research is to augment ultrasound-guided prostate biopsy by adding tissue typing information that can be used for targeted biopsies. As a new paradigm in tissue typing, we hypothesize and demonstrate that if a specific location in tissue undergoes sequential interactions with ultrasound, the time series of echoes, which we call radiofrequency (RF) time series, would carry "tissue typing" information. We provide a potential physical explanation for this phenomenon and justify it based on computer simulations of the ultrasound probe and scattering media. We also report laboratory and animal studies that illustrate the utility of the method. We rely on a set of seven spectral and fractal features extracted from RF time series for tissue typing.

To show the clinical value of the proposed approach, we report an *ex-vivo* study involving 35 patients in which the utility of RF time series features for detection of prostate tumors is confirmed. The outcomes are validated using histopathologic

disease distribution maps provided for the studied specimen. We show that the RF time series features are powerful tissue typing parameters that result in an area under receiver operating characteristic (ROC) curve of 0.87 in 10-fold cross validation for diagnosis of prostate cancer. They are significantly more accurate and sensitive than spectral features extracted from single RF frames, and also B-scan texture features (area under ROC curve of 0.78 and 0.72, respectively). A combination of these three categories of features results in a feature vector that provides an area under ROC curve of 0.95 in 10-fold cross-validation and 0.82 in leave-one-patient-out cross validation for diagnosis of prostate cancer. Using this hybrid feature vector and support vector machines, we create cancer distribution probability maps that highlight areas of tissue with high risk of cancer.

Co-Authorship

Chapter 2 of this thesis is based on a survey paper published in co-authorship with my supervisors, Dr. Prang Abolmaesumi and Dr. Parvin Mousavi in *Ultrasound in Medicine and Biology* (July 2007). The survey has been updated with 2007 and early 2008 publications. Chapter 5 has been published in *Medical Image Computing and Computer Assisted Interventions 2007* and *SPIE Medical Imaging 2007*. Dr. Robert Siemens (Department of Urology, Queen's University), Dr. Eric Sauerbrei (Department of Diagnostic Radiology) and Dr. Alexander Boag (Department of Pathology and Molecular Medicine, Queen's University), along with my supervisors, are my co-authors on the *ex-vivo* human prostate study to appear in *Medical Image Computing and Computer-Assisted Interventions 2008* and accepted with minor revisions to *IEEE Transactions on Biomedical Engineering*.

Acknowledgments

I acknowledge the support of my true life heros, my parents, who came from modest backgrounds but gave their six children opportunities for prosperity and higher education.

I would like to thank my supervisors, Dr. Parvin Mousavi and Dr. Purang Abolmaesumi for their guidance, their scientific as well as personal support, and dedication to research. They have been my mentors in research and in life.

Ontario Graduate Scholarship (OGS), Precarn Incorporated and Queen's University (through the Duncan and Urlla Carmichael Fellowship) have funded my studies over the past four years. My research has also been funded through grants from Natural Sciences and Engineering Research Council of Canada (NSERC) and the Canadian Urological Association.

A number of faculty members and staff in different departments of Queen's Faculty of Health Sciences have had a significant role in my research. I would like to gratefully appreciate the contributions of Dr. Eric Sauerbrei (Diagnostic Radiology), Dr. Robert Siemens (Department of Urology), Dr. Alexander Boag, Dr. Philip Isotalo, Dr. Chris Davidson and Mr. Lloyd Kennedy (Department of Pathology and Molecular Medicine), Mr. Paul St John and Ms. Leone Ploeg from Human

Mobility Research Center. Within the School of Computing, I would like to specifically acknowledge Dr. Jonathan Boisvert, technical staff at the School of Computing (Tom, Ben, Richard, Gary and Dave), Debby Robertson and Wendy Bertrim. Among my friends, Amir Tahmasebi, Kathrin Tyryshkin, Thomas Chen, Hassan Shojania, Nooshin Kiarashi, Jean Mok, Pezhman Foroughi, Amaan Mehrabian, Bob Fraser, Amber Simpson, Hamidreza Saligheh-rad, Reh-Hui Gong, Maryam Salehi, Nazanin Aghaloo, Narges Ahmidi, Mehdi Hedjazi and Kathryn Duffy have helped me in my struggles over the years.

I genuinely feel sad for leaving my lab and the School of Computing here at Queen's and the beautiful city of Kingston. I will have a lot to miss, from our coffee times to the softball team, from our lovely Christmas parties to cross-country skiing, from CSCBC to CISC472, from Sandbanks to Frontenac Park, from Kingston waterfront to Market Square.

Finally I would like to thank Paria for her love and support and for always being there for me.

Statement of Originality

I, Mehdi Moradi, state that the research work presented in this thesis is my own and was conducted under the supervision of Dr. Parvin Mousavi and Dr. Purang Abolmaesumi. All references to the work of other researchers are properly cited.

I gratefully acknowledge the contributions of the clinical collaborators of this research: Dr. Alexander Boag, Dr. Philip Isotalo, Dr. Erick Sauerbrei and Dr. Robert Siemens.

Table of Contents

List of Tables

List of Figures

Glossary

A-mode Type of ultrasound scanning mode in which the amplitude of the signal is plotted versus the depth of the interface. The strength of the reflected echo is represented by the height of a spike [81].

ANOVA Analysis of variance. A statistical test aiming to find out whether data from several groups have a common mean.

Attenuation The decrease in the intensity in intensity as a sound beam travels through the medium. Attenuation depends on different mechanisms of interaction of ultrasound with tissue.

B-mode Brightness mode ultrasound scanning, which modulates the brightness of a dot to indicate the amplitude of the signal displayed at the location of the interface [81].

BPH Benign prostatic hyperplasia. Refers to the increase in size of the prostate in middle-aged and elderly men due to hyperplasia.

Carcinoma A malignancy neoplasm that arises from epithelial cells [114].

DRE Digital rectal examination. A clinical test to diagnose prostate cancer during which, the physician touches the prostate of the patient with fingers.

The cancerous prostate tissue is known to be stiffer than normal tissue; therefore, the physician tries to determine if the tissue is unusually hard.

Epithelium Epithelium is a tissue composed of layers of cells that line the cavities and surfaces of structures throughout the body. It is also the type of tissue of which many glands are formed.

Ex-vivo Latin: Out of the living. It refers to experiments and measurements performed on living tissue in an environment outside the body.

FWHM Full Width at Half Maximum. The full width at half maximum (FWHM) is a parameter commonly used to describe the width of a bump on a curve or function. It is given by the distance between points on the curve at which the function reaches half its maximum value [Mathworld]. As a tissue typing feature extracted from B-scan ultrasound images, FWHM is measured by identifying the points on the image histogram which are half the maximum value.

Hyperechoic Characterization of relatively strong echoes created in ultrasound images compared with nearby regions [81].

Hyperplasia A general term referring to the proliferation of cells within an organ or tissue beyond the ordinarily levels. Hyperplasia may result in the gross enlargement of an organ.

Hypoechoic Characterization of relatively weak echoes created in ultrasound images compared with nearby regions [81].

In-vivo Latin: within the living. Refers to something which takes place inside an organism. In-vivo refers to experimentation done in or on the living tissue of a whole, living organism as opposed to a partial or dead one or a controlled environment.

Neoplasia The abnormal proliferation of cells, resulting in a neoplasm. Neoplasia is the scientific term for the group of diseases commonly called tumor or cancer.

PCA Principal component analysis. A vector space transform often used to reduce multidimensional data sets to lower dimensions for visualization and analysis [13].

PIN Prostatic intraepithelial neoplasia. A non-cancerous condition that occurs when the cells that line the ducts of the prostate change. PIN is frequently observed in coexistence with carcinoma, therefore, it is considered a probable precursor to carcinoma of prostate [114].

PSA Prostate specific antigen. A protein produced by the cells of the prostate gland. PSA is present in small quantities in the serum of normal men, and is often elevated in the presence of prostate cancer and in other prostate disorders. A blood test to measure PSA is a test currently available for the early detection of prostate cancer.

RBF Radial basis function. A real valued function whose value at each point depends only on the distance of that point from a specific center point.

RF signals Radiofrequency signals. In this thesis, it refers to the signals received in

the ultrasound probe. The frequency of ultrasound in clinical applications falls within the range of radiofrequency electromagnetic signals. Although ultrasound is a mechanical wave and fundamentally different from electromagnetic waves, the transducer transforms the mechanical wave to an electrical signal in the RF range of frequency.

RF time series The sequence of one sample of one ultrasound RF scan line over time forms an RF time series. To acquire the RF time series, one keeps the ultrasound probe and the tissue fixed in place and continues acquiring frames of RF data at the frame rate of the ultrasound machine.

ROC curve Receiver Operating Characteristic curve. A plot of sensitivity versus specificity or probability of false alarm for different values of the decision threshold in a classification method. ROC curves can be used to compare the diagnostic performance of diagnostic tests.

ROI Region of Interest. A rectangular area in the B-scan or RF data space that is represented with tissue typing features and is classified into one of possible tissue categories.

Scattering The redirection of sound energy resulting from the sound beam striking an interface whose physical dimension is less than the wavelength.

Sensitivity In a classification test, specificity measures the proportion of negatives which are correctly identified.

SNR Signal to Noise Ratio. In general, the ratio of signal power to noise power. As a tissue typing feature extracted from B-scan ultrasound images, SNR

is computed as the ratio of speckle mean to standard deviation.

Specificity In a classfication test, specificity measures the proportion of negatives which are correctly identified.

SVM Support vector machine. A classification method that falls within the category of maximum margin classifiers.

TGC Time gain control. A method of increasing amplification of the ultrasound signal with depth to compensate for loss caused by attenuation.

TRUS Transrectal ultrasound. Diagnostic imaging of prostate through rectum.

Chapter 1

Introduction

1.1 Motivation

Prostate Cancer (PCa) is the most common malignancy among men and the second leading cancer-related cause of death after lung cancer [92]. Prostate is an accessory gland in the urinary and reproductive system of the male. It is located deep in the pelvis, just below the bladder. In a mature male, prostate is cone shaped and weighs approximately $12 - 20\ gr$. For detailed information on the anatomy and possible disease of prostate see [32, 173].

Prostate cancer accounted for 29% of cancer cases among North American men and terminated the lives of 31,350 of them in 2007 [93]. The Canadian Cancer Society estimates that 24,700 new cases of PCa will be diagnosed among male Canadians in 2008, leaving it as the most prevalent type of cancer among men [21]. PCa is also the most prevalent type of cancer in male Europeans and affects over 237,000 men in 40 European countries annually [16].

Despite its prevalence, PCa is a curable condition in many cases. In Canada for

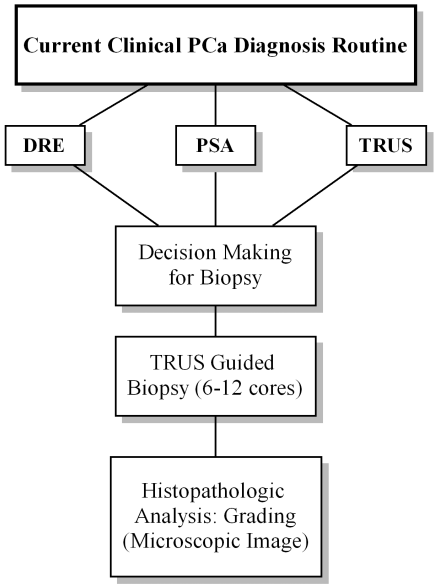

Figure 1.1: The current clinical approach for detection and grading of PCa.

example, the five-year survival rate of prostate cancer for men between the ages of 50-79 is 96% [21]. Mortality often happens when patients are affected by metastasis of the cancer to bones. At that stage, surgical and hormonal treatments are not very effective. Therefore, the early diagnosis and staging of the disease play an important role in the choice and the success of the treatment. The currently available treatments, including brachytherapy, prostatectomy, hormone therapy and chemotherapy result in different degrees of side effects, especially incontinence and impotence. Therefore, it is important to choose a treatment option that maximizes the likelihood of success while minimizing the side effects.

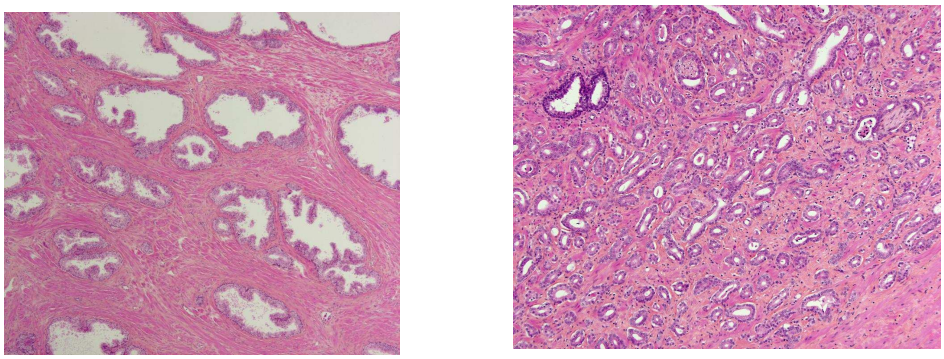

Figure 1.2: Typical microscopic histopathology images of prostate tissue illustrating normal prostate (left), and prostatic carcinoma (right).

The process of screening and diagnosis of prostate cancer is far from a perfect procedure (Figure 1.1). Immunoassay-based measurement of the blood levels of Prostate Specific Antigen (PSA: a glycoprotein produced almost exclusively in the epithelium of the prostate gland) is commonly accepted as the first step in screening of prostate cancer. The case for a public screening process has been a topic of discussion since the early 90's when the PSA test was introduced [188]. PSA test is prone to both false positives and false negatives. Sceptics believe that false positive outcomes of PSA are too high and result in unnecessary and more invasive follow-up procedures such as biopsy. Some suggest that in general, public screening with PSA test results in over-diagnosis of PCa and, hence, in surgical or brachytherapy treatments in cases of prostate cancer that should not be treated due to their non-aggressive and chronic nature [233].

On the other hand, PSA results in false negative outcomes as well. While serum PSA levels of over 4 ng/ml are normally associated with high risk of PCa[1], studies

[1]More precisely, the threshold is 3.5 ng/ml for men in their 50's, 4.5 ng/ml for men in their 60's

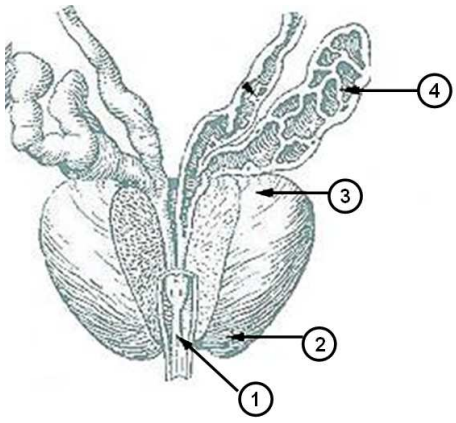

Figure 1.3: Anterior view of the left and the right lobes of the prostate gland. 1) Urethra, 2) apex of the prostate, 3) base of the prostate, 4) seminal vesicles. Picture taken with permission from http://www.celtnet.org.uk /cancer/prostate-cancer.html.

have shown that certain populations of men with lower levels of PSA share the same risk level [36, 187]. PSA tests are often accompanied with detection by palpation through digital rectal examination (DRE). DRE test is based on the clinical fact that the cancerous tissue is stiffer than normal prostate tissue. DRE is limited to relatively large and superficial lesions [108].

Given all the limitations of the non-invasive diagnostic tests, the current "gold standard" for PCa diagnosis is histopathologic analysis of biopsy tissue samples (Figure 1.2) under Transrectal Ultrasound (TRUS). During biopsy, a radiologist extracts core samples of prostatic tissue using a needle guided to prostate under ultrasound imaging. The most common prostate biopsy protocol is the sextant systematic approach proposed in 1989 [84]. The sextant protocol involves taking tissue samples from the apex (inferior portion), the midsection, and the base (superior portion) of the left and the right lobes of prostate (See Figure 1.3). Several studies have shown

and 6.5 ng/ml for men in their 70's [21].

that this protocol is prone to missing cancer in many patients. Therefore, different variations of the sextant biopsy have been suggested in which the number of cores is increased to 10, 12 or even 18 [200].

Unfortunately, even the invasive biopsy operation is not a perfect diagnostic tool. Biopsy is a sampling process and due to the multifocal nature of PCa, there is always some level of risk for missing pathologically significant lesions resulting in false negatives and/or repeated biopsies [176]. Different studies have estimated the sensitivity of TRUS-guided needle biopsies to be between 40% and 60% [42, 154] showing that almost half of cancer cases are missed on the first biopsy. This low sensitivity is partly due to the fact that most prostate tumors lack visually distinct appearances on ultrasound images that are used for the guidance of the biopsy process. While the hypoechoic lesions in ultrasound images are generally attributed to cancer in prostate, studies have shown that only 40% of the peripheral zone hypoechoic lesions prove malignant [193]. Furthermore, isoechoic and even hyperechoic tumors have been observed [88]. Therefore, the clinical value of TRUS is limited to an anatomical guidance tool [2]. As a result, the rate of false negative outcomes in prostate biopsy is high and a large number of men have to go through repeated biopsies.

1.2 Objective

We argued that improving the biopsy process is a pressing need. Ideally, this should be done with minimal overhead imposed on the routine clinical biopsy process. Since

[2]Studies have shown that using Magnetic Resonance Imaging (MRI) as the guidance tool for prostate biopsies does not effectively change the sensitivity of the process [104, 236].

ultrasound imaging is currently an integrated part of the biopsy process, an enhancement to this process based on ultrasound imaging is preferable. Furthermore, ultrasound is an inexpensive imaging modality that does not expose the patient or the radiologist to ionizing radiation and produces real-time images. The goal of the research described in this thesis is to enhance the TRUS-guided biopsy process. Our approach to achieve this goal is to augment ultrasound images with tissue typing information that can be used for cancer detection and targeting during biopsy. Previous research has shown that although visual inspection of B-scan ultrasound images is not sensitive for cancer diagnosis, computer-based approaches can improve the outcomes. Such approaches take advantage of texture analysis of B-scan images and more importantly, rely on the analysis of raw RF ultrasound signals [55, 128]. However, the available techniques are not accurate enough and lack a widespread clinical acceptance [53].

In this thesis, we propose a novel approach to acquire and analyze ultrasound RF signals for tissue typing. We extensively evaluate this approach through simulation, and on phantom and animal studies and show its feasibility. We also report a clinical study that shows the promising outcomes of the proposed method, for diagnosis of cancer in human prostate tissue.

1.3 Hypothesis

We introduce a new paradigm in ultrasound tissue typing which is based on the concept of "RF time series". An RF time series is formed by the sequence of RF echoes received from one location in the tissue over time. To acquire the RF time series, one keeps the ultrasound probe and the tissue fixed in place and acquires

frames of RF data at the frame rate of the ultrasound machine. We hypothesize that if a specific location in tissue undergoes sequential interactions with ultrasound at the typical clinical ultrasound frame rates, the sequence of RF echoes from that location, the RF time series, would carry tissue typing information. We use this information to enhance the TRUS-guided prostate biopsy process.

A "potential" physical explanation for the existence of the tissue-type dependent information in RF time series will be discussed and examined through simulations in Chapter 3. However, throughout the thesis, we will follow a primarily experimental approach to validate the hypothesis described here.

1.4 Contributions

The major contributions of the thesis are as follows. This thesis:

- Introduces the concept of the RF time series for the first time and provides analytical methods to extract efficient tissue typing parameters from the RF time series.
- Provides a potential explanation for the existence of tissue-type related information in the ultrasound RF time series. Computer simulations of ultrasound probes and scattering media provide evidence to support this explanation.
- Introduces six parameters extracted from frequency spectrum of ultrasound RF time series for tissue typing. It also shows that fractal dimension of RF time series can be used for tissue typing.
- Describes phantom and animal tissue typing experiments. The phantom studies

aim at proving the relationship between cellular microstructure and the RF time series. In animal tissue typing experiments, RF time series acquired both using a clinical ultrasound machine and a high-frequency machine operating at 55 MHz are studied.

- Reports an *ex-vivo* clinical study involving 35 patients in which the performance of the RF time series features for detection of prostate cancer has been evaluated. Also, the thesis reports quantitative comparisons between the accuracy of detection of prostate cancer using the RF time series features and the classical ultrasound-based tissue typing features proposed by Lizzi and Feleppa [55, 130]. Detailed histopathological analysis of the studied prostate specimens is used as the gold standard.

- Presents cancer distribution probability maps acquired using a combination of the time series features with B-scan texture and Lizzi-Feleppa features along with Support Vector Machine (SVM) classification.

- Reports experimental studies that characterize the effects of parameters such as the acoustic power of ultrasound, the depth of imaging and the ultrasound acquisition frame rate on the effectiveness of detection of prostate cancer based on the RF time series features.

1.5 Organization of the thesis

In this chapter, we presented the research problem studied in this thesis and discussed the importance of developing a computer-based methodology to enhance the TRUS-guided prostate biopsy. Additionally, we listed the contributions of the thesis. The

remaining chapters of the thesis are organized as follows:

- Chapter 2 reviews the state of the art in computer-aided diagnosis of prostate cancer. Ultrasound-based cancer diagnosis methods are reviewed in more detail. Several other approaches and trends in diagnosis of prostate cancer based on magnetic resonance imaging, elastography, and automatic analysis of microscopic histopathology images of prostate tissue are also discussed.

- Chapter 3 introduces the concept of RF time series, provides a potential physical explanation for the existence of tissue-type related information in RF time series and presents our simulation study.

- Chapter 4 describes the tissue typing features proposed based on RF time series. This chapter also provides information on the classification approaches utilized in the thesis.

- Chapter 5 describes our phantom and animal studies.

- Chapter 6 describes our clinical study involving 35 patients. The chapter describes methods developed for generation of probabilistic maps of prostate cancer based on RF time series, and the steps taken to validate the outcomes of the study based on histopathologic analysis of prostate specimens. The effects of imaging depth, acoustic power of the ultrasound, and frame rate on the outcomes are analyzed.

- Chapter 7 provides the summary and conclusions of the thesis along with a discussion of the limitations and the future work.

It should be noted that the order of presentation of experiments in this thesis does not match the chronological order in which the experiments were carried out. The research started in 2005 with a preliminary human study involving four patients. The experiments continued throughout 2006 with animal tissues. Data collection and analysis for the larger human study involving 35 patients were performed in 2007. The phantom studies were carried out in 2008.

Chapter 2

Review of the related work

This chapter reviews the state of the art in computer-aided diagnosis of prostate cancer and focuses, in particular, on ultrasound-based techniques. We provide a general overview of several image-based techniques for detection and grading of prostate cancer. Further, in accordance with the topic of this thesis, we provide an in-depth review of ultrasound-based methods. We review numerous studies in which ultrasound Radio Frequency (RF) signals, B-scan images and Doppler images have been used for computer-aided diagnosis of the disease. In recent years, computer-aided diagnosis and treatment of prostate cancer have been very active fields of research. The reader is encouraged to consult survey papers by Moradi *et al.* [143] and Zhu *et al.* [240] for further exploration of the field. Through the analysis of the vast array of methods proposed in the literature, we intend to demonstrate that the ultrasound-based methods are among the most cost-effective and promising approaches for detection of prostate cancer. At the same time, shortcomings of all the computer-assisted methods, including those based on ultrasound, justify continued research in the field.

It should be noted that computer-aided diagnosis systems are designed to provide

a second opinion and are not to replace the opinion of physicians. This general rule applies to prostate cancer as well. The prevalence of false negatives in diagnosis of prostate cancer implies that a second opinion can be very valuable. If this assisting opinion becomes available during the biopsy process, it gives the radiologist an upper hand in selecting the biopsy sites.

2.1 Overview of image-based methods for diagnosis of prostate cancer

The task of categorizing computer-aided PCa detection techniques is non-trivial. We provide a review of image-based techniques for detection of PCa in this section. We will continue in Section 2.2 with ultrasound-based methods as the main focus of the current thesis.

2.1.1 Magnetic Resonance Imaging (MRI)

There have been attempts to use imaging modalities such as MRI and CT scan for diagnosis of prostate cancer[1]. MRI, in particular, has received the attention of researchers based on the premise that localizing prostate tumors with endorectal MRI could be more accurate than localizing such tumors with ultrasound [163]. Some of the main approaches to utilize MRI imaging in computer-aided diagnosis of prostate cancer are introduced in this section.

[1]CT scan is usually used as a post-diagnosis method for finding possible metastases to abdominal cavity, bones and lymph nodes; however, the application of CT scan has not resulted in superior detection outcomes (compared to ultrasound) during prostate biopsy [168]. CT scan has also been used for brachytherapy treatment planning and post-implant dosimetric analysis [169]. Although there have been reports on using Positron Emission Tomography in prostate cancer diagnosis [181], the role of PET has yet to be defined [195].

MRI provides superior anatomical image quality compared to ultrasound imaging. This results in more accurate boundary delineations and 3D model generation of the organ under study which can be used to compute the volume of prostate and to plan radiotherapeutic treatments. Rasch *et al.* [172] have described the methodology of volume determination using MRI scans. It should be noted that dynamic contrast-enhanced magnetic resonance imaging of the prostate tumor is also used to study the tissue perfusion and to image prostate carcinoma [19, 125]. Nowrolski *et al.* have reported that cancer regions in peripheral zone of prostate can be distinguished from normal regions using dynamic contrast enhanced MRI [153].

MRI has been used as an imaging modality for guidance during prostate biopsy [26, 30, 80, 229]. Hata *et al.* have reported a comprehensive study on using T2-weighted MR images acquired from a 0.5 T intraoperative MR system to guide placement of biopsy needles in both suspected targets and sextant location in the peripheral zone of the prostate [80]. The mismatch in needle placement in their study (reported both on validation phantoms and on two clinical cases) has been less than 1.9 mm (the error is mainly due to the deflection of needle in the soft tissue). Kaplan *et al.* [100] have also used TRUS as the intraoperative image modality and MRI as the preoperative modality for prostate biopsy procedures. In their study, MRI image sets were registered to the ultrasound images in real time during the biopsy. Kaplan *et al.* used a hardware setting similar to the hardware utilized for brachytherapy implant procedure [99] and stereotactically targeted the abnormal areas of the tissue as identified on MRI images. More recently, a remotely actuated manipulator for accessing the prostate tissue under magnetic resonance imaging guidance was introduced [62, 112]. The designers of this system have reportedly overcome the engineering challenges

imposed by the high intensity magnetic field inside the MRI machine (ferromagnetic materials and electronic devices are not allowed to be in the magnet). The details of software interface for visualization, planning, and monitoring of this MRI-based robot for prostate biopsy

Contrary to the technical achievements in MRI-based prostate interventions, most clinicians still believe that MRI images do not effectively change the level of accuracy of the diagnosis process [104]. Some of the studies acknowledge this impression: The accuracy, sensitivity, and positive predictive value of MRI for detecting tumor foci greater than 1 *cm* in diameter has been reported to be 79.8%, 85.3%, and 92.6%, respectively, in a recent study [148]. However, based on the same work, the corresponding values for detecting tumor foci smaller than 1 *cm* decreased to 24.2%, 26.2%, and 75.9%, respectively. This suggests that MRI is more useful for detection of presence, size, and possible extension of cancer foci greater than 1 *cm* in diameter. Another interesting study, by Madabhushi *et al.*, provides some insight into usefulness of MRI in detection of prostate cancer [134]. The authors have performed a comprehensive study using 35 3D texture features extracted from high resolution (4T) MRI to identify cancer tumors in prostate tissue. The authors' best reported sensitivity is in the range of 40-50% which is superior to the sensitivity of diagnosis by an expert reported on the same dataset; however, inadequate as a clinically feasible system[2]. In a very recent work, an unsupervised segmentation method has been presented by Viswanatha *et al.,* which "employs manifold learning via consensus schemes for detection of cancerous regions" from high resolution 1.5 T endorectal *in-vivo* prostate MRI [219]. Evaluation on 18 patents has resulted in sensitivity of 92.7% and specificity of

[2]It should be noted that Madabhushi *et al.* have aimed at classifying single sub-millimeter voxels in cancerous and normal classes and have acquired very high values of specificity.

82.1%.

The time complexity of MRI-based prostate cancer diagnosis systems should also be taken into consideration. Particularly, in 3D systems, the computation time for analysis of one complete MRI scan exceeds an hour [134]. The application of MRI as a routine diagnostic procedure for PCa is also restricted by its high cost. As we will discuss in upcoming sections of this chapter, ultrasound scans provide the same level of diagnostic value as MRI with significantly lower cost.

An alternative imaging modality based on magnetic resonance which is widely utilized for prostate cancer detection is Magnetic Resonance Spectroscopy (MRS). It has been shown that prostate gland is a unique organ in human body by having a high level of citrate. In the mid 90's, a correlation between water T_2 relaxation time and citrate concentration in the normal prostate was demonstrated [124]. Furthermore, a proven negative correlation between neoplasia and citrate level in prostate is well documented [28]. A strong positive correlation between choline level and prostate cancer is also reported [203]. Based on these facts, many researchers have undertaken studies on the use of MRS to detect metabolic biomarkers (mainly choline and citrate) for characterizing prostate tissue [67, 115, 146]. The analysis of the MRS data to automatically identify likely cancerous areas of prostate is the topic of a few studies [209]. A few investigators have studied prostate cancer through registering the MRS signals to MRI anatomic images; they have validated correlations between cancer characterizing patterns in the signals, biopsy outcomes and texture in the images [105, 153]. Van Dorsten *et al.* have tried to differentiate prostate carcinoma from healthy peripheral zone and central gland using quantitative dynamic contrast-enhanced magnetic resonance (MR) imaging and two-dimensional MRS combined

into one clinical protocol [214]. Their results are in agreement with [28] and show that a combination of high-resolution dynamic MRI and metabolic information from MRS has the potential for improved diagnosis of prostate cancer.

In a recent study, Feleppa *et al.* have reported combining MRS and ultrasound for detection of prostate cancer [53]. They have used the ratio of choline to citrate concentrations acquired through MRS along with RF spectrum features extracted from ultrasound (see Section 2.2) for tissue typing. Reportedly, the area under the receiver operating characteristic (ROC) curve acquired from the MRS-based method increased from 0.64 to 0.84 after addition of the ultrasound-based features [52].

Before we close our discussion on MRI-based methods, it should be noted that currently MRI-based techniques are in use for PCa computer-aided treatment procedures such as: MRI-guided radio-frequency thermal ablation of PCa [50, 51], planning of the radiotherapy treatment and quality control of the correct placement of radioactive seeds in prostate brachytherapy (post-implant dosimetric analysis) [169, 202, 215]. Therapeutic methods are beyond the scope of the present survey.

2.1.2 Ultrasound

In ultrasound imaging, tissue typing based on the acoustic parameters such as attenuation and backscattering coefficients extracted from RF echo signals has been studied since the early 70's (see [130] for a review). Texture features extracted from B-scan ultrasound images also account for an important category of parameters used for cancer detection. Furthermore, the proven correlation of neovascularity with cancer generation has impelled investigators to use features extracted from ultrasound

color Doppler images for tissue typing. All these ultrasound-based tissue typing approaches have been applied to prostate cancer detection. The advantages of having an ultrasound-based PCa detection system are encouraging enough to boost this field of study: ultrasound provides real-time images; TRUS is already accepted as the standard prostate biopsy guidance tool; different ultrasound data and image modalities are simultaneously available on modern ultrasound machines; and ultrasound imaging is among the most accessible and least harmful medical imaging systems. The disadvantages of ultrasound imaging include low contrast and existence of speckle in the images. As ultrasound-based methods for detection of prostate cancer are the main focus of the current thesis, Sections 2.2 and 2.3 will focus on RF, B-scan and Doppler techniques applied to PCa detection. We will present the accuracies of prostate cancer detection reported in different studies and show that they are comparable to the accuracies acquired using MR imaging as discussed in this section.

Another category of studies focuses mainly on the application of ultrasound as a guidance technique for biopsy. Robotic techniques based on 3D ultrasound imaging form a major trend in such studies. One such system is developed by Tong *et al.* and consists of a standard 2D TRUS probe equipped with a motor driven mechanism that rapidly acquires 2D B-mode images and reconstructs a 3D model [210]. In 3D ultrasound imaging, there is always a compromise between the size of the dataset (which is in direct relationship with the information made available for diagnosis) and technical challenges for volume reconstruction and visualization [38]. However, with the recent developments of the 3D ultrasound systems, near real-time views of the anatomy are available [61]. Based on such systems, investigators have designed robotic systems for

targeted prostate biopsy or placement of radioactive seeds for brachytherapy treatments with sub-millimeter accuracy [221]. More recently, Fichtinger *et al.* [63] have reported a robotically assisted prostate brachytherapy system that consists of transrectal ultrasound, and a spatially registered robot integrated with an FDA-approved commercial treatment planning system.

Tissue motion and deformation create serious challenges for image-based guidance of the biopsy process. Under current biopsy protocols, it is almost impossible to track the biopsy samples back to their exact location for quality control or targeted repeated biopsies. To overcome this limitation, Baumann *et al.* proposed a 3D TRUS-based tracking system for precise prostate biopsy sample localization [10]. Their method is based on the fact that the probe motion range is large and is constrained only by rectum walls, and therefore, the initial alignment needed to solve the registration problem (from a given reference space to the tracking space during biopsy) might have to estimate rigid transformations that are beyond the capture range of simple image similarity measures. They propose a multiresolution attribute-vector registration approach that combines global and local optimization methods to solve this problem. They report successful convergence of the 3D-3D registration approach in 96% of cases with an accuracy of 1.41 mm.

2.1.3 Elastography

An alternative ultrasound-based method for cancer detection is "elastography". Alterations in the elastic properties of the tissue are indicators of the prostate malignancy and are normally examined by digital palpation (DRE test). Elastography,

"palpation by imaging" and "strain imaging" are different names for automatic techniques aiming at depicting the elastic properties of the tissue [66] in search for pathologic areas. Ophir *et al.* [158] described elastography as a technique for quantitative imaging of elastic properties of tissue from its strain profile computed through comparison of locations of peaks in ultrasound RF echo signals before and after applying an external compression. The comparison is made by cross-correlation analysis of corresponding pairs of RF A-lines (one acquired before and one after compression). In case of prostate elastography, the compression can be applied manually by a hand-held transrectal probe [133]. The resulting system is an automated version of the DRE test which extends the elastic analysis of the tissue to non-superficial lesions[3]. One disadvantage of the correlation-based technique for strain estimation in elastography is its computational complexity. Pesavento and Lorenz *et al.* introduced an algorithm for real-time and accurate strain estimation that relies on phase differences of the corresponding pairs of RF signals [133, 164].

In a study published in 1998, Fatemi and Greenleaf [49] showed that the tissue motion caused by ultrasound radiation force can be used for measuring the acoustic response of material to mechanical excitation. Interfering focused beams of ultrasound were used to create the mechanical response from the tissue. In a more recent study, the same group described a methodology in which the radiation force of ultrasound is used to scan the object at a resonant frequency. The vibration of the object is measured by laser and the resulting acoustic emission from the object is measured by a hydrophone. Although the experimental results of [238] are reported on a mechanical heart valve and arterial phantom, they confirm the possibility of creating mechanical

[3]An MRI-based technique known as magnetic resonance elastography also measures the propagation of acoustic strain waves in tissue subjected to mechanical excitation. For information on that technique and its potential application in detecting prostate cancer see [113, 137].

excitation and microscopic vibrations in response to ultrasound emission.

Salcudean *et al.* have recently reported a vibro-elastography system specifically designed to study the mechanical properties of prostate tissue [179]. Their system integrates the TRUS transducer with an actuation system that can apply low-frequency ($< 20\ Hz$) vibrations to the tissue. With the assumption that the response of the tissue to excitation is linear, they have applied mechanical frequencies up to 20 Hz to the tissue and have estimated tissue mechanical frequency responses (transfer functions). They have shown that for more than 80% of their computed transfer functions, the coherency over the frequencies of excitation is at least 0.9 which is a sign of high signal to noise ratio and linearity.

In another recent study, Courtis and Samani [29] proposed an elastography method based on finite element registration. The technique requires two 3D TRUS volumes: a baseline volume, and a second volume in which the US probe is displaced vertically to deform the prostate. Then a finite element model of the prostate, tumor, rectum, TRUS probe, and surrounding tissue is used to simulate the deformation induced by the probe. Results from their phantom study showed that the technique could detect the increased stiffness of the simulated tumor.

In recent years, significant improvements in computational and engineering methods employed for elastography have been reported [22, 25, 43, 120, 140, 147, 159, 162, 174]. Elastography is proved to be a valuable tool for tissue typing and is currently under study either as an independent tool [4] or in combination with 3D imaging for PCa detection [122]. However, the restricted value of signal to noise, frequent cases of multi-focal and very small cancer loci in prostate malignancies, high computational cost of the method that restricts its real-time application, and relatively complicated

settings of the method have restricted its applicability in daily clinical procedures. In particular, the prostate anatomy restricts investigators' control over the accuracy of the compression applied during the procedure, and implies the need for more reproducible compression techniques [89, 133]. This problem was initially tackled by Omata and Constantinous using a bio-sensor for *in-vivo* evaluation of prostatic stiffness [156]. Slightly different versions of this tactile sensor have been fabricated and used to evaluate the elasticity of prostate and other tissue types *in-vivo* and *ex-vivo* in animal studies [120, 147]. Recently, there have been reports on the utilization of magnetically induced motion for imaging prostate tissue after implanting brachytherapy radioactive seeds [140].

2.1.4 Microscopic histopathology images

Studying the histopathology of the biopsy samples is the means for reporting the presence and the grade of prostate cancer. Higher grade (more aggressive) lesions correspond to highly irregular cellular networks in tissue. The commonly accepted grading system for PCa is Gleason grade [32] that suggests a ten grade system based on the appearance of processed tissue samples. Therefore, grading is dependent upon the subjective and time consuming procedure of microscopic analysis of the level of irregularity in the cellular structure of the tissue.

Automation of the histopathologic analysis of microscopic images of tissue has engaged many researchers in image processing and computer vision fields. Based on a number of shape and texture features of the microscopic image, Stotzka *et al.* have used neural networks to distinguish the moderately and poorly differentiated lesions of prostate tissues [201]. Shape and texture features combined with neural networks

[8], similarity measurement methods [198] and multi-wavelet features combined with K-Nearest Neighbor (K-NN) classifiers [90] have been applied to automatic grading of prostate biopsy samples. Tabesh *et al.* combined linear and quadratic Gaussian classifiers with color channel histogram, and fractal and wavelet-based features to grade pathologic samples [204]. Farjem *et al.* have devised a tree-structured grading algorithm that uses roundness and shape distribution features in addition to texture features for classification of cancerous glands [48]. In the recent studies on automatic grading of pathologic prostate cancer tissues, classification accuracies of up to 95% have been reported [204, 48]. Doyle *et al.* have suggested exploiting multiple image scales to extract up to 600 texture features for automatic pathological typing [40] of prostate tissue. The authors have shown that their multi-scale approach results in very high performances based on ROC analysis (ROC curves are provided, but the authors have not reported the value of the area under the ROC curve). More recently, utilizing architectural and textural image features with Support Vector Machine (SVM) classification, Doyle *et al.* reported accuracies between 76% and 92% in distinguishing different grades of prostate cancer from each other and from normal prostate tissue types [39].

Histopathologic analysis of microscopic images of prostate tissue is labor-intensive; as a result, providing the pathologists with a computer-aided diagnosis as a "second opinion" can be valuable. We were unable to find any reports on a commercial software implemented and in use for histopathologic grading of prostate tissue.

It should be added that different researchers have used the results of histopathologic analysis of large populations of prostate cancer patients to generate *statistical atlases* of distribution of the disease. Biopsy protocols can be adjusted based on the

findings of such studies to increase the sensitivity of the procedure. Sofer *et al.* have constructed a statistical distribution map of cancer using the prostate tissue of 301 patients. The removed prostates were sectioned at 2.25 mm intervals and scanned to generate digital image files. 3D reconstruction of prostates based on these slices were combined with histopathology results. The researchers designed a biopsy protocol to maximize the likelihood of targeting cancer tissues based on these statistical maps and acquired significantly higher detection rates than protocols currently used clinically [199]. Shen *et al.* have also generated a 3D statistical atlas of the distribution of prostate cancer lesions in large populations of patients [190, 191]. This atlas has been used for selecting biopsy sites in a separate group of patients with an accuracy of 99% in finding the cancerous lesions. In a recent publication, Zhan *et al.* also reported a study in which statistical atlases have been used to optimize the biopsy process [237]. In their approach, first, a statistical atlas of the spatial distribution of prostate cancer is constructed from histological images. Then, a probabilistic optimization framework is employed to optimize the biopsy strategy. Finally, the optimized biopsy strategy generated in the atlas space is mapped to a specific patient space using an automated segmentation and deformable registration method. Zhan *et al.* reported that the predictive power of the optimized biopsy strategy for cancer detection reached to 94% – 96% for 67 biopsy cores.

2.1.5 Section summary and discussion

In this section, we reviewed several image-based solutions to tackle the problem of localizing prostate cancer lesions. Recently, there has been more interest towards using MR images both for characterizing prostate tissue and guidance during biopsy.

MRI provides higher quality in depicting the anatomy (compared to ultrasound), and MR spectroscopy reveals the concentration levels of choline and citrate which are important biomarkers for prostate cancer. Researchers have developed solutions to the engineering challenges posed by strong magnetic fields within MRI machines to build automatic biopsy targeting systems [62, 80, 112], and also proposed effective feature extraction and classification approaches for prostate tissue typing from MR images [134].

Due to its numerous clinical advantages, ultrasound is still the main imaging modality for prostate cancer diagnosis. Among these advantages are the inexpensive and versatile process of ultrasound scanning, real-time image formation and non-ionizing nature of ultrasound. Most importantly, the diagnostic value of ultrasound is not inferior to MRI [236].

However, it should be noted that one does not find a consensus in the literature on the performance of ultrasound or MRI in detection of prostate cancer. The reported values for accuracy and sensitivity of these diagnostic methods vary in different studies. Schiebler *et al.* have summarized the results of some clinical studies that use MRI for finding prostate cancer [185]. In two cases, the datasets have been studied both with MRI and ultrasound. In both cases, the sensitivity of diagnosis by the radiologist is around 10% higher when MRI has been used[4].

The size of region of interest (ROI), or equivalently the resolution of diagnosis influences the results. For example, the study by Schiebler *et al.* suggests that it is easy to visualize tumors as small as $3mm^3$ in MRI[5] [185]. Madabhushi *et al.* have

[4]According to [185], in a large study with around 219 patients involved, the sensitivity values were 77% and 66%, respectively, for MRI and ultrasound.

[5]This is in contradiction with [148] which concludes the performance of MRI significantly reduces for tumor sizes smaller than 1 cm in diameter.

suggested that it is impossible to visualize lesions of size smaller than $5 - 6\ mm^3$ using ultrasound [134].

Accuracy and sensitivity are not the only factors for comparing ultrasound and MRI-based techniques. Cost and time-complexity also need to be considered and ultrasound is superior in these aspects. While the high resolution MRI-based tissue classification results reviewed in this section are acquired on 4 T MRI machines with over an hour of computation time, the ultrasound-based methods hardly add any hardware overhead to the clinical routines and are performed in near real-time fashion (Section 2.2).

To summarize, most researchers believe that in experienced hands, the most accurate *imaging* test for primary staging of the disease is MRI using an endorectal coil [181, 230]. Nevertheless, according to different studies, the sensitivity of local staging of prostate cancer with MRI ranges between 37% and 77% [134, 185, 230]. The recently proposed computer-based diagnosis systems have been successful in providing similar levels of performance from MRI [134] and also from ultrasound [55, 182, 236]. In other words, image-based methods can facilitate and enhance the diagnostic process by providing a "second diagnostic opinion" to the physician. Nevertheless, the "second opinion" provided by computer-aided analysis of medical images is not accurate enough to gain the clinical acceptance (and replace the biopsy and histopathology process).

Based on our brief review of strain-imaging and elastography techniques, it appears that ultrasound-based elastography is gaining more popularity among researchers.

Most of the older versions of elastography were based on quasi-static and/or manual compression of tissue. Therefore, the images were operator dependent and non-reproducible. Advances in the fabrication of compression and vibration inducing systems integrated with the ultrasound probes have advanced elastography [147, 175, 179, 238].

We close our discussion with reminding the readers that computer-aided techniques for detection of prostate cancer are not limited to the image-based methods introduced in this section. As mentioned earlier, the present survey is not aimed at covering all PCa detection techniques reported in the literature. We have presented a brief review of the image-based techniques in this section, and will focus specifically on ultrasound-based tissue typing methods applied to diagnosis of prostate cancer in the remainder of this chapter. The reader is also encouraged to consider DNA microarray-based gene expression analysis of prostate tissue which has led to suggesting specific sets of genes as biomarkers of prostate cancer [33, 118, 119, 196, 225], analysis of protein profiles associated with PCa [3], and bioimpendence-based methods that take advantage of the tissue conductivity reduction with formation of cancer [98, 197]. These techniques are beyond the scope of the present survey.

2.2 Ultrasound-based methods for diagnosis of prostate cancer

Ultrasound-based prostate tissue typing was introduced in the previous section as a potential technique to improve the accuracy of the biopsy process and ultimately to eliminate the need for histopathologic analysis. In this section, we present the

fundamentals of tissue typing based on ultrasound RF echo signals (Section 2.2.1) and B-scan images (Section 2.2.2) and review the studies that have used RF and B-scan based features for prostate tissue typing (Section 2.2.3).

2.2.1 Fundamentals of tissue typing using RF echo signals

Commercial medical ultrasound transducers generally operate at frequency ranges of $2 - 12\ MHz$. The ultrasound beams generated by these machines undergo different interactions with the structural elements of the tissue. The main interactions are the scattering and the absorption of the ultrasound signal. The net result of each interaction mechanism on the signal is a function of the ultrasound frequency, temperature, and the characteristics of the tissue. Therefore, the ultrasound echo signals (which, due to the similarity of their frequency range to radio-frequency waves, are called RF echo signals) contain valuable information about the physical properties of the tissue [94].

Some of the tissue characterizing parameters can only be extracted from RF echo signals before they go through the nonlinear process of envelope detection for B-scan image generation. The methodology of this analysis was introduced in the late 60's: Researchers realized that the frequency dependence of the backscattering phenomena can be used to derive the tissue characterizing parameters from the RF echo signals [128]. This frequency dependency results in high-frequency components of an ultrasonic pulse being more reduced in amplitude compared to low-frequency components at the same depth. The distortion caused in the waveform shifts down the central frequency in the spectrum of the RF echo signal and the pattern of this change can be used to characterize the propagation medium [41]. However, there exists one major

challenge to this approach: the echo signals received by the transducer in an ultrasound system are affected by other factors as well. For tissue typing, we are interested in fundamental properties of the tissue that affect the ultrasound through frequency-dependent backscattering and attenuation of the signal. Yet the ultrasound signals are also affected by movement of the tissue, the mechanical and electrical properties of the transducer, and diffraction effects due to the finite aperture of the transducer [126, 186]. Thus, appropriate measurements and analytical models of different phenomena affecting the signal are needed to extract the scattering function of the tissue [76, 126].

The most commonly utilized tissue characterizing parameters extracted from RF signals are those describing the attenuation and scattering of ultrasound in the tissue. The first assumption made for characterizing the ultrasound attenuation is to consider a uniformly distributed attenuation due to absorption. According to the classical work of Pauli and Schwan [161] which was further developed in [24], the acoustic attenuation of ultrasound in tissue is an exponential function of the covered distance in the tissue and of the frequency-dependent attenuation coefficient. For biological tissues, this frequency dependency can be considered linear [150] and the parameters of this linear relationship characterize the attenuation.

A more complex interaction between tissue and ultrasound is scattering. Fluctuations of physical properties such as elasticity, density, acoustic velocity, specific acoustic impedance, index of refraction and viscosity in different parts of the tissue result in scattering. The task of quantitatively characterizing the scattering based on RF echo signals has proven problematic. The difficulty stems from two sets of

problems: i) measurement reproducibility and transducer calibration, and ii) theoretical shortcomings in modeling the scattering phenomena. Researchers need to consider simplifying assumptions (such as isotropic scattering and uniform absorption) to reasonably describe the interaction of ultrasound and tissue (see [126] for details). Scattering measures may only be extracted after compensating the spectrum for depth-dependent attenuation effects. Details of the multi-narrow-band method used to model and compensate for the attenuation, are discussed in [24, 130, 157].

Today, well-established methods exist for the extraction of tissue characterizing features from RF echo signals. As illustrated in the first row of Figure 2.1, the feature extraction procedure involves a pre-processing step during which the signal is compensated for the system-dependent effects. The most popular attenuation parameters include the axis intercept, slope and midband values (extracted from the linear regression of the frequency spectrum of the RF signal). After the attenuation parameters are extracted, the spectrum is compensated for depth-dependent attenuation and the primary spectral features characterizing the backscattering of the tissue are computed. Important backscattering features are slope, axis intercept, midband value, integrated power and deviation from the linear regression fit of the spectrum [37, 128, 182, 186]. A number of groups have theoretically analyzed the capability of RF-spectrum parameters to discriminate tissue types in prostate. Feleppa *et al.* [55] used databases of RF parameters drawn from normal and histopathologically proven cancerous tissues, and tried to extract parameter ranges and discriminant functions for different pathological conditions. Their study shows a significant intercept, slope and midband value differences between normal and cancerous tissues in a population of 30 patients.

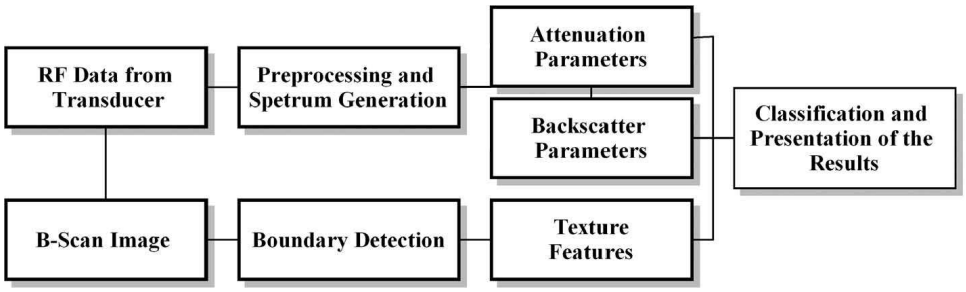

Figure 2.1: The general procedure of RF- and B-scan-based tissue typing. Features characterizing the attenuation and backscattering are extracted from the frequency spectrum of RF signals (top row) and combined with texture features extracted from B-scan images (bottom row) to be used for tissue classification.

2.2.2 Fundamentals of tissue typing using B-scan images

Besides the RF-spectrum analysis, many researchers have used texture features extracted from ultrasound B-scan images for prostate tissue typing. The initiative is that the speckle pattern in the ultrasonic image can reveal structural information about the tissue. We review some of the important B-scan texture features utilized for prostate tissue typing.

For texture classification, the object image is divided into windows of reasonable size or ROIs[6]. The first-order statistical moments (mean, standard deviation, skewness and kurtosis) of the intensities of pixels in each ROI form a basic set of features for texture typing [182, 85]. Furthermore, the speckle Signal to Noise Ratio (SNR), maximum and minimum, ratio of squares, and the Full Width at Half Maximum (FWHM) of the intensity of the pixels within ROIs have been found useful for prostate tissue typing [182, 186].

[6]ROI sizes between 0.1 cm^2 and 1.45 cm^2 have been reported in the literature.

Texture classification based on first-order statistical features has three major shortcomings: i) it has been shown that the SNR of the ultrasound images approaches a saturation value of 1.91 as the scatterer density increases [220]. Therefore, the capability of some first-order statistics to characterize high density tissues is limited. The scatterer density in many biological tissues does not exceed the saturation level [226]; ii) the mean intensity values of different images can not be compared because different imaging systems apply different gain adjustments [9]; and iii) tissues affected by the same pathology might show different acoustical properties (For example, in case of prostate cancer, while most PCa lesions are hypoechoic, there are cases of hyperechoic and even isoechoic appearance of tumor on ultrasound images).

These limitations have prompted researchers to use features extracted from co-occurrence matrices which are based on second-order conditional statistics [9, 182, 186]. The co-occurrence matrix of an image is a square matrix of size $N_g \times N_g$ (where N_g is the number of gray scale levels in the image). It is a histogram representation that describes the co-occurrence of a pair of intensities at a given distance (d) along a certain direction (θ). For feature extraction from gray-scale images, usually only the co-occurrence matrices corresponding to directions $\theta = 0^\circ$ and $\theta = 90^\circ$ with different values of d are used [9, 213]. A great number of texture features can be extracted from co-occurrence matrices. Haralick *et al.* were the first to introduce the concept and the formulation of such features [79]. For prostate tissue typing, features such as entropy (a measure of disorder in distribution of intensities), contrast (a measure of variation in intensities), correlation, angular second momentum (a measure for homogeneity), variance of the co-occurrence matrix elements, inverse difference moments, sum average, sum variance, sum entropy, difference entropy, information

measures of correlation, maximum probability, and many others have been extracted from co-occurrence matrices and used in different studies [9, 87, 142, 182, 213]. We will review the classification methodology and results of these studies in Section 2.2.3.

Texture parameters extracted by other techniques have also been utilized for ultrasonic tissue typing (mostly in tissue types other than prostate). Previous literature proposed a PCa diagnosis method based on Gabor filter texture segmentation [141]. Vorhoeven and Thijssen studied the potential application of fractal dimensions for lesion detection in echographic images [218] and later, fractal feature vectors based on M-band wavelet transform were used for ultrasonic liver tissue typing [121]. Bleck *et al.* [14] extracted texture parameters considering autoregressive periodic random field models for liver tissue typing. DaPonte *et al.* [31] applied Markov field models for texture feature extraction. De Marchi *et al.* have used fractal and statistical features of speckle in B-scan images for detection of prostate cancer [138].

It should be noted that manual, semiautomatic or automatic detection of the boundary of prostate on the ultrasound images is a primary step for applying the methods discussed in this section and also for generating 3D models of prostate [54, 59]. Several researchers have worked in this area [1, 27, 35, 65, 68, 73, 74, 86, 116, 117, 127, 149, 160, 192, 212, 222, 232, 236]. A comprehensive review of different boundary delineation and segmentation methods of prostate tissue from ultrasound images is beyond the purpose of the current survey (for a recent review paper on ultrasound segmentation see [151])[7].

[7]In addition, it is important to note that to evaluate the results of ultrasound-based techniques for prostate cancer detection, one should compare them with the results acquired by the histopathologic analysis of the same cross section of tissue. This brings up an ultrasound to histopathology registration problem, which is normally solved using visual landmarks. However, some researchers have developed more accurate approaches to solve this problem. For example, see [207] who have created fiducial points in the tissue using a four prong device to register their *ex-vivo* ultrasound

2.2.3 The results of ultrasound-based methods in diagnosis of prostate cancer

RF/B-scan features have been used in combination with pattern recognition techniques to increase the accuracy of PCa diagnosis. Here, we review some of the studies that have followed this approach. The final results of these studies, which are usually presented as 2D or 3D maps illustrating different classes of prostate tissue are used for biopsy guidance or diagnostic decision making.

A few researchers merely use texture features to characterize prostate tissue [85, 132], sometimes in combination with basic clinical measures such as the location of area of interest in the prostate gland [78]. In [85], the performance of the first-order statistics (mean, standard deviation, skewness and kurtosis) of the B-scan images were analyzed to localize cancer lesions on a group of 25 patients. The results show that the average pixel intensities in non-cancerous regions are lower compared to cancerous areas; the average skewness and kurtosis values are greater in the cancerous areas; and the standard deviations are not significantly different. The authors utilized decision trees to classify ROIs based on mean and skewness values [85] and acquired an overall accuracy rate of about 80% (compare to the 64% accuracy of the visual inspections). Basset *et al.* [9] published a detailed analysis on the functionality of texture features derived solely from co-occurrence matrices (second-order statistics) for prostate tissue

images to histopathology. They have used a 3-D correlation registration algorithm and reported accuracies between 89%–94%. Similarly, researchers have studied MRI to histopathology registration. Zhan *et al.* have developed a deformable registration methodology that utilizes prostate boundary points and internal salient points, identified with a space-scale analysis method, as landmarks. Using this approach, they have reported an average of up to 80% of correct overlap between manually and automatically labeled cancerous regions on MRI images [234, 235]. Also, in a recent work, a registration method called combined feature ensemble mutual information is developed for registration of 4 T MRI with whole mount histology images [23]. The authors of [23] found their method superior to image intensity-based mutual information registration.

typing. They applied values of $d = 2$ to $d = 50$ (where d stands for the distance used in computation of the co-occurrence matrices, see section 2.2.2) and have reported the classification results for ROIs of about 64×64 pixels in size corresponding to 1.45 cm^2 of the actual tissue. The ROC analysis showed 83% specificity versus 71% sensitivity. However, decreasing the region size to 16×16 pixels reduced the accuracy, and resulted in sensitivity of 41%.

Recently, Mohamed and Salama [142] used a mutual information algorithm to select a subset of second order texture features for prostate tissue classification. They examined their feature vectors using support vector machines as classifiers and reported accuracy ranges from 83.5% to 93.7%. Huynen *et al.* [87] obtained a specificity of 77.1% and a sensitivity of 80.6% by devising a feature vector of combined first- and second-order statistics of prostate ultrasound images. One of the most recent studies that take advantage of only textural B-scan features for detection of prostate cancer is by Llobet *et al.* [132] who report an area under the ROC curve of 61.6% with k-nearest neighbors (k-NN) and Hidden Markov classifiers.

As previously discussed, an important set of ultrasound-based tissue typing features are extracted from RF echo signals. Feleppa *et al.* [57, 56, 60] reported on prostate tissue typing systems that combine a set of features extracted from spectrum analysis of RF signals with clinical data. The clinical data fields consisted of PSA, age, ethnicity, and radiologist's interpretation of the B-scan images. This combined feature vector was used in conjunction with artificial neural networks as classifiers. The authors found radial basis function neural networks and Multi-Layer Perceptrons (MLPs) efficient for this application. The best performance of an MLP in their study was 84% (showing a considerable improvement compared to the 66%

success rate on clinical assessment of B-scan images from the same dataset).

Different ranges of accuracy have been reported on the classification efficiency of specific groups of features. This can be interpreted as a sign of the dataset-dependent nature of some of the features utilized and also of the different sizes of ROIs considered for feature vector generation. One possible solution for designing a robust tissue typing system is to use large datasets and hybrid feature vectors (including RF spectrum, image texture features, and clinical data). This is an ongoing trend. Scheipers *et al.* [182, 183] published a study involving 100 patients who all received radical prostatectomy as their treatment option. The researchers analyzed 40 different features [183] and later a selected set of 28 features [182] for classification of ROIs of 0.1 cm^2 in size. In the latter study, features included three attenuation parameters, five scattering parameters, eight first-order image texture parameters, nine second-order texture parameters extracted from co-occurrence matrices, and also three clinical parameters. The classification method of the study involved feeding the feature vectors characterizing each ROI to two parallel neuro-fuzzy inference systems. The outputs were processed to evaluate the contextual information and then combined to generate a malignancy map to assist the biopsy process. The researchers obtained a success rate of 86% (in terms of the area under the ROC curve) in distinguishing between hyperechoic or hypoechoic tumors from normal tissue, and 84% in distinguishing between the isoechoic tumors and normal tissue.

Schmitz *et al.* [186] also utilized hybrid feature vectors for PCa detection in ROIs of the same size (0.1 cm^2). They performed studies on 33 patients and used Kohonen maps and linear and quadratic Bayes classifiers, and nearest neighbor methods. ROIs characterized by a 16-dimensional feature vector consisting of attenuation, scatter

and texture parameters were classified. Their best result is reported to be acquired from a 3×3 self-organizing Kohonen map based on the Mahalanobis distance. The results were presented by a color map which included six different color codes. They acquired a success rate of 82% for sensitivity and 88% for specificity.

2.2.4 Section summary and discussion

In this section, we reviewed computer-aided methods for detection of prostate cancer that utilize features extracted from B-scan images or ultrasound RF signals. Tissue regions of sizes in the range of 0.1 cm^2 to 1.45 cm^2 have been classified based on first-order statistical moments of B-scan images [85] and second order statistics such as co-occurrence matrices [9]. Researchers have also used features like axis intercept, slope and midband values extracted from the frequency spectrum of the ultrasound RF signals for prostate tissue classification. In several studies, the RF and B-scan features have been combined to obtain the optimal ultrasound-based feature vector for PCa detection. Overall, ultrasound-based prostate tissue classification systems outperform the visual interpretation of images. Feleppa *et al.* have reported a comparison between the performance of visual inspection and classification based on RF-spectrum features in detection of PCa. While the former results in accuracies ranging from 64% to 66%, RF-based classification delivers 75-82% accurate classifications [58].

From the survey of the literature it appears that texture features extracted from B-scan images and spectral parameters proposed by Lizzi and Feleppa [55, 130] are the most frequently utilized and cited approaches in ultrasound-based tissue characterization. Therefore, in the current thesis, these two methods were chosen for comparison with the proposed method of detection of prostate cancer from RF time

series features. Detailed description of the features proposed by Lizzi and Feleppa and also the texture features will be given in the upcoming chapters.

Clinical acceptance of the methods reviewed in this section is subject to overcoming challenges in ultrasound-based tissue typing [101]. However, as a cost efficient diagnostic approach, ultrasound-based techniques can potentially play an important role in the future of computer-aided methods for detection of PCa. Some of the described diagnostic techniques in this survey, and the methodology developed in this thesis, require direct access to RF signals. Previously, this access has only been possible through the design of custom-built hardware by individual research groups, or special arrangements with ultrasound manufacturers. Recently, at least two manufacturers of ultrasound machines have provided their users with direct access to RF echo signals, on certain models of their clinical products, with no need for additional hardware.

2.3 Ultrasound Doppler

Doppler mode imaging is an alternative ultrasound-based solution for detection of pathologic conditions. In this section, we review the basic principles of this approach and describe some of the features extracted from Doppler images for tissue typing purposes (Section 2.3.1). We also review methodologies and results of studies that evaluate the performance of ultrasound Doppler-based methods for detection of prostate cancer (Section 2.3.2).

2.3.1 Fundamentals of Doppler-based tissue typing

The development of cancer is associated with changes in cellular metabolism. In this process, an increase in the uptake rate of nutrients and oxygen eventually leads to an increase in blood supply per unit time to cancer lesions and therefore, to neovascularization in the malignant area [75]. In general, according to studies on different organs (including prostate [15, 18, 180]), hypervascularization is believed to be correlated with cancer. Moreover, clear correlations between the micro-vessel density and Gleason grade in prostate cancer have been found [224].

The neovascularity phenomenon suggests that malignant tissue could be identified by studying the blood flow at the capillary level. Ultrasound Doppler systems are now standard tools to study the blood flow in the cardiovascular system. Such ultrasound-based systems operate based on the Doppler phenomenon: Reflected/scattered ultrasonic waves from a moving object undergo a frequency shift proportional to the speed of the moving object. Modern Doppler systems provide a color flow image in which Doppler frequency shifts measured from sample volumes are displayed on the B-scan gray scale images. An alternative representation is to measure and display the total power of Doppler signal from each sample volume; this quantity is governed by the volume of moving scatterers (mainly red blood cells). Systems that measure and present the power of Doppler signal produce the so-called power Doppler images.

A fundamental problem in Doppler-based cancer detection stems from the fact that ultrasound beam is backscattered both from the tissue and from the moving blood cells. Blood is a relatively weak scatterer of the ultrasound (much weaker than the surrounding tissue). Therefore, in order to separate a Doppler signal from the

background signal, a considerable frequency shift is required which confines high-accuracy Doppler studies to larger vessels with high blood velocity. The neovascularization associated with neoplasia is usually at microvascular level. This fact restricts the applicability of Doppler analysis in PCa detection [144]. It is possible to increase the intensity of signals scattered from blood cells by injecting ultrasonic contrast agents. The acoustic properties of these agents result in a stronger signal being reflected from the blood, enabling the Doppler method to detect even small vessels perfusing around a tumor [217]. Studies have shown that the contrast-enhanced ultrasound Doppler results in reproducible classification of prostate tissue [189]. Current limitations of the contrast agents include the lack of availability of approved agents, the cost, and the lack of randomized trails demonstrating an actual improvement in the diagnosis rate [72].

In spite of these limitations, some researchers have attempted to extract the maximum possible tissue typing information from Doppler data. Here, we introduce the quantitative vascular measures extracted from Doppler images and signals.

Power Doppler pixel density, normalized mean power in colored pixels and normalized power-weighted pixel density are three quantitative measures *extracted from power Doppler images* that characterize the distribution of Doppler signal power in ROIs. In color flow images, Speed Weighted Pixel Density (SWD) and mean speed in colored pixels quantize the frequency shifts in ROIs. Speed- and power-weighted normalized pixel density is a combined measure which uses both the frequency shift and power mode information. Details on the computation of these features can be found in [144].

The pulsatility index and the resistance index are the most widely used measures

for quantitative analysis of Doppler data and *are extracted from Doppler signals* [46]. They are measures of damping in the waveform which can be an indication of stenosis in cardiovascular studies (see [46] for the formulations). Results of [106] show that the resistance index can be an acceptable indicator of benign prostatic hyperplasia (non-cancerous enlargement of prostate). The resistance index is also used in kinetic studies of prostate tumor blood flow [155].

Vascularity indices are functions of the number of color pixels in a region of interest. In order to evaluate the correlation between vascularity and prostate cancer, researchers need to register the Doppler images spatially with the gold standard images (*i.e.* histopathology images on which cancerous lesions are segmented by a pathologist). The accuracy of tumor segmentation and registration process can affect the overall performance of the researchers in evaluating their results. Segmentation is almost always performed manually and registration is carried out either visually or semi-automatically [145, 167]. Potdevin *et al.* have used manual segmentation of tumors in histopathology slides [167]. They have used an ellipsoid fit for the boundaries of prostate in both the histological and Doppler ultrasound images and applied an affine transformation to register the two datasets. They report an average registration error of 0.2 cm.

2.3.2 The results of studies in Doppler-based methods

Initial reports on application of Doppler imaging for prostate studies date back to 1990 [223]. At that time, power Doppler method was not available and conventional color flow imaging was used for tissue typing. Today, Doppler signals, power Doppler images, and color flow images are all utilized for detecting malignant tissues and

assisting biopsy [155, 217].

Potdevin *et al.* have used Doppler measures to locally discriminate PCa [167]. In that study, prostate glands were visually divided into peripheral and periurethral regions. Doppler measures were calculated for ROIs of size 1 mm^2 .The results show that speed and SWD are acceptable discriminators for PCa in the peripheral and periurethral regions of the gland, respectively. According to the results of this study, the area under the ROC curve, obtained from SWD, is about 80%, making it an acceptable measure for inclusion in feature vectors used for classification of prostate tissue. Two power Doppler features utilized in the mentioned study did not show a high diagnostic value (the area under the ROC curve was reportedly about 60%).

In another study [206], Tang *et al.* selected 54 patients with distinct cancer lesions on ultrasound images. They manually segmented lesion areas. For this specific set of regions of interest (with typical diameter of 2.2 cm), they calculated the density of color pixels from Doppler images and used statistical t-test to analyze the relationship between the density ratio and malignancy. In 91% of the cases, abnormalities were detected (this sensitivity should be interpreted along with the large size of ROIs).

In a recent study by Arger *et al.* [5], the total vascularity and vascular density extracted from power Doppler images were exploited for cancer diagnosis. Total vascularity is the average number of vessels per image plane of the prostate. It is based on a simple count of color pixels in the image planes. On the other hand, vascular density divides the number of color pixels in each plane by the total number of pixels enclosed within a region which can be the entire prostate, central or peripheral zones. Based on the report of Arger *et al.*, vascularity extent measured by total vascularity and vascular density ranged from low to high in different tissue types and hence, these

measures did not show a substantial difference between diverse pathologic situations.

In a clinical trial, Kravchick *et al.* [111] reported a considerable increase in the diagnostic accuracy resulting from combining the B-scan image and Doppler information. It has also been shown that increasing the operating frequency of the ultrasound to about 20 MHz makes it much more efficient for imaging microcirculation [69], which is not feasible on current clinical machines.

2.3.3 Section summary and discussion

In this section, ultrasound Doppler was reviewed as another ultrasound-based source of information for detection of prostate cancer. Doppler-based cancer detection methods take advantage of the neovascularization phenomenon in cancer tumors. However, the results obtained from computational analysis of Doppler images for PCa detection are not generally in harmony with the strong biological evidence indicating increased vascularity in cancer lesions. This is probably due to the basic limitations of Doppler signal intensity during imaging of the microvascular structures. While the intravascular contrast enhancing agents can increase the intensity of Doppler signal from the micro-vessels, legal and technical difficulties have limited the application of such agents. One of the possible applications for Doppler-based indices can be combining them with other sources of information such as ultrasound images and signals. This possibility has hardly been explored in the reported studies.

It should be noted that the resolution of the Doppler-based methods for cancer detection (at least at their present form) is limited. In other words, Doppler measures provide us with a general image of vascularity without specifically delineating the borders of the tumor.

An alternative solution to take advantage of the neovascularization phenomenon for PCa detection is the visualization of microscopic capillaries. High-frequency ultrasonic imaging (ultrasound biomicroscopy) is a technique that aims to achieve such visualizations [64]. This technique is well studied in applications such as ophthalmology, however, clinical trials of ultrasound biomicroscopy in case of prostate cancer are only in primary stages [227][8].

2.4 Chapter summary and conclusions

Accurate and efficient diagnosis and grading of prostate cancer plays a crucial role in controlling the mortality rate of this common malignancy in men. It also can provide the information needed for properly deciding on the treatment options for patients. This chapter presented a comprehensive review of the current computer-aided methods for diagnosis of prostate cancer. We particularly discussed the ultrasound-based techniques used for prostate tissue typing. Hybrid texture/RF-spectrum features in combination with nonlinear classification methods have resulted in detection of prostate cancer in ROIs as small as 0.1 cm^2 with sensitivity and specificity values of up to 82%. This is a great achievement; however, higher values of accuracy and stronger scientific theories that correlate pathological conditions with acoustic properties of tissue are needed to justify the inclusion of automatic ultrasound-based tissue typing methods in routine diagnosis. Furthermore, large scale clinical studies are needed to ensure the utility of the tissue typing methods in diagnosis of prostate cancer.

[8] Studies on brain MRI images has also confirmed a correlation between abnormally shaped vessels and cancer [20].

We also reviewed studies in which the phenomenon of neovascularization around cancerous tissue has been studied with ultrasound Doppler techniques. Researchers have often failed to correlate Doppler features extracted from the clinical ultrasound machines with the actual capillary counts. This limitation is probably due to the weakness of the Doppler element of the ultrasound signal generated by the capillaries compared to the signal scattered by the surrounding tissue and can be partly addressed by using contrast agents.

In recent years, researchers have been trying to design automatic systems for targeted biopsy and placement of radioactive seeds for brachytherapy purposes under ultrasound and MRI guidance [6, 34, 61, 71, 80, 100, 112, 221] and have used C-arm images registered to ultrasound to overcome the poor quality of the radioactive seeds in ultrasound images [91]. With efficient targeting and guidance systems already available, accurate and reliable classification of prostate tissue (from ultrasound and MRI images) is a missing component of a comprehensive computer-aided prostate intervention system. The research carried out for this thesis is an effort to devise a method that improves and/or complements the available methodologies for ultrasound-based tissue characterization aimed at augmenting the prostate interventions, specifically, the biopsy process.

Chapter 3

Ultrasound RF Time Series

The fundamental novelty of this thesis is the introduction of ultrasound RF time series as the source of tissue typing information. In this chapter, we describe this concept. We also present a simulation study that confirms the existence of information-rich variations in ultrasound RF echo samples acquired from a specific location in a scattering media subject to sequential ultrasound emissions.

3.1 RF time series: A new paradigm in ultrasound-based tissue typing

Ultrasound beams undergo different interactions with the structural elements of the tissue, mainly scattering and absorption. The mechanism of these interactions is frequency-dependent and is also affected by the characteristics of the microstructure and macrostructure of the tissue. Therefore, the ultrasound echo signals (which, due

to the range of frequencies of medical ultrasound probes, are called RF echo signals) contain valuable information about the structural properties of the tissue [94]. However, several factors complicate the process of ultrasound tissue characterization, mainly: 1) Biological tissue is highly heterogenous. What is collectively called "tissue", in fact consists of a combination of different cell types and biological molecules in the microstructure level and various structures such as glands and capillaries with different acoustic properties. 2) The sources of the perturbations in echoes are not fully understood. The models that describe the backscattering and attenuation of ultrasound in biological tissue are complicated and approximate. 3) The alterations in the received echoes are also a factor of variations in transducer parameters such as the center frequency or output intensity. These challenges have limited the level of the success in ultrasound-based tissue typing [101].

The most commonly cited and utilized approach for ultrasound-based tissue typing proposed by late Frederick Lizzi and Ernest Feleppa [55, 130], compensates the effects of system dependent parameters by dividing the frequency spectrum of the received RF signals by a calibration spectrum. The calibration spectrum is acquired by scanning an isonified flat glass plate and describes the machine dependent properties of the ultrasound echoes. Lizzi, Feleppa and their colleagues have shown that the average slope and intercept of the calibrated frequency spectrum of segments of RF A-lines in an ROI of the tissue can be used as tissue characterizing features [128]. This approach to tissue typing does not rely on a physical model of the interaction between the tissue and ultrasound. Instead, it relies on the consistent experimental "observation" of certain characteristics in the frequency spectrum of the signals backscattered from a tissue type and assumes that the occurrence of such characteristics indicates

the presence of that tissue type [102].

The methodology of tissue typing proposed in this thesis shares the "observation-based" nature of the previous approaches. However, the observed features of backscattered ultrasound are extracted from a sequence of echoes received from a specific location of tissue, and not from a single frame. In other words, the fundamental observation is that if a certain spot in tissue undergoes sequential ultrasound emissions in the typical frame rates of clinical ultrasound machines, the time series formed by recording the echoes from that location carries information that can be used for tissue typing. In order to clarify this statement, one should notice that digital ultrasound machines normally have a linear or curved array of piezoelectric crystals (128 is a typical number). To form the ultrasound image, a number of the crystals become active at a time (32 is a typical number for the active crystals). The received echoes are combined with beamforming techniques, to form one line of sight which is called an RF scan line [81]. Each scan line is a discrete signal and the number of its samples depends on the depth of imaging and the sampling frequency of the ultrasound machine. A number of these scan lines that cover the width of the probe, form one frame of RF data. The mechanism of forming the B-scan images involves applying envelope detection to the RF scan lines. However, the envelope detection process removes some of the details of the signal that could be vital for tissue typing. Therefore, for tissue typing, the conventional methods extract the features from the spectral frequency of these RF scan lines before transformation to B-scan data. In our proposed method, we acquired the RF scan lines, keep the ultrasound probe and the tissue fixed in place, and continue acquiring frames of RF data at the frame rate of the ultrasound machine. The sequence of one sample of one RF scan line over

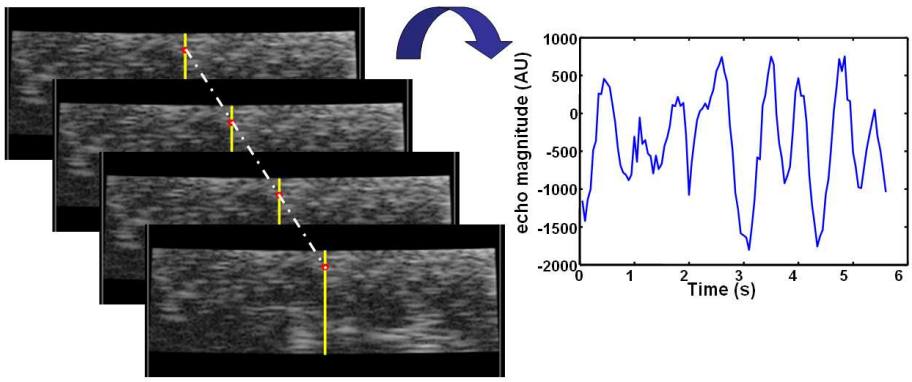

Figure 3.1: Samples of RF echo signals, collected over time from a fixed spot of tissue under emission of ultrasound at the frame rate of the ultrasound machine, form one RF time series.

time, forms what we call an RF time series. The principal frequency of the RF time series is defined by the frame rate of the ultrasound machine. Figure 3.1 illustrates the concept of RF time series.

In the remainder of this chapter, we provide a potential explanation for the phenomenon that forms the central hypothesis of this thesis (Chapter 1.3): the existence of tissue typing information in RF time series.

3.2 A potential explanation for variations in RF time series

The two following questions about RF times series are inevitable: 1) Why should there be any alterations in the RF time series while the tissue and the probe are fixed in position? 2) If such alterations do exist, do they contain tissue typing information?

A large portion of the present thesis will be dedicated to the answer to the second question. We will provide phantom studies, animal tissue typing studies and a clinical study involving detection of prostate cancer from ultrasound data. The results of these studies show that a set of features extracted from RF time series are accurate in tissue typing and improve the clinical diagnosis of prostate cancer. The remainder of this chapter, deals with the first question.

In the absence of external mechanical force or controlled variation of the incoming ultrasound beams, two sources can create variations in the echoes received from the tissue: 1) The electronic noise of the ultrasound machine that appears as jitter in the intensity and the frequency of the ultrasound beam. 2) Possible vibrations in the microstructure of the tissue caused by the acoustic radiation force exerted by the sequence of ultrasound beams. The former source is undisputable. However, as we will show in Chapter 6, it has a negative effect on the tissue typing results. So we discuss the latter here.

All forms of wave motion, including the acoustic waves, exert a unidirectional radiation force on obstacles in their path [211]. In case of acoustic waves, it has been shown that the force applied to the tissue can be described as:

$$F = \frac{2\alpha I}{c} \tag{3.1}$$

where c is the speed of sound in the medium, α is the absorption coefficient of the tissue, and I is the average intensity of the incident beam. The average intensity can be described as

$$I = \frac{1}{S}\frac{d\langle E\rangle}{dt} \tag{3.2}$$

where S is the cross sectional area of the beam and $\langle E \rangle$ is the short term time average of the energy of the ultrasound waveform [109].

For a perfectly sinusoidal ultrasound beam waveform, the mean sound pressure and the force that particles undergo can be considered zero [211]. However, perfect sinusoidal waveform is not achievable even with the simplest model of medium of propagation [211]. The aberration of the waveform from sinusoidal form occurs due to the nonlinear interaction of tissue with the ultrasound beams. Torr has shown [211] that the radiation force intensity of 1 W/cm^2 exerted by the ultrasound beam can be explained by the existence of an aberration of the incoming signal from the sinusoidal form that produces only an average pressure of 10^{-4} times the amplitude of the ultrasound waveform. Therefore, the radiation force does exist, even at the absence of a controlled method to generate harmonic locally deposited energy[1]. Konofagu and Hynynen [110] show the validity of this claim through measuring the particle displacements. Since the existence of this force depends on the alteration of the ultrasound waveform from its original sinusoidal form due to the effects of tissue type dependent absorption and attenuation, the amount of force, F, depends on the tissue type.

In our methodology, the ultrasound force is applied in an intermittent manner with a frequency matching the frame rate of the ultrasound machine (22 or 45 Hz in most of our experiments). The existence of the tissue-type dependent information in the

[1]It is important to note that different groups have used the concept of acoustic radiation force to generate harmonic locally deposited energy for imaging the mechanical response of the tissue [49, 110, 238]. The common approach is to use two focused ultrasound probes that work at slightly different frequencies. At the common focal zone, the average energy deposited locally by the two beams follows a sinusoidal variation with a frequency equal to the difference of the frequencies of the two transducers (see [109] for the derivation of this result.) By adjusting the difference of the frequencies to match the mechanical resonance frequency of the tissue, harmonic displacements with magnitudes up to $600 - 800$ μm have been measured and reported in the literature [110].

time series of RF echoes could be attributed to the microstructural vibrations under the low frequency mechanical excitation caused by the sequentially applied ultrasound energy that gives rise to a mechanical force in the direction of wave propagation.

To analytically evaluate the displacements of the particles under the scenario of RF time series acquisition, one could solve for the displacements of all nodes on an elastic network of connected nodes. Researchers in the field of elastography have proposed methods to solve for the displacements of tissue nodes under known force profiles using finite element methods [70]. The state of the system at the end of one cycle of emission, characterized by the locations and speeds of the nodes, could be used as the initial state for the next cycle. In the viscoelastic medium of the biological tissue, the displacement caused by F can be acquired by solving for x from [171]

$$m\ddot{x} + d\dot{x} + kx = F \tag{3.3}$$

where m, d and k are mass, damping and stiffness matrices describing the microstructure model of the tissue. Given the unknowns of the system, solving (3.3) under the assumption of intermittent emission of ultrasound is challenging [17]. The characterization of the force, F, at each spatial location is very complicated due to its dependence on the interaction between the tissue and the ultrasound and also the electronic noise of the machine. Furthermore, the inhomogeneous characteristics of biological tissue mean that the values of parameters m, d and k are not readily available. Due to these complications, we avoid the analytical approach for characterizing the displacements and resulting alterations in the echoed signals.

In the remainder of this chapter we will show, through computer simulation, that the microstructural vibrations can cause variations in ultrasound echoes and these variations meaningfully change with alterations in the simulated microstructure. This

will be performed by applying random vibrations to the scattering particles and studying the effects on the RF time series.

It should be noted the existence of the physiological movements caused by the spontaneous cell movements and capillary level blood circulation, can cause tissue-characteristic variations in RF time series in *in-vivo* studies. Recently, spontaneous cell movements under different physiological conditions have been characterized [205]. Since all the experiments reported in this thesis are performed in *ex-vivo* conditions, this phenomenon is unlikely to play a role. However, this should be considered for extending the method to *in-vivo* studies.

3.3 Field II simulations

As described in the previous section, the aim of the simulation study described here is to demonstrate that vibrations in microscopic level can cause variations in ultrasound echoes acquired from an ultrasound transducer and that these variations meaningfully change with alterations in the simulated microstructure. We used Field II ultrasound simulation program [95] to generate a simulated scattering medium with an assumed number of scattering particles and also, an ultrasound probe with realistic physical parameters. We created a frame of data consisting of a number of RF scan lines, applied a microscopic displacement to the scatterers and a minute and realistic amount of variation to the characteristics of the beam, and simulated the next frame. The magnitude of these variations was selected according to the manufacturer's datasheet available for the simulated probe (BPSL9-5 transrectal probe, Vermon, France). A sequence of 128 frames created with this methodology, formed the RF time series (Figure 3.2).

Since we did not have an analytical description of the force and the potential vibrations caused by the sequence of ultrasound emissions or the physiological movements, we could not exactly simulate the locations of the particles at the end of each cycle of emission. Instead, we applied random noise with Gaussian distribution to the location of the scatterers (relative to the locations at the beginning of the simulation) to model the microscopic displacement of the backscattering particles from each emission cycle to the next one. The mean of this Gaussian noise was chosen according to the published measurements of particle movements under emission of ultrasound [110]. Therefore, it should be noted that this simulation is not a modeling of the exact interaction of the tissue with the sequence of ultrasound beams.

3.3.1 Methodology

Field II is a simulation package that finds the intensity of echoes received by an ultrasound transducer. The program is written in C programming language and provides a number of Matlab (Mathworks, Inc.) m-files that call different functions of the program. The primary goal of the designer of the program, Dr. J. A. Jensen, has been simulating the ultrasound images in order to optimize the design of the ultrasound probes [95, 97]. The program provides commands to define the type of ultrasound probe (linear, phased or 2D matrix arrays) and also the number of piezoelectric elements, the number of active elements, the size and the distance between the elements, and the number and specifications of focal zones. To simulate the ultrasound image, Field II relies on the linear system theory and uses the concept of spatial impulse response to find the intensity of ultrasound created by a simulated probe at any given point in a simulated medium. The impulse response defined for the probe aperture

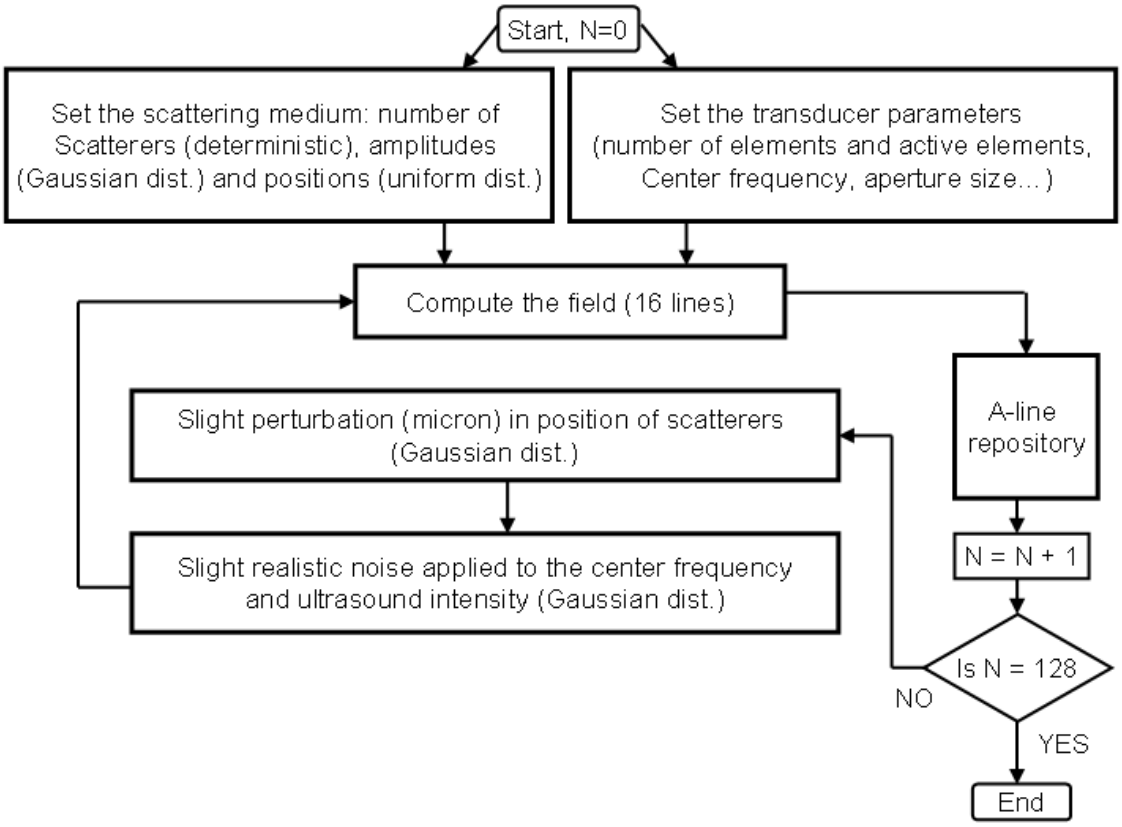

Figure 3.2: A flowchart illustrating the simulation process of RF time series. The simulation considered reasonable variations in the intensity and central frequency of ultrasound from each frame to the next. Under this assumption, the effects of the density of the scattering medium and the magnitude of the microstructural vibrations of the scatterers on the energy level of RF time series were studied.

determines the emitted ultrasound field at a specific point in space as a function of time, when the transducer is excited by an impulse (Dirac delta function). The field for any kind of excitation can then be found by convolving the spatial impulse response with the excitation function.

The simulated ultrasound transducer

The probe specifications in Field II were chosen to match those of the BPSL9-5 transrectal probe (Vermon, France) distributed by Ultrasonix Medical Systems (Richmond, BC, Canada) with SonixRP ultrasound machines. This probe has 128 elements with 32 active elements. The distance between the elements is 25 microns. The probe center frequency is 6.6 MHz. The sampling rate for the RF data was set to 40 MHz which is one of the two possibilities available on SonixRP.

The simulated medium

The physical phenomenon behind the formation of ultrasound RF signals and ultrasound images is the collection of echoes backscattered or reflected from the medium on the surface of a transducer. The medium can be considered continuous or discrete. In our simulation, we used the discrete model introduced by Bamber and Dickinson which is the basis of most studies on statistics of ultrasound speckle [7]. The medium was simulated as a collection of individual and independent scatterers, each re-emitting a part of the received acoustic energy in all directions in space. The Filed II methodology for calculation of the contributions of individual scatterers in the ultrasound echoes received in the probe is explained in detail in [96, 123].

We created a medium of dimensions $50 \times 60 \times 10\ mm$. The scatters were distributed

in the medium with a random uniform distribution. The density of scatterers was changed in different experiments to study its effect on the RF time series. The scattering amplitudes were chosen similar to the methodology of [95] which assumes a standard Gaussian distribution ($N(1,0)$). It should be noted that the simulated mediums corresponded to virtual phantoms with no specific anatomical structures or strong reflecting surfaces.

Field II is capable of simulating the effects of frequency and depth dependent attenuation of ultrasound due to absorption. We set the attenuation coefficient of the medium to 0.5 $dB/MHz - cm$ which is a typical value for vascular tissue [55].

The simulated data

The number of RF scan lines in each frame, covering the width of the phantom, was set to 50. The main disadvantage of Field II is the computation time. In our study, since each time series is formed by acquisition of 128 frames, the timing problem was a serious challenge. Therefore, we only simulated 16 lines in the center of the phantom for each simulation experiment.

With the described depth and sampling frequency, the length of each RF scan line in our simulated data was 3,500. A single transmit focal point was set at 3 cm deep in the tissue. The data at the focal zone was used for the analysis presented in this thesis and included 500 samples along each line totalling to 8,000 samples over 16 lines. Each of these samples formed a time series of length 128.

The noise applied to the central frequency of the probe from each frame to the next followed a Gaussian distribution with the mean at 0 and standard deviation of 50 KHz. The noise applied to the amplitude of the waveform was $\pm 3\%$ with a

Gaussian distribution. In other words, the central frequency of the probe at each frame was $f_c = f_0 + N(0, 50KHz)$ where $f_0 = 6.6\ MHz$ in our experiments and $N(\mu, \sigma)$ describes a Gaussian random variable with the mean of μ and the standard deviation of σ. The intensity of ultrasound at each location followed this pattern

$$I = I_0 sin(2\pi f_c t) + N(0, 0.03I_0) \tag{3.4}$$

These values were realistically chosen according to the data provided by the probe manufacturer. For example, the maximum deviation of the central frequency of the probe from the expected frequency of 6.6 MHz is 100 KHz. Therefore, a Gaussian noise with $\mu = 0$ and $\sigma = 50\ KHz$ could describe the electronic noise in this case.

Data analysis

For our analysis, we performed two sets of simulations:

1) In the first set, we created phantoms with different number of scatterers per volume. Specifically we created seven phantoms with 25,000, 50,000, 75,000, 100,000, 125,000, 150,000 and 175,000 scattering particles distributed uniformly over the volume of $50 \times 60 \times 10\ mm$. A time series of frames was created from each phantom. From each frame in the time series to the next, the beam and the location of the particles were perturbed. The location of the particles was perturbed relative to the original location, by displacing each particle along the direction of the ultrasound beam. The amount of displacement followed a Gaussian distribution of form $N(0, 1\ \mu m)$. This value is recorded in the measurements of [110] in the absence of harmonic mechanical excitation.

2) In the second set of experiments, we studied the effects of the magnitude of

the applied microstructural vibrations on the energy of the RF time series variations. We performed this experiment with three different phantoms with 50,000, 75,000 and 125,000 scattering particles. For each phantom, five time series of RF frames of length 128 were simulated. The difference between the five simulations was in the amount of displacement applied to the particle locations: the particles were displaced along the direction of the beam relative to the initial locations following Gaussian distributions all with mean of 0 μm and standard deviations of 0 μm, 0.5 μm, 1 μm, 2 μm, and 3 μm.

In our analysis, we compared the level of energy of variations of RF time series in different simulations. The existence of such variations, and their dependence on the specifications of the phantoms, could provide evidence to support our hypothesis of utility of RF time series for tissue typing. Therefore, the parameter of interest, used for comparison of RF time series in different simulations, was the averaged normalized energy of the time series which was computed as follows. For a single RF time series, with samples $x_{ts1}, ..., x_{ts128}$, the energy was calculated as

$$E = \frac{1}{128} \sum_{i=1}^{128} (x_{tsi} - \overline{x_{ts}})^2 \tag{3.5}$$

where $\overline{x_{ts}}$ was the mean of the time series and the length of the RF time series was 128. This value was averaged over each line segment as follows

$$\overline{E_l} = \frac{1}{500} \sum_{i=1}^{500} E_i \tag{3.6}$$

(the length of each of the scan line segments in the focal zone which were used in the analysis was 500). Therefore, for each simulation, 16 average energy values were acquired ($\overline{E_{l1}}$ to $\overline{E_{l16}}$). In order to compare the energy levels of different simulations,

these values were normalized by dividing them to the average spatial energy over all the sixteen lines of the first frame (among the 128 RF frames that formed the time series) in the simulation computed as

$$\overline{E_{spatial}} = \frac{1}{(8,000)} \sum_{l=1}^{16} \sum_{i=1}^{500} (x_{il} - \overline{x_l})^2 \tag{3.7}$$

where x_{il}'s and $\overline{x_l}$ were the samples and the mean of the samples along RF scan line l. This resulted in 16 averaged and normalized energy values corresponding to 16 line segments in each simulation. We called these values E_{ts}^{l1} to E_{ts}^{l16}

$$E_{ts}^{li} = \overline{E_{li}} / \overline{E_{spatial}} \tag{3.8}$$

3.3.2 Results of the simulation study

The results of the seven experiments with phantoms of different particle intensities are summarized in Figure 3.3. Each point in this figure is the average of the 16 values of E_{ts}^{li} for one simulation. The length of the error bar is two times the standard deviation of these 16 values. It is clear from Figure 3.3 that although the distribution of electronic noise was similar in all seven simulations, the increase in the density of the scattering particles resulted in a substantial increase in the average normalized energy of the RF time series.

The results of the experiments with varied magnitudes of microstructural vibrations applied to the scattering particles are depicted in Figure 3.4 for three different phantoms. The most important observation in this set of experiments was that when the magnitude of microstructural vibrations was set to zero, the average normalized

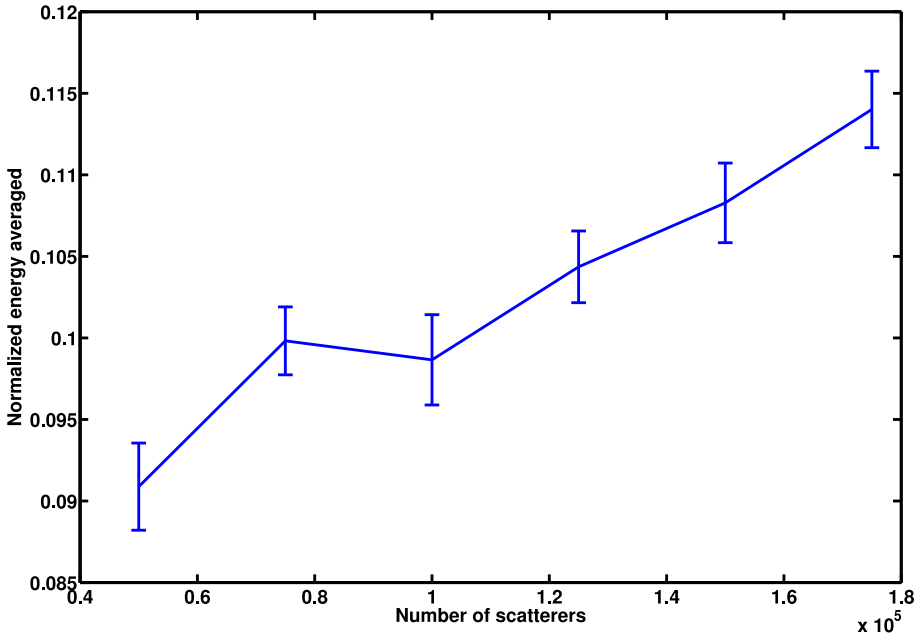

Figure 3.3: Normalized energy of RF time series for simulated phantoms with different number of scatterers per volume (seven simulations). At a fixed noise level ($\pm 3\%$ noise applied to the intensity of ultrasound and ± 50 KHz applied to the probe center frequency), the energy of variations in RF time series substantially increased for more dense scattering media.

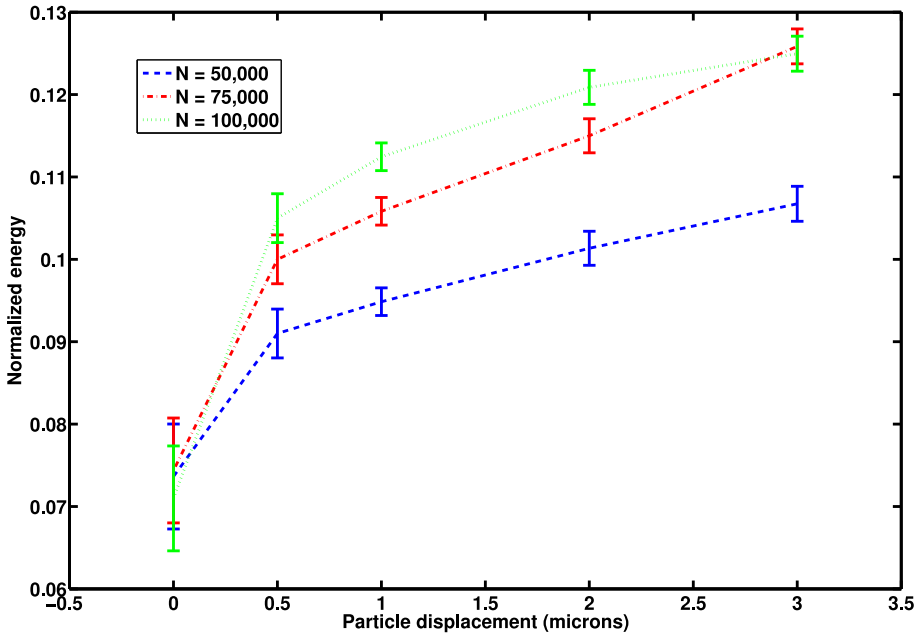

Figure 3.4: Normalized energy of RF time series for simulated phantoms with different amounts of microstructural vibrations. The simulations were performed for three different phantoms with 50,000, 75,000 and 125,000 particles. At a fixed noise level (±3% noise applied to the intensity of ultrasound and ±50 KHz applied to the probe center frequency), the energy of variations in RF time series consistently increased with larger magnitudes of vibration in all three phantoms.

energy of the RF time series was substantially smaller than the simulations with application of 1 μm or even 0.5 μm vibrations to the particles. It should be noted that the electronic noise was present in all cases and the level of noise applied to the beam was similar in all simulations. In other words, the key factor in formation of the variations of RF time series was the microstructural vibrations. It was also notable that increasing the mean of the distribution of displacements applied to the particles increased the energy level of the RF time series. This was consistently true for all three phantoms.

These experiments demonstrated that the microstructural vibrations of the scattering particles, within the ranges reported in the literature, under ultrasound emissions can create variations in time series of RF echoes. These variations increase with an increase in the density of the medium and are substantially stronger than the variations in RF time series caused only by the electronic noise of the probe.

3.4 Chapter summary and conclusions

In this thesis, we introduced the concept of ultrasound RF time series. To form the RF time series, we record ultrasound RF echoes backscattered from tissue, at the frequency determined by the frame rate of the ultrasound machine, while the imaging probe and the tissue are stationary in position. Our studies have shown that these time series contain tissue-type dependent information. We emphasize that our methodology to prove the utility of RF time series for tissue typing and specifically detection of prostate cancer is experimental and relies on pattern recognition techniques that will be described in the next chapter of this thesis. However, in this chapter, we provided a possible explanations for the existence of tissue typing contents in RF time series. Microstructural vibrations can be caused by the ultrasound radiation force. We examined the equations for the ultrasound radiation force which show that for ultrasound waveforms that are not perfectly sinusoidal, the long term average of the ultrasound radiation force is not zero. Since the ultrasound beams undergo non-linear and tissue-type dependent interactions with the biological medium, the beamform deviates from the sinusoidal form and, therefore, the scatters experience a non-zero and tissue-dependent force. Under emission of ultrasound at the frequency determined by the frame rate of the ultrasound machine, this non-zero force might

cause microstructure vibrations. In live tissue, physiological movements caused by spontaneous cell motions and capillary level blood circulation (both of which depend on the function of the tissue) can also create variations in the sequence of RF echoes.

In order to show that microstructural vibrations, in the order of 1 μm, can cause tissue dependent variations in RF time series, we performed a study using the Field II ultrasound simulation program. The results of this simulation study showed that microstructural vibrations can cause variations in the sequence of ultrasound echoes. These variations carry more energy than the variations caused merely by the electronic noise of the ultrasound probe. It was also shown that the energy of these variations increases with an increase in the density of scatterer particles. The results confirm a possibility of variations in RF echoes caused by the microstructural vibrations.

The physical phenomenon described here is one *possible* cause of the existence of the tissue-type dependent information in RF time series. The techniques presented in this thesis do not solely rely on the validity of this physical explanation. Throughout this thesis, we have chosen an experimental approach towards proving the utility of RF time series for tissue typing. We will discuss feature extraction and classification approaches that take advantage of this phenomenon for tissue typing. We show that the concept of RF time series can be successfully used for separating tissue mimicking phantoms with different sizes of particles. Then, we show that for animal tissue types of distinctly different microstructure, the success rate in tissue typing based on the proposed method is very high. Finally, we present the results of a study that show the proposed method can be used to detect prostate cancer.

Chapter 4

Feature Extraction and Classification

In our methodology for enhancing the prostate biopsy, small regions of interest (ROI) of tissue are described by features extracted from the corresponding ultrasound RF time series. A classifier is trained, in a supervised manner, using a portion of the data with known tissue types. This standard pattern recognition framework requires the extraction of proper features from RF time series and the choice of suitable classifiers. The proposed features and utilized classification methods are discussed in this chapter. The discussion here includes both the novel aspects of the presented research and the readily available features and classifiers approaches readily available. Such techniques are clearly distinguished from the novelties of the current work.

4.1 Novel features based on RF time series

The main group of tissue typing features proposed in this thesis are extracted from the Discrete Fourier Transform (DFT) of RF time series. These features should not be confused with the spectral features proposed by Lizzi and Feleppa which are based on the analysis of segments of RF scan lines in single frames of ultrasound data [55, 130].

4.1.1 Spectral features from RF time series

We propose six parameters extracted from the amplitude of the DFT of RF time series averaged over an ROI for tissue typing. These features form a small profile that represents the frequency spectrum of RF time series. Four of these features represent the energy of the time series in different frequency bands and two of them describe the general appearance of the spectrum of the time series.

Each RF time series is a discrete signal of length N equal to the number of sequentially acquired frames. We were interested in the variations of this signal; therefore, features were extracted from the zero-meaned time series. The discrete Fourier transform of the time series x_t is computed as

$$X[k] = \frac{1}{N} \sum_{n=0}^{N-1} x_t[n] e^{-j(2\pi/N)kn} \tag{4.1}$$

where X is the DFT of the zero-meaned RF time series x_t. The time series were zero-padded in case of some of our experiments were N was not a power of 2. DFT is computed using the Fast Fourier Transform (FFT) algorithm as implemented in MATLAB^{TM} (Mathworks Inc.). Since the RF time series are real and have mean of zero, $|X[0]| = 0$ and $|X[k]| = |X[N-k]|$ where $|.|$ denotes amplitude. In other

words, the frequency spectrum[1] of RF time series was completely represented by $N/2$ values, namely $|X[k]|$ where $k = 1, ..., N/2$. We averaged the spectrum over all RF time series corresponding to RF samples in one ROI. The averaged spectrum of the ROI ($|\overline{X}|_{ROI}$) was then normalized as follows

$$|\widehat{X}_{ROI}[k]| = |\overline{X}_{ROI}[k]|/max(|\overline{X}_{ROI}|) \tag{4.2}$$

This normalization process set the maximum of the averaged spectrum to 1 and enabled us to compare data from different ROIs. The six proposed RF time series features, listed below, were extracted from $|\widehat{X}_{ROI}|$. The first four features (S1, S2, S3 and S4) were the integral of $|\widehat{X}_{ROI}|$ in four quarters of the frequency range

$$S1 = \sum_{k=1}^{N/8} |\widehat{X}_{ROI}[k]| \tag{4.3}$$

$$S2 = \sum_{k=N/8+1}^{N/4} |\widehat{X}_{ROI}[k]| \tag{4.4}$$

$$S3 = \sum_{k=N/4+1}^{3N/8} |\widehat{X}_{ROI}[k]| \tag{4.5}$$

$$S4 = \sum_{k=3N/8+1}^{N/2} |\widehat{X}_{ROI}[k]| \tag{4.6}$$

In other words, we averaged the spectrum over different frequency bands to condense the signal information in $S1 - S4$ as features for tissue typing[2]. We also fit

[1]It should be noted that the described methodology here provides only the periodogram of the time series which is a rough estimation of the frequency spectrum. Throughout the thesis, we have used the expression "frequency spectrum" to describe this rough estimate.

[2]The idea of summarizing the frequency spectrum of a signal in a few parameters for pattern recognition purposes has been suggested in [170] and [231].

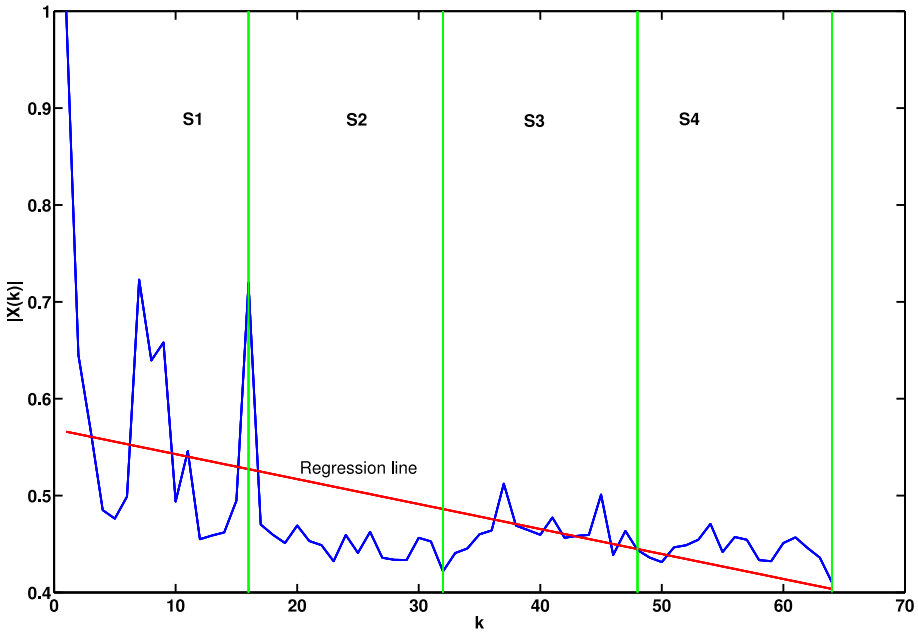

Figure 4.1: A plot of the normalized average frequency spectrum of RF time series of length 127 from ROIs of the pig liver tissue. The slope and intercept of the linear regression of the frequency spectrum and also, the sum of the amplitude values in four different frequency bands (separated by vertical lines on the graph) were used as features. The probe frame rate (which determines the principal frequency of RF time series was set to 22 fps. The probe central frequency was set to 6.6 MHz.

a least mean square regression line to values of the spectrum versus normalized frequency. The intercept (S5) and slope (S6) of this line were used as two more features. Figure 4.1 shows the normalized average frequency spectrum for one ROI of RF time series data acquired from pig liver tissue and depicts the process of computing S1-S6.

4.1.2 Fractal dimension

One of the parameters extracted from RF time series and found effective as a feature for tissue typing was the average fractal dimension of RF time series in a region

of interest in the tissue. The concept of fractal dimension (FD) is a generalization of the Euclidean dimension that reflects the complexity of a signal or object[3]. FD is a common feature used for the analysis of biomedical signals such as EEG [2, 82]. Researchers have studied FD of the time series formed by numerous biological processes including blood pressure [139] and heart rate [11].

The fractal dimension of a time series reveals properties that are raised from complex internal nonlinear dynamics of the underlying process [194] (rather than those caused by noise and environmental conditions). This property of FD is the incentive in utilizing it as a tissue typing feature. We do not have an analytical model of the mechanism of interaction between tissue microstructure and sequential ultrasound emissions. Therefore, it is difficult to separate the noise from microstructure-related features. Since FD is affected more significantly by the nonlinear dynamics of the interaction between the tissue microstructure and ultrasound beams, it proves useful in separating tissue types based on RF time series.

There are several algorithms for estimation of the fractal dimension of a time series [83, 103, 165]. Some of these algorithms (such as Katz's [103]) rely on geometric features of the curve formed by the time series. Others such as the widely utilized algorithm proposed by Higuchi [83], decompose the signal into different scales and evaluate the signal complexity.

[3]The concept of fractal dimension is widely used to characterize the self-similarity of an object. Self-similarity is the property of objects that are geometrically similar to their parts or have similar statistical properties to their parts. In signals, self similarity results in scale-invariant complexity: the signal preserves its complexity when it is scaled down. As Mandelbrot demonstrates [136], FD provides a measure of scale-invariant complexity even when the object is not a fractal object/signal. Therefore, one does not need to claim that the RF time series are essentially fractal in order to use FD as a measure of complexity. Since our simulations in Chapter 3 show that the energy of variations in RF time series significantly increases with increasing the complexity (number of scatterers) in the medium, the complexity of the RF time series characterized by FD was considered as one of the tissue typing features.

Higuchi's algorithm is proven to be a stable and accurate method to estimate the FD[4] of time series and more importantly, works for time series with few samples [45]. The algorithm computes mean length of the signal at different scales, plots a log-log graph of length versus scale, and measures the slope of the linear fit of this graph as the FD. The implementation details are as follows:

Consider N frames of RF data acquired while the probe and the tissue are fixed in position. Over time, each sample of the RF data forms a time series $\{X(1), X(2), ..., X(N)\}$. From this time series, first k new time series of form

$$X_k^m : \{X(m), X(m+k), X(m+2k)..., X(m+[\frac{N-m}{k}].k)\} \tag{4.7}$$

are constructed where k is the sampling time interval (which determines the scale, $k < N$) and $m = 1, 2, ..., k-1$. Both m and k are integers. The length of each time series, $L_m(k)$, is defined as

$$L_m(k) = 1/k \times (\frac{N-1}{[\frac{N-m}{k}].k}) \times \sum_{i=1}^{[\frac{N-m}{k}]} |X(m+ik) - X(m+(i-1).k)| \tag{4.8}$$

The average value of $L_m(k)$ over k sets, $L(k)$, is the so-called length of the time series at scale k. This procedure is repeated for each k ranging from 1 to k_{max}. A line is fitted to values of $\ln(L(k))$ versus $\ln(1/k)$ and the slope of this line is considered as the FD. The number of the samples, N, and the nature of the time series determine the optimal value of the parameter k_{max}. We chose the value of k_{max} that resulted in the maximized classification accuracy for tissue typing. We performed a study

[4]Our simulation results also confirmed this finding. When Higuchi's algorithm was used to extract the fractal dimension of time series of length 1,000 originating from a simulated Brownian motion process with theoretical FD=1.5, an unbiased estimate of the FD with a standard deviation smaller than 0.05 was acquired (smaller variances were achievable when longer lengths of simulated time series were used). Similar simulations with Katz's algorithm resulted in biased estimations.

on the separability of the tissue types under fractal dimensions evaluated with k_{max} values between 4 and 56. Based on that study, which will be detailed in Chapter 5, $k_{max} = 16$ was chosen.

4.2 Classical features from B-scan and RF data

Throughout this thesis we have used texture features extracted from ultrasound B-scan images and also, a group of spectral features extracted from single frames of RF data as proposed by Lizzi and Feleppa [55, 130] for comparison with our methodology and also to complement it. A brief description of these feature extraction methods is provided here.

4.2.1 B-scan texture features

Texture features extracted from B-scan images have been extensively used for ultrasound-based tissue typing for diagnostic purposes. Several researchers have used them as the sole set of features [9, 85, 142, 213], other groups have combined them with features extracted from the spectrum of RF signals [182, 186]. In this section, we describe the utilized texture features.

B-scan statistical moments: We computed the first-order statistical moments: mean (M), standard deviation (SD), skewness (Sk) and kurtosis (K), of the intensities of pixels in each ROI. Although these features have been shown to be useful for texture classification [85], addition of second order statistics in form of co-occurrence features can increase the performance of texture-based tissue typing [9, 220].

B-scan co-occurrence features: Co-occurrence matrices of an image are histogram representations, each describing the co-occurrence of a pair of intensities at a certain distance (l) along a certain direction (θ). These matrices are sources for valuable texture features originally proposed in [79]. For feature extraction from gray-scale images, usually only the co-occurrence matrices corresponding to directions $\theta = 0°$ and $\theta = 90°$ are used [9, 213]. Features extracted from these matrices statistically describe the relationships between pixels in the image.

In this work, we used co-occurrence distance of $l = 1$ and directions $\theta = 0°$ and $\theta = 90°$ (vertical and horizontal adjacency). In other words, we calculated the following two co-occurrence matrices for each ROI

$$\theta = 0° \quad : \quad p(I(m,n) = i, I(m \pm 1, n) = j) = \frac{no.\ of\ horizontally\ adjacent\ pixel\ pairs\ with\ values\ (i,j)}{total\ number\ of\ possible\ pairs} \tag{4.9}$$

and,

$$\theta = 90° \quad : \quad p(I(m,n) = i, I(m, n \pm 1) = j) = \frac{no.\ of\ vertically\ adjacent\ pixel\ pairs\ with\ values\ (i,j)}{total\ number\ of\ possible\ pairs} \tag{4.10}$$

The following eight features were extracted from co-occurrence matrices:

Contrast (Cn0, Cn90): A measure of the intensity contrast between a pixel and its neighbors in the image

$$Cn = \sum_i \sum_j p(i,j) \times |i-j|^2 \tag{4.11}$$

Correlation (Cr0, Cr90): A measure of correlation between the intensity of a pixel

and its neighbor

$$Cr = \frac{(\sum_i \sum_j (ij)p(i,j)) - \mu_i \mu_j}{\sigma_i \sigma_j} \tag{4.12}$$

where μ_i and σ_i are the mean and standard deviation of row i in the co-occurrence matrix.

Energy (E0, E90): A measure of the smoothness of the image, also known as the angular second moment

$$E = \sum_i \sum_j p(i,j)^2 \tag{4.13}$$

Homogeneity (H0, H90): A measure of randomness in the image which takes low values for smooth images

$$H = \sum_i \sum_j \frac{p(i,j)}{1 + |i - j|} \tag{4.14}$$

4.2.2 Lizzi-Feleppa features (LF1,LF2,LF3):

In this thesis, we have used the classical ultrasound-based tissue typing features extracted from single RF frames for comparison with the RF time series features in case of our clinical study on human prostate specimens. Lizzi, Feleppa and their colleagues have shown that the intercept extrapolated to zero frequency (LF1), the average slope (LF2), and mid-band value (LF3) of a line fitted to the mid-band portion of the calibrated frequency spectrum of segments of RF A-lines can be used as the signature of cancerous and normal tissue types in prostate [55, 60]. We closely followed the

methodology described in [55] for calibration of the frequency spectrum. In our clinical study involving prostate specimens, the calibration data for Lizzi-Feleppa method was acquired from the surface of a flat glass plate in a water bath at the transducer focal zone, with minimum amplifier gain and flat TGC. A sliding Hamming window was applied to the RF lines, and the squared magnitude of the Fourier transform of the windowed data was computed. The linear fit was computed for the portion of the spectra extending from 3.5 MHz to 9 MHz (the central frequency of the probe was 6.6 MHz). The values of slope and mid-band value were corrected for an assumed linear attenuation coefficient of 0.5 $dB/MHz - cm$ [55] and averaged over the ROI.

It is important to note that although LF features and RF time series features are both computed based on the spectral analysis of echo signals, they are fundamentally different. The LF features are computed based on spectral analysis of segments of RF A-lines in one single frame. RF time series features, on the other hand, are computed based on spectral analysis of temporal samples of RF echoes all originating from the same spatial location in the tissue. In the literature, LF features are commonly referred to as spectral RF features. We chose to call them LF features in order to avoid the confusion with spectral RF time series features.

4.3 Classification methods

In our methodology, each region of interest (ROI) in the tissue is described with a feature vector. In different studies on phantom, animal and human tissue presented in this thesis, the feature vector is composed of RF time series features alone, or in combination with LF and texture features. In this section, we will use $\mathbf{x}$ to refer to the feature vector describing the ROI.

Due to the heterogenous and complex nature of biological tissue, the assumption of a specific statistical distribution for the values of the features is a difficult task in case of tissue typing based on ultrasound echoes. Therefore, we avoid the use of methods such as Bayesian classifiers that rely on a parametric estimation of feature distributions. Instead, we rely on two types of classifiers which take advantage of supervised learning to optimize the parameters of a discriminant model by minimizing the classification error on training data. These methods are multilayer perceptron which belongs to the category of neural networks, and support vector machine (SVM) that belongs to the category of maximum margin classifiers. Neural networks and SVM are nonparametric classifiers [77]. This is due to the fact that they do not rely on any assumption concerning the distribution of features.

4.3.1 Multilayer perceptron network

The general model for classification can be described by a discriminant function of the feature vector, $\mathbf{x}$, of form[5]

$$y(\mathbf{x}, \mathbf{w}) = f\Big(\sum_{j=1}^{M} w_j \phi_j(\mathbf{x})\Big) \tag{4.15}$$

where $f(.)$ is a nonlinear activation function, $\phi_j(\mathbf{x})$ are the basis functions and y stands for the outcome of the classification or the class labels. A neural network is a specific type of this general model. In other words, the neural network model is simply a nonlinear function from a set of input variables, $\mathbf{x}$, to a set of output variables, y [13].

[5]This model is in fact called the linear model of classification [13]. The linearity, however, is with respect to the parameter vector $\mathbf{w}$. The mapping is nonlinear due to the existence of the function f and potentially nonlinear ϕ.

The name "neural network" has its roots in studies that aimed at finding mathematical representations for the mechanism of data processing in biological neural systems [177]. However, for the practical pattern recognition purposes, these biological interpretations are unnecessary. Among different types of neural networks, multilayer perceptron has proven very efficient. The architecture of a multilayer perceptron is composed of a network of processing units, or neurons, arranged as an input layer, an output layer and one or more hidden layers. Each neuron combines its inputs in a linear manner and applies a nonlinear function to the result to generate the input to the next layer. For a two layer perceptron, which is composed of an input, output and a hidden layer, the overall network function can be written as [13]

$$y_k(\mathbf{x}, \mathbf{w}) = g\Big(\sum_{j=0}^{M} w_{kj}^{(2)} g\Big(\sum_{i=0}^{D} w_{ji}^{(1)} x_i\Big)\Big) \tag{4.16}$$

where y_k represents the output of the kth neuron in the output layer ($k = 1, ..., K$), D is the number of input neurons, M is the number of neurons in the hidden layer, parameters of form $w_{ij}^{(1)}$ represent the weight of the connection between the ith neuron in layer (1) with the jth neuron in the next layer. The biases of each connection are also included in the weight vectors. Therefore, the indices of the summations start at 0 instead of 1. A common choice for the function $g(.)$ is the logistic sigmoid function of form

$$g(a) = \frac{1}{1 + (exp(-a))} \tag{4.17}$$

which yields values between 0 and 1. In a two class problem, a single output layer is sufficient and the class label can be decided by rounding the output of the neuron to

the closer number of the set $\{0, 1\}$.

In the training phase, given a set of input vectors $\mathbf{x}_n$ with known output vectors $\mathbf{t}_n$, the intention is to find the set of parameters $\mathbf{w}$ that minimizes an error function. A common error function, which we used, is the mean square error function of form

$$E(\mathbf{w}) = \frac{1}{2} \sum_{N}^{n=1} \|\mathbf{y}(\mathbf{x}_n, \mathbf{w}) - \mathbf{t}_n\|^2 \tag{4.18}$$

The most common solution for solving this optimization problem is the backpropagation technique [178] which was used in this thesis as well. This method involved an iterative procedure. We used the backpropagation technique based on gradient decent. Network weights were initialized with random values and then changed in the direction that reduced the error. The details of the backpropagation algorithm can be found in the original reference [178] or any pattern recognition text [13]. The stopping criteria for the training process was determined by monitoring the learning curve which depicts the value of the objective function *vs.* the number of iterations.

4.3.2 Support vector machines

Support vector machines belong to the family of maximum margin classifiers. Using a kernel function, SVM maps the input data to a higher dimension space where a hyperplane can separate the data in different classes. The process of training a SVM classifier is equivalent to finding this optimal hyperplane in a way that minimizes the error on the training dataset and maximizes the perpendicular distance between the decision boundary and the closest data points in the classes [216]. In a two-class case, if the training dataset consists of N feature vectors $\{\mathbf{x}_1, ..., \mathbf{x}_N\}$ with class labels $y_i \in \{1, -1\}$, then the SVM training problem is equivalent to finding W and b such

that [13]

$$1/2 \times W^T W + C \sum_{i=1}^{i=N} \xi_i \tag{4.19}$$

is minimized subject to

$$y_i(W^T \phi(\mathbf{x}_i) + b) \geq 1 - \xi_i \tag{4.20}$$

where $\xi_i \geq 0$ are the so-called slack variables that allow for misclassification of noisy and difficult data points, and $C > 0$ controls the trade-off between the slack variable penalty and the margin [13]. The function $\phi(.)$ maps the data to a higher dimensional space. This new space is defined by its kernel function: $K(\mathbf{x}_i, \mathbf{x}_j) = \phi(\mathbf{x}_i)^T.\phi(\mathbf{x}_j)$. The above problem can be formulated as a quadratic optimization process. The details of the solution, as used in our methodology, and its implementation can be found in [47]. For the choice of kernel type, we examined linear, sigmoid, polynomial and Gaussian Radial Basis Function (RBF) kernels. We chose the RBF kernel which is defined as

$$K(\mathbf{x}_i, \mathbf{x}_j) = e^{-\gamma \|\mathbf{x}_i - \mathbf{x}_j\|^2} \tag{4.21}$$

This choice was due to two reasons: 1) The RBF kernel has only one parameter ($\gamma > 0$) to adjust. This means that the process of tuning the SVM classifier to a specific problem is limited to finding the appropriate values for two parameters: C and γ; 2) we found SVM classifiers based on RBF kernel more accurate in case of detection of prostate cancer in our dataset.

We used the publicly available C++ implementation of the SVM algorithms known as LIBSVM [47]. The entire dataset was normalized prior to training by setting the maximum value of each feature to 1 and the minimum to 0. For parameter selection

(C and γ), exhaustive search was performed. The details will be provided along with the description of the experiments in future chapters.

4.3.3 Posterior class probabilities for cancer distribution maps

In this section, we explain the methodology used to generate the posterior class probabilities of tissue ROIs classified with the SVM method. These probability values were used to generate cancer distribution probability maps. Unlike some statistical classification methods such as the Bayesian classifier, SVM is merely a decision machine: If $f(\mathbf{x}_n) = W^T\phi(\mathbf{x}_n) + b > 0$, then the class label for $\mathbf{x}_n$ is $y_n = 1$. In other words, SVM does not provide posterior class probabilities ($P(class|input)$). In order to generate the cancer distribution probability maps and also Receiver Operating Characteristic (ROC) curves for our human study, we needed posterior probabilities of normal and cancer classes

$$P_c(\mathbf{x}_n) = p(y = 1|f(\mathbf{x}_n)) \tag{4.22}$$

where $P_c(\mathbf{x}_n)$ stands for probability of $\mathbf{x}_n$ being cancerous and $P_{nor}(\mathbf{x}_n) = 1 - P_c(\mathbf{x}_n)$. Platt [166] has extended SVM for probability estimates. Platt's method trains an SVM and then, trains the parameters of an additional sigmoid function of form

$$P_c = (y_n = 1|f(\mathbf{x}_n)) = \frac{1}{1 + exp(Af(\mathbf{x}_n) + B)} \tag{4.23}$$

to map the values of $f(\mathbf{x}_n)$ to posterior probabilities. The values of parameters A and B are fit using maximum likelihood estimation from the training set for which the actual labels are known [166, 228]. We used class probabilities generated with this method for creating the probabilistic cancer maps.

4.3.4 Receiver Operator Characteristic

The performance of computer-aided diagnosis methods is usually expressed with measures including accuracy, specificity, sensitivity, and Receiver Operator Characteristic (ROC) curves. In this section, we provide definitions of these measures. In case of the ROC curve, we will provide a description of our method for creating ROC curve based on SVM outcomes. It should be noted that throughout this thesis, measures of performance are presented based on the number of ROIs in the test set. In other words, if in a certain classification experiment an accuracy of 80% is reported, then 80% of the ROIs in the test set have been correctly classified.

The sensitivity and specificity are indicators of the frequency of correct diagnosis in subjects (ROIs in our experiments) with and without the disease, respectively. Mathematically they can be expressed as [152]

$$se = \text{sensitivity} = \frac{\text{true positives}}{\text{Number of positive cases in the test set}} \tag{4.24}$$

$$sp = \text{specificity} = \frac{\text{true negatives}}{\text{Number of negative cases in the test set}} \tag{4.25}$$

where true positive refers to the number of ROIs correctly classified as positive (cancerous) and true negative refers to the number of ROIs correctly classified as negative. In any detection/diagnosis study, there is a simple or composite parameter based on which the "critical value" or "decision boundary" is determined. There always exists a trade-off between having high specificity and high sensitivity values depending on the chosen threshold. Therefore, the sensitivity of diagnosis or detection method should always be assessed along with its specificity. One method to assess the diagnostic value of a test and to define an appropriate decision boundary, is the ROC

curve analysis. ROC curve is a plot of sensitivity against specificity which is derived by varying the decision boundary and measuring sensitivity and specificity for each threshold value[6]. Conventionally, specificity is plotted along the abscissa and sensitivity is plotted along the ordinate [46]. A desirable test is one for which sensitivity rises rapidly without a major decrease in specificity. The area under an ideal ROC curve is therefore close to 1 when specificity and sensitivity are expressed in $[0, 1]$ interval.

In case of SVM classification which was the method of choice in our clinical study, the posterior cancer probability (P_c computed using the method described in Section 4.3.3) was used to determine the decision boundary (t) used for plotting the ROC curve. In other words, an ROI was classified as cancerous if $P_c > t$. The value of t was incrementally increased from 0 to 1 with steps of size 0.001. For each step, sensitivity and specificity values were calculated. The area under the ROC curve was then calculated as follows [184]

$$A_{ROC} = \frac{1}{2}\Big(\sum_i (se_i + se_{i-1})(sp_{i-1} - sp_i)\Big) \tag{4.26}$$

where se_i and sp_i were the sensitivity and specificity corresponding to point i on the ROC curve. The area under the ROC curve was used as the primary measure for evaluation of the classification performance in our clinical study.

[6]Many researchers prefer to plot sensitivity versus 1-specificity which is called Probability of False Alarm (PFA).

4.3.5 The choice of the classifier

The classification method of choice for our animal studies was neural networks. It was noted that very simple architectures of neural networks, such as the two layer model described in Section 4.3.1, provide very high classification accuracies. However, for the case of the clinical study, we used the SVM classifier. This was due to the practical advantages of the SVM to the neural networks, including: 1) A systematic method for choosing the best architecture of neural network for a specific problem is outstanding. In case of SVM, on the other hand, the tuning of the classifier is equivalent to finding the values of only two parameters through a sparse search on a large interval followed by a more exhaustive search on a smaller subset. 2) Although for both neural network and SVM classifiers the training process involves nonlinear optimization, it can be shown that the objective function in case of the SVM training is convex [13]. Therefore, the solution of the optimization problem is more straightforward and the training goal is achieved in a significantly shorter time.

The cancer distribution probability maps reported in Chapter 6 were created using the SVM classification method based on the posterior class probability estimation method described in Section 4.3.3.

4.4 Chapter summary and conclusions

In this chapter we discussed the methods utilized in the thesis for extraction of tissue typing features from ultrasound RF time series. We introduced the spectral and fractal parameters used to characterize RF time series received from tissue. We also briefly described a set of B-scan texture features and spectral features extracted

from single frames of RF data proposed in the literature for ultrasound-based tissue typing. These features will be used for comparison with and also for complementing the performance of our novel RF time series features in Chapter 6. Further, we provided details of the multilayer perceptron neural network and SVM classification methods used for tissue typing in the current work.

Chapter 5

Phantom and Animal Studies

In this chapter, we provide experimental evidence, based on phantom and animal studies, showing that the ultrasound RF time series can be used for tissue typing within a pattern recognition framework that utilizes training supervised classifiers such as neural networks and support vector machines. In the phantom studies, we examine the capabilities of RF time series features in distinguishing tissue mimicking phantoms, with difference only in the size of cell-mimicking microscopic glass beads. Prostate tumors are composed of immature and "small cells" which lack structural organization [114]. Previous studies have shown that the size and the microstructure of the sub-wavelength particles affect the backscattered signals [107] and the spectral parameters extracted from single RF frames [131], and are likely to be among important factors in the success of ultrasound-based tissue typing methods. Therefore, in our phantom studies, we model the cell sizes as one of the differences between the cancerous and normal tissue, and examine the success of our proposed tissue typing approach in separation of the phantoms with different cell sizes.

Once the basic idea of utilizing RF time series features for tissue typing was

examined on phantoms, we performed animal studies involving tissue types of different microstructure to extend the methodology to biological tissues. In the animal studies, we acquired RF time series from four different types of animal tissue, computed the proposed features for Regions of Interest (ROIs) of the tissue, and utilized them along with a neural network classifier for tissue typing. It should be noted that although successful differentiation of the animal tissue types does not directly imply the usefulness of the proposed method on the real clinical applications, it provides experimental support for the central idea of this thesis.

As part of this animal study, we also examined the RF time series acquired from a high-frequency ultrasound machine operating at the central frequency of 55 MHz. It is a well-known fact that at very high frequencies the scattering of ultrasound is primarily caused by the cellular microstructure [64] as opposed to tissue macrostructure. Therefore, the dependence of the RF time series features on cellular microstructure should be more evident in high-frequency data. The results of our animal study confirmed this hypothesis.

We also compared the tissue typing performance of the proposed method with B-scan texture characterization. The 12 texture features introduced in Section 4.2.1 provide a conventional approach to ultrasound-based tissue typing. The results of our comparative study demonstrated that the new approach outlined in this thesis is more accurate for tissue typing.

5.1 Methodology of the phantom study

Since the microstructural changes in cellular structure of tissue are important indicators of cancer formation, they are likely to be the source of tissue typing information

in RF time series as well. An important microstructural feature of tissue is the cell size. To determine the effects of cell size on RF time series, we acquired and studied ultrasound RF time series from custom tissue mimicking phantoms with varied microscopic particle sizes.

5.1.1 The phantoms

We built tissue mimicking phantoms in the form of gelatin-agar based suspensions [12, 135]. Microscopic glass beads with known distributions of particle sizes were added to study the effects of cell size. Gelatin and agar (Sigma Aldrich, Canada, Oakville, ON) were mixed in distilled water in room temperature and while being constantly stirred, were heated to $90°C$ at which point glass beads (Potters Industries, Parsippany, NJ) were added. Small quantities of bleach were added to avoid bacterial growth in the phantoms [44]. The resulting mix was slowly cooled down to the room temperature, while being stirred. When reached to the room temperature, the suspension was transferred to a plastic box and stored overnight in a cooler. The ultrasound data was collected the next day.

The dry weight percentages of ingredients used in the utilized phantoms are given in Table 5.1. Two different types of phantoms were built which shared the same recipe, with the only difference being the size of microscopic glass beads. The two types of utilized glass beads were of average diameter of 35 μm (Potters Industries catalog number: 3000E) and 11 μm (Potters Industries catalog number: 5000E). It is notable that prostate PC-3 cell line has a mean diameter of 26 μm [107]. The detailed distribution of bead sizes in 3000E and 5000E materials are provided in Table 5.2.

The physical properties of the phantoms (such as density, elasticity, and speed

Table 5.1: Dry weight percentage of the various components in the particle size phantoms.

Component	Weight %
Agar	1.17
Gelatin	3.6
Glass beads	6
Bleach	0.25
Water	88.98

of sound) were similar. This was important since the phantoms were intended to be different only in terms of cell sizes. The 3000E and 5000E materials have very close untapped densities (101 *vs.* 99 lbs/ft^3). The resulting phantoms, also had very similar elastic properties. The stress-strain curves acquired using an Instron 5500R materials test system, are depicted in Figure 5.1. Since the speed of sound is related to density and stiffness ($c = \sqrt{C/\rho}$ where C is the coefficient of stiffness and ρ is the density [81]), the similar values of elasticity and density mean that the speed of sound should also be similar in the two types of phantoms.

For cross-validation purposes, two copies of the 3000E phantom and two of the 5000E phantom were built (four phantoms in total). It should be noted that the B-scan images acquired from the two types of the phantoms appeared very similar (Figure 5.2)[1].

A cylindrical opening was created in the phantoms just before congealing by inserting a plastic pipe into one corner of the holding boxes. Before imaging, this pipe was removed carefully and the transrectal ultrasound probe (BPSL9-5/55/10, center frequency: 6.6 MHz) was inserted vertically into the hole left behind and was fixed

[1]Not surprisingly, an attempt to distinguish the 3000E phantoms from 5000E phantoms based on B-scan texture features described in Section 4.2.1 failed with an acquired accuracy of just below 60%. The SVM classification approach was used in this test.

Table 5.2: The distribution of particle sizes in glass beads used in particle size phantoms.

	3000E	5000E
10% finer than	18 μm	3 μm
50% finer than	35 μm	9 μm
90% finer than	65 μm	38 μm
Mean value	35 μm	11 μm

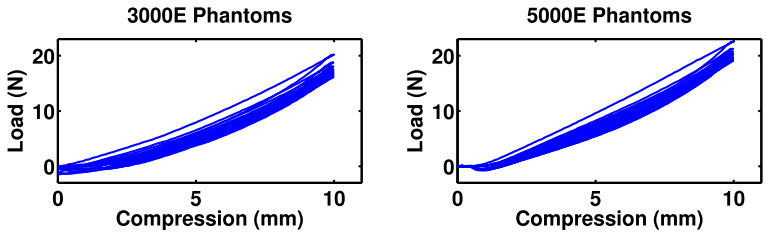

Figure 5.1: The stress-strain curves for the particle size phantoms.

with a standing clamp (Figure 5.3). The data was collected using a Sonix RP (Ultrasonix Inc., Richmond, BC, Canada) ultrasound machine. To form the RF time series, we acquired 128 frames of RF data from eight different cross sections within each phantom. Therefore, the length of RF time series in our analysis of phantom data was 128. The data was acquired at 22 frames per second (fps). A single transmit focal point was set at 1.5 cm and only data from the focal zone (1 cm on each side of the focal point) were used for feature extraction and classification experiments. The RF sampling rate was 20 MHz and the number of bits per RF sample was 16.

5.1.2 Feature extraction and classification

We extracted the RF time series features from areas of interest (ROIs) of size 1 $mm \times$ 3.5 mm (this was chosen to match the ROI size in our human study of Chapter 6).

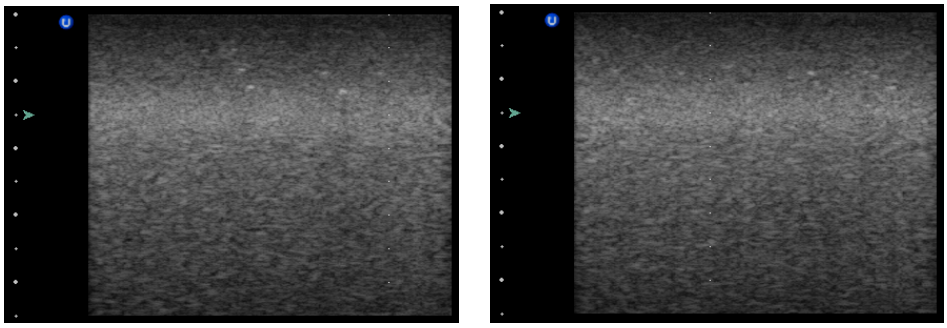

(3000E) (5000E)

Figure 5.2: The typical B-scan images of 3000E and 5000E phantoms. The textures appear to be visually identical.

This included four segments of RF lines, each of length 96 samples. In other words, each ROI was formed by 384 RF time series, each of length 128. A total of 2624 ROIs of each phantom type were available which almost equally originated from the two versions built from each phantom type. Six spectral RF time series features (S1,S2,S3,S4,S5,S6) were extracted from the ROIs and used for separation of the phantoms (the description of these features were provided in Section 4.1)[2].

For classification, we compared the performance of the neural networks and SVM classifiers. Multilayer perceptrons with two and three hidden layers and 3-11 neurons in each of the hidden layers were examined first. The best performing neural network classifier was the architecture with one hidden layer and five neurons in that layer. We also examined the SVM classifier with the Gaussian RBF kernel. For parameter selection (C and γ, see Section 4.3.2), we exhaustively searched the parameter space $C \in \{2^{-10}, 2^{-9}, ..., 2^{10}\}$ and $\gamma \in \{2^{-10}, 2^{-9}, ..., 2^{10}\}$. For each set of parameters, 10-fold

[2]In case of the phantom study, the addition of the FD to the features did not result in a significant change in the classification accuracies. In the animal study, on the other hand, the FD played an important role.

Figure 5.3: Data collection setup for phantom studies.

cross-validation was performed to determine the best SVM parameters. The values of $\gamma = 4$ and $C = 0.25$ were used.

5.2 Results of the phantom study

As previously stated, we made two copies of the 3000E and two copies of the 5000E phantom (3000E1, 3000E2, 5000E1, 5000E2). We performed six sets of classification experiments using these phantoms.

Experiment 1 - train on 3000E1 *vs.* 5000E1, test on 3000E1 *vs.* 5000E1: In this experiment, the classifier was trained to separate RF time series ROIs from 3000E1 and 5000E1 phantoms. The classifier was trained on a portion of the data from 3000E1 and 5000E1 phantoms and tested on a different portion of the data from

those phantoms. Eight cross sections of RF time series data were available from each phantom. The experiments were performed with a leave-one-out approach. In other words, the classifier was trained on data from seven cross sections of the 3000E1 data *vs.* seven cross sections of the 5000E1 data and tested on one cross section of 3000E1 *vs.* 5000E1. The process was repeated for all eight cross sections.

Experiment 2 - train on 3000E2 *vs.* 5000E2, test on 3000E2 *vs.* 5000E2: This was similar to experiment 1, however, data from 3000E2 and 5000E2 phantoms was used.

Experiment 3 - train on 3000E1 *vs.* 5000E1, test on 3000E2 *vs.* 5000E2: In this experiment, the classifier was trained on data from 3000E1 and 5000E1 phantoms and was tested on separating the ROIs of 3000E2 from 5000E2 phantoms. All ROIs from 3000E1 and 5000E1 were used for training and all ROIs from 3000E2 and 5000E2 were used for testing.

Experiment 4 - train on 3000E2 *vs.* 5000E2, test on 3000E1 *vs.* 5000E1: This was similar to experiment 3, only the training and testing sets were switched.

Experiment 5 - negative control 1: In this experiment, the classifier was trained to separate 3000E1 ROIs from 3000E2 ROIs. Half of the data from each of these phantoms were used for training and the other half was used for testing.

Experiment 6 - negative control 2: In this experiment, the classifier was trained to separate 5000E1 ROIs from 5000E2 ROIs. Half of the data from each of these phantoms were used for training and the other half was used for testing.

The results of experiments 1 and 2, when a SVM classifier was used, are presented in Table 5.3 averaged together as the intra-phantom trials. The average accuracy, sensitivity and specificity (with 5000E defined as the positive detection), were 80.5%,

79.8% and 81.1%, respectively. It was noted that the results from the neural network classification were slightly less accurate (accuracy of 78±6.9% on a feedforward network with five neurons in a single hidden layer).

The results of experiments 3 and 4, when a SVM classifier was used, are presented in Table 5.3 averaged together as the inter-phantom trials. The accuracy slightly dropped to 79% compared to the intra-phantom experiments. This was expected due to the fact that the training and testing data in inter-phantom trials were from physically different versions of 3000E and 5000E phantoms.

As Table 5.3 shows, the average accuracy of the negative control tests where the two classes of ROIs originated from the same phantom types, was 58%. In other words, physically different phantoms which had similar cell sizes were very poorly distinguishable from each other based on the proposed tissue typing approach. Since the phantoms were custom made, small structural differences between the phantoms of the same type were inevitable.

The results showed that RF time series acquired from tissue mimicking phantoms with difference only in the size of cell-mimicking particles were distinguishable with statistically reliable accuracy of 80.5%. The low accuracy of the classification acquired on the negative control experiments involving phantoms with identical cell sizes showed that the method is in fact sensitive to the cell size.

The phantom study reported here focused only on one of the possible differences between cancerous and normal tissue, namely cell size. Tissue properties such as elasticity or vascularity also change during formation of cancer. Based on a small study which involved agar and gelatine-based phantoms with different levels of stiffness, we can not confirm that RF time series features are sensitive to elasticity.

Table 5.3: Classification results on particle size phantoms: 3000E versus 5000E phantoms. Analysis of variance (ANOVA) test confirmed that the classification of ROIs in both intra-phantom and inter-phantom experiments was significantly more accurate than the classification in negative control experiment ($p < 0.001$).

	Accuracy (std)	Sensitivity	Specificity
Intra-phantom (experiments 1 and 2)	80.5% (6.2)	79.8% (5.9)	81.1% (6.6)
Inter-phantom (experiments 3 and 4)	79% (3.1)	77.5% (3.1)	82.6% (3.5)
Negative control (experiments 5 and 6)	58% (7.1)	62.5% (6.1)	60.3 % (6.9)

5.3 Methodology of the animal study

5.3.1 Tissue types

We used four animal tissue types which were all available from butcher-shop cuts. They were: bovine liver, pig liver, bovine muscle, and chicken breast. As illustrated in Figure 5.4, the cellular structure of both bovine and pig liver are characterized by hepatocyte cells (of slightly different shape and density), whereas bovine muscle and chicken breast both have fibrous structures.

These significantly different cellular microstructures do not translate to distinct appearances on ultrasound B-scan images. To quantitatively validate this claim, we performed a simple "visual inspection test". We asked seven graduate students, who were all familiar with ultrasound imaging, to train themselves by looking at five ultrasound B-scan images acquired from the cross sections of each of the four tissue types used in this study. Students were given up to half an hour to review these 20 images. Immediately after training, they were given 20 new images in a random order and were asked to associate them to one of the four classes. The average performance of the human inspectors in this simple test was 71.7% and they all complained about

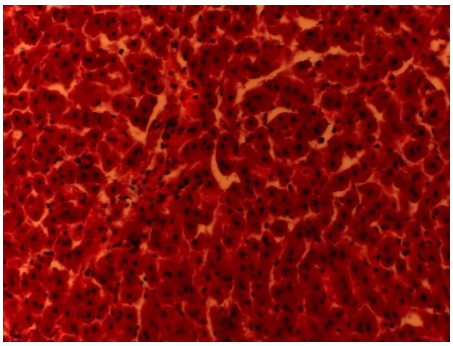

(a: Bovine liver)

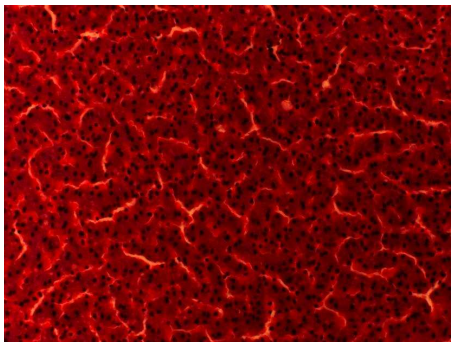

(b: Pig liver)

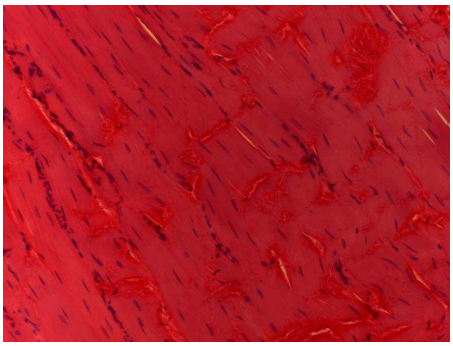

(c: Chicken breast)

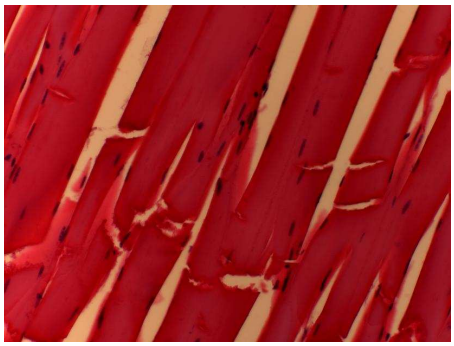

(d: Bovine muscle)

Figure 5.4: Images of the cellular structure of tissue types used in this study at 200X magnification (acquired from H&E stained slides with a Zeiss AxioImager M1 microscope).

the lack of a simple pattern that distinguishes the tissue types[3]. In other words, the studied tissue types are not readily distinct on ultrasound images. This is in fact similar to the situation in clinical problem of cancer detection which is our ultimate goal for developing a tissue typing method.

[3]This result is not directly comparable to the results of the computer-aided methods described in this thesis, mainly because the computer-based methods classify regions of interest of the tissue and not the entire images. Furthermore, one should notice that while this visual classification is a four-class problem, most of our analysis in this chapter considers pairwise tissue typing.

5.3.2 Data collection

The experiments were performed on data acquired with two different imaging systems: an ultrasound machine operating at the typical clinical frequency of 6.6 MHz and a high-frequency machine operating at 55 MHz. The data collection procedures and specifications of the two datasets were as follows:

Data acquired at 6.6 MHz

We used a Sonix RP (Ultrasonix Inc., Richmond, BC, Canada) ultrasound machine to collect RF echo signals. The ultrasound probe was a BPSL9-5/55/10 transrectal probe which generates ultrasound signals with wide-band spectrum. The centeral frequency was set to 6.6 MHz. The depth of imaging was set to 2 cm.

From each of the four tissue types, we scanned 10 cross sections, where each cross section was from a different butcher-shop piece of that tissue (40 cross sections in total, each coming from a different animal). We took numerous measures to ensure that the differences of RF time series collected from various tissue types do not originate from alterations in the imaging conditions. The probe was placed in direct contact with the tissue and only one transmit focal point was set at depth 0.5 cm in all cases. The tissue was firmly suspended in a water bath and prior to scanning we measured the temperature of water to make sure that all tissue types were scanned at temperature range of $22-23°$C. Furthermore, after mounting each tissue piece and positioning the probe at the imaging position, we waited until the level of water became completely calm. We used distilled water and changed the contents of the water bath after scanning each tissue cross section. Figure 5.5 shows our data collection setup.

(a) **(b)**

Figure 5.5: Experimental setup for collection of data at 6.6 MHz, (a) A close-up of the tissue mounted in the water bath and the transrectal probe, (b) Ultrasound machine and the scanning water bath.

To form the RF time series, we continually acquired 127 frames[4] of RF data, at the rate of 27 frames per second, from each cross section of the tissue. In other words, the length of the time series was set to 127. Each frame of the RF data consisted of 256 A-lines. An ROI in our classification experiments corresponded to an area of 3.5 mm^2 of the tissue or equivalently an 8×96 window in the RF data. The number of ROIs from different tissue types included in the classification experiments ranged between 368 and 400.

In this chapter, we compare the performance of our proposed methodology with the performance of texture features extracted from the B-scan images. A B-scan image of each cross section, which was constructed from the first RF frame in the time series, was used for this purpose. The equivalent ROI size in the B-scan image was 8×8 pixels.

[4]At the time of acquisition of this dataset, we were limited to 127 frames for technical reasons. The RF time series were zero-padded to 128 for computation of the DFT-based features.

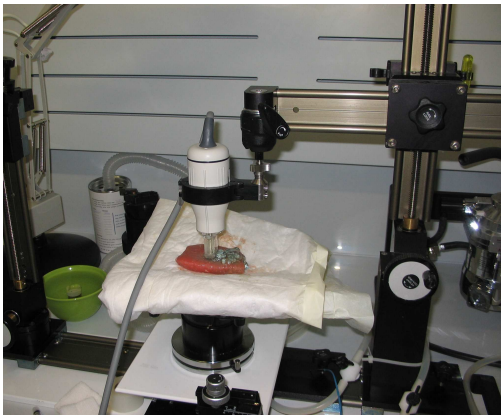

Figure 5.6: The scanning setup and the probe used for the high-frequency study.

Data acquired at 55 MHz

The high-frequency RF time series in this study were collected using a Vevo 770 high-resolution ultrasound system (VisualSonics Inc., Toronto, Canada) with the RMV711 scanhead (Figure 5.6). The probe central frequency was 55 MHz which provided an axial resolution of 30 μm. The scanhead featured a single crystal and we operated it in A-scan mode. The depth of scanning was about 1 mm which corresponded to 512 signal samples. While the tissue and the probe were fixed in place, we continually acquired 500 ultrasound A-lines (frame rate: 60 fps) from one spot of the tissue. In other words, we formed RF time series of length 500 from each sample of each A-line. We acquired time series corresponding to two separate A-lines from two different areas of each tissue type. The tissue typing features were extracted from single time series of RF samples and averaged over segments of length 10 samples (20 μm). 100 ROIs of each tissue type were available in our high-frequency dataset.

5.3.3 Feature extraction and classification

In total, we utilized seven RF time series features: fractal dimension and six simple parameters extracted from the magnitude of the Discrete Fourier Transform (DFT) of RF time series. The detailed description of the seven RF time series features (S1,S2,S3,S4,S5,S6,FD) were provided in Section 4.1.

For selection of the k_{max} value for computation of the fractal dimension, we performed a study on the separability of the tissue types under fractal dimensions evaluated with k_{max} values between 4 and 56. The results of that study showed that k_{max} values between 8 and 20 yield FD values that can be used for separating tissue types types with a peak in performance at $k_{max} = 16$. Therefore, $k_{max} = 16$ was used for computing the fractal dimension.

For evaluation and comparison, we used 12 texture features computed from B-scan images constructed from the first frame in the RF time series for data acquired at 6.6 MHz. The texture features were used for typing of the four animal tissue types and the results were compared to the performance of the proposed RF time series features. Since our high-frequency data was acquired at A-scan mode, no texture feature analysis was performed at high-frequency. The description of the 12 texture features used in the study (M,SD,Sk,K,E0,E90Cn0,Cn90,Cr0,Cr90,H0,H90) were provided in Section 4.2.1.

We used feedforward multi-layer perceptron networks for tissue classification[5]. To determine the architecture of the neural network, we studied networks with one and two hidden layers. We found that the networks with a single hidden layer yield higher

[5]The choice of the neural network classifier was merely based on the fact that a simple structure of multilayer feedforward network provided a universally satisfactory performance in our animal studies. Therefore, we did not explore other types of classifiers for this purpose.

accuracies. Also, we examined networks with one hidden layer with different number of neurons in the hidden layer (3-11 neurons). We found that the performance of the neural network is maximized with seven neurons when used with the RF time series features, and with five neurons when used with the texture features. We defined the transfer functions of the neurons in the networks as log-sigmoid and used the Levenberg-Marquardt backpropagation algorithm for supervised training of the classifier.

We used a leave-10%-out strategy for training and testing the networks and for validation of the results. In other words, in each experiment, we randomly divided the data from the two tissue types involved in the classification to 10 folds. We trained the network on 90% of the data samples and tested it on the remaining 10%. We repeated this procedure for all 10 portions of the data. The test accuracies from 10 portions were averaged. This result is not independent from the random process of splitting the data in 10 parts. Therefore, we repeated the leave-10%-out process 50 times, each time with a different random partitioning of the data in 10 parts. We report the mean and standard deviation of the outcomes of these 50 trials on test portion of the data.

5.3.4 Feature selection

There are several reasons for reducing the size of the feature vector used for classification. Apart from increased computational complexity, unnecessary inputs also reduce the generalizability of the trained classifier which translates to reduced test accuracy. In pattern recognition literature, the complications introduced in classifier design by the large number of features is referred to as "the curse of dimensionality" [208].

We used the exhaustive search algorithm to find the best subset of features for tissue typing. The computational complexity of exhaustive search for feature selection exponentially grows with increasing size of the feature space [208]. To choose the optimal subset of features from an n-dimensional feature space, one needs to examine $2^n - 1$ different subsets. This adds up to 127 subsets in case of the seven-dimensional RF time series features, and to 4095 subsets in case of 12 B-scan texture features. We had access to a high end parallel computing server (Sun Microsystems, Sun Fire V890) which made the exhaustive search possible. We performed our entire process of leave-10%-out training and validation, detailed in the next subsection, for all six pairs of tissue types and for all of the possible combinations of features (separately for time series and texture features). We ranked the combinations based on accuracy of classification on validation data, for each pair of tissue types, and found the best subsets of n features, $1 \leq n \leq 7$ for RF time series features and $1 \leq n \leq 12$ for texture features.

5.4 Results of the animal study

5.4.1 Results at 6.6 MHz

In this section, we first provide a detailed analysis of the performance of the seven proposed RF time series features in pairwise tissue typing at 6.6 MHz. This includes results of analysis of the performance of each of the seven features separately, and the optimal feature subsets at different dimensions (one to seven) for all six pairs of tissue types. The outcomes will be compared with the results acquired using the texture features. We will also present the classification results on data acquired at 55 MHz

Table 5.4: The best performing single features extracted from RF time series at 6.6 MHz.

Tissue types	Best ***single*** feature	Classification accuracy (STD)
Bovine liver - chicken breast	FD	74.3% (1.7)
Bovine liver - bovine muscle	FD	90.2% (4.7)
Chicken breast - pig liver	FD	72.2% (2.2)
Pig liver - bovine muscle	S6	82.4% (3.1)
Bovine liver - pig liver	FD	74.1% (1.8)
Chicken breast - bovine muscle	FD	82.8% (2.8)

Table 5.5: The second best performing single features extracted from RF time series at 6.6 MHz.

Tissue types	Best ***single*** feature	Classification accuracy (STD)
Bovine liver - chicken breast	S6	72.3% (2.7)
Bovine liver - bovine muscle	S6	84.2% (3.1)
Chicken breast - pig liver	S6	70.3% (2.1)
Pig liver - bovine muscle	FD	79.1% (2.2)
Bovine liver - pig liver	S6	72.1% (2.8)
Chicken breast - bovine muscle	S6	75.1% (1.8)

to examine the effects of increasing ultrasound frequency. In all tables in this section, accuracy values are averaged over 50 times of execution of the leave-10%-out cross-validation process and are followed by the standard deviation of the accuracy values in parentheses.

Best single features: FD and S6

Tables 5.4 and 5.5 list the best performing and the second best performing single features for the six different tissue type pairs. Fractal dimension showed the best performance in five cases with S6 (slope) following it closely. In case of pig liver versus bovine muscle, S6 performed more accurately. From Table 5.4, it is notable that tissue typing accuracies in range of 74-90% are achievable using a single feature.

While S1-S4 are each governed by limited frequency bands in the spectrum of the

time series, FD and S6 are features that best represent the general behavior of the time series. Therefore, they carry more information about the RF time series, and not surprisingly, provide the best classification results.

Figures 5.7 and 5.8 show the distribution of the values of S6 and FD for the four different tissue types in histogram format. In case of bovine muscle versus pig liver, as Figure 5.8 illustrates, the histograms of the FD values were very similar. In this case the single feature of choice was S6.

As a nonlinear classifier, the neural network maps the data to higher dimensions for extraction of the decision planes. Therefore, we acquired relatively high accuracies even in cases where the histograms of the FD values were fairly similar (*e.g.* chicken breast versus pig live). It was however evident that one single feature was not universally sufficient for separating these tissue types.

Best combinations of RF time series features

The exhaustive search executed on all possible combinations of the seven proposed features showed that in all six tissue pairs, the tissue typing accuracy had a peak when four or five features were used. For each tissue type, Figure 5.9 shows the mean and standard deviation of the accuracy of classification acquired from the best combination of one to seven features. It is clear that in all cases, increasing the size of feature vector to six or seven is unnecessary or even detrimental.

Table 5.6 provides the list of the four or five features that were selected as the optimal subset for each tissue type pair. It should be noted that FD and S6 appeared in the optimal feature vector in all and five out of six experiments, respectively. S1,S2,S3, and S4 did not show a significant difference in terms of class separability

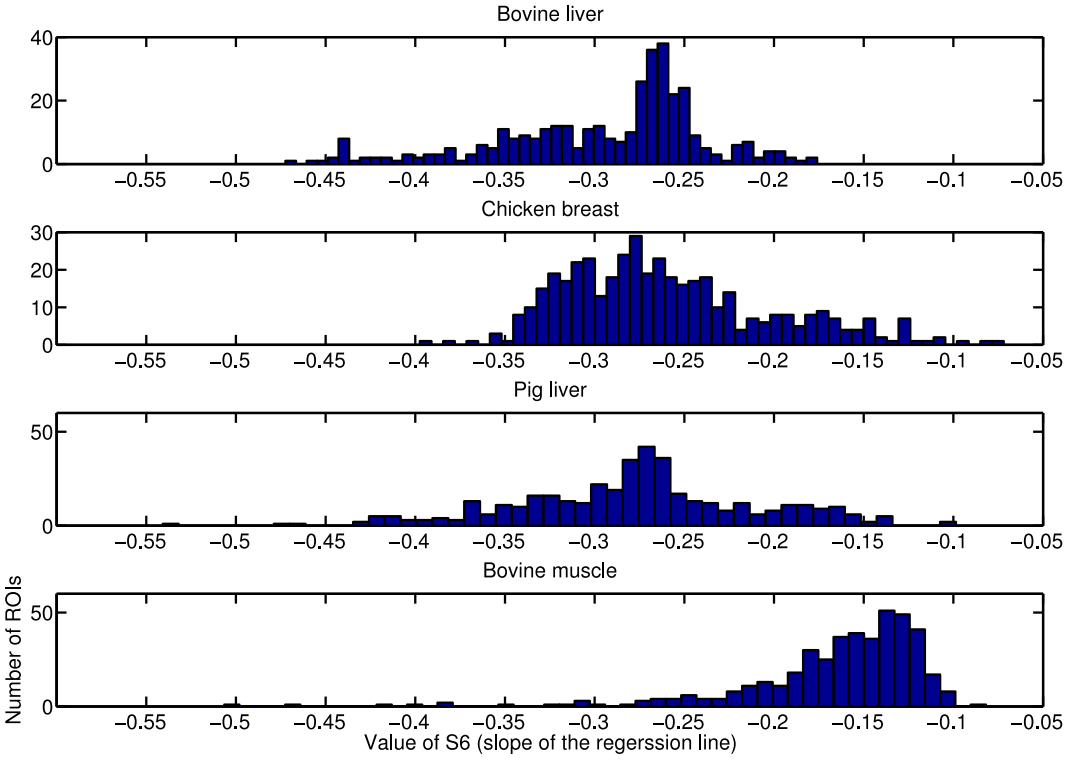

Figure 5.7: Distribution of the values of the feature S6 (slope of the regression line) in different tissue types.

from each other. These features characterize specific bands of the frequency spectrum of RF time series. We conclude that the tissue typing information of RF time series is not specific to certain frequency bands; therefore, parameters such as FD and S6 which provide a general view of the behavior of RF time series are the best tissue typing features.

Table 5.6 shows that with a set of features selected from the seven proposed features, tissue typing accuracies ranging between 91% (bovine muscle versus chicken breast) and 98% (bovine muscle versus bovine liver) can be acquired. The average over all six tissue pairs was 95.1%.

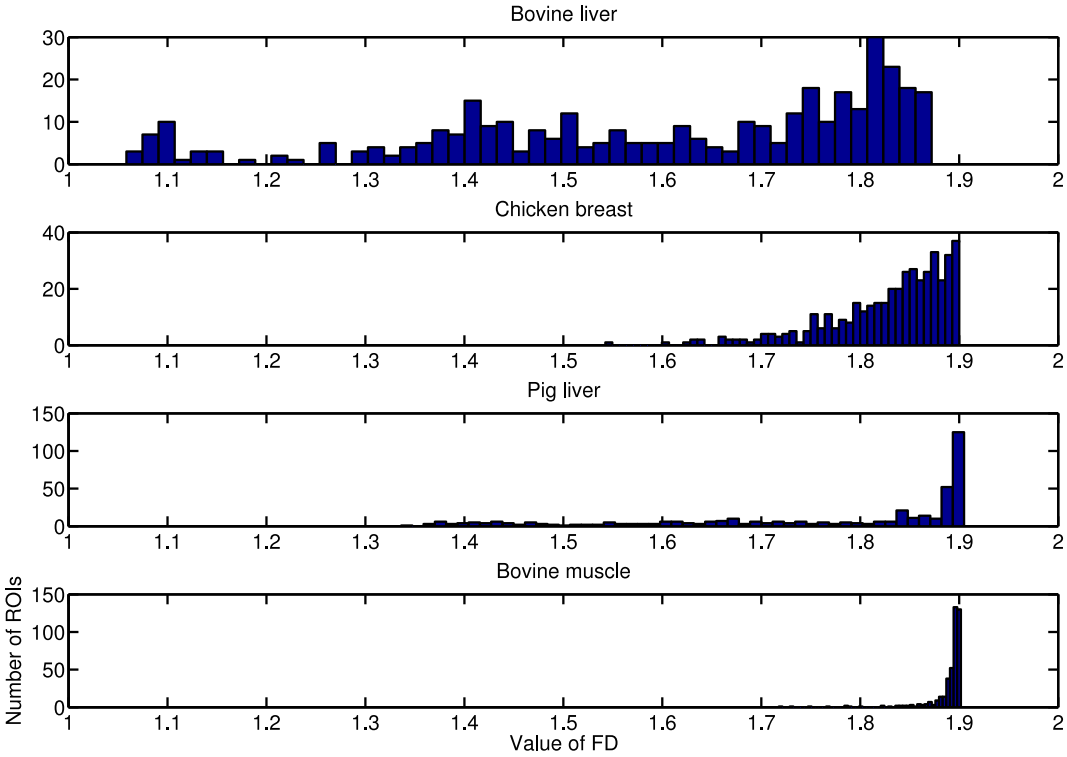

Figure 5.8: Distribution of the values of the feature FD (fractal dimension) in different tissue types.

Four-class classification

In a separate experiment, we used the seven proposed features along with a feedforward neural network classifier to perform four-way tissue typing. Data from all four tissue types were used for training and the network was tested on all four classes as well. The network architecture consisted of a hidden layer with 5 neurons, and two neurons in the output layer which was sufficient to code the four possible outcomes. For this experiment, we used 75% of the data from each tissue type for training and 25% for testing. The training-testing procedure was performed 100 times with different random selections of train and validation data and the test accuracies were

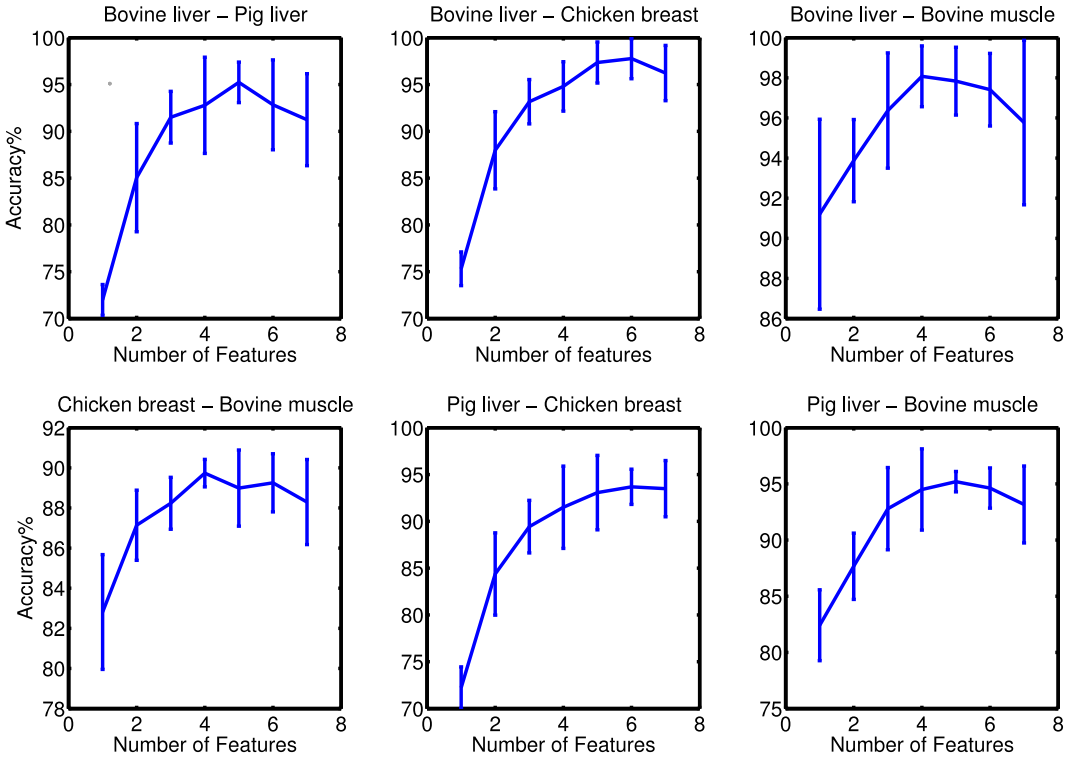

Figure 5.9: Performance of the best feature vectors of different sizes in tissue typing. The Error bars denote ± one standard deviation (over 50 leave-10%-out trials).

averaged. An average accuracy of 86.5% with a standard deviation of 7.2% was acquired.

Performance of B-scan texture features

For evaluation and comparison purposes, we used the texture features from B-scan windows equivalent to the analyzed RF time series ROI as alternative features for tissue typing. An exhaustive search determined the optimal subset of the 12 features for each of the six different tissue pair classifications. Table 5.7 illustrates the list

Table 5.6: Results of applying the proposed tissue classification approach based on RF time series to the data acquired on a clinical ultrasound machine (probe center frequency: 6.6 MHz). For each tissue pair, the results of the best performing set of features is reported.

Tissue types	Selected features	Classification accuracy (STD)
Bovine liver - chicken breast	S1,S2,S3,S6,FD	97.5% (3.0)
Bovine liver - bovine muscle	S1,S2,S5,FD	98.1% (0.8)
Chicken breast - pig liver	S1,S3,S4,S6,FD	94.6% (3.2)
Pig liver - bovine muscle	S2,S5,S6,FD	94.8% (1.8)
Bovine liver - pig liver	S1, S4,S5,S6,FD	95.4% (2.6)
Chicken breast - bovine muscle	S4,S5,S6,FD	90.6% (0.9)
Average over all six tissue pairs	**95.1%**	

of selected subsets of texture features along with the accuracies acquired for each of the tissue typing experiments. The results show a maximum of 88.1% in bovine liver versus bovine muscle classification, which yielded the maximum accuracy using the RF time series as well. On average, over all six pairs of tissue types, an accuracy of almost 77.5% was acquired. The first order texture features appeared in all of the selected feature vectors (Table 5.7). However, they did not show an acceptable performance without inclusion of the co-occurrence features. In case of all six tissue pairs, the optimal feature subset selected during the exhaustive search consisted of five, six or seven features. The difference between the performance of the texture features and the RF time series features is sizable: 77.5% versus 95.1%.

5.4.2 Results at 55 MHz

At very high frequencies, the scattering of ultrasound is primarily caused by the cellular microstructure [64] as opposed to tissue macrostructure. Therefore, the dependence of the variations in RF time series on cellular microstructure should be more evident in high-frequency data. We used a dataset of RF time series, acquired

Table 5.7: Performance of the twelve texture features in classification of tissue types. For each tissue pair, the results of the best performing set of features is reported.

Tissue types	Selected features	Accuracy (STD)
Bovine liver - chicken breast	Cn90,E90,H90,M,SD,K	74.4% (1.5)
Bovine liver-bovine muscle	Cn0,Cr0,Cr90,M,SD	88.1% (2.5)
Chicken breast - pig liver	Cn0,Cn90,H0,M,Sk	65.7% (1.9)
Pig liver - bovine muscle	Cr0,Cr90,E90,H90,M,SD,Sk	81.7% (1.9)
Bovine liver - pig liver	Cn90,Cr90,E0,H90,M,Sk	70.9% (1.3)
Chicken breast - bovine muscle	Cn0,E0,H90,M,SD,Sk	84.4% (2.2)
Average over all six tissue pairs	**77.5%**	

at 55 MHz from the four tissue types analyzed in this study, to examine the effects of high-frequency ultrasound on the tissue typing capabilities of the proposed features.

We exhaustively searched for the optimal set of features in each of the six tissue typing experiments on high-frequency data. It was noticed that in the high-frequency data, one can accurately identify the tissue types with even one single feature. For example, using only the FD of RF time series, we were able to achieve an average accuracy of just below 90% over six tissue pairs. This accuracy was achieved when FD was calculated with $k_{max} = 16$. Figure 5.10 shows the average classification accuracies acquired when FD with different values of k_{max} were used.

As presented in Table 5.8, the average accuracy increased to 98.1% when we used optimal combinations of features. Compared to the accuracy acquired with the clinical frequency data, the tissue typing with the high frequency machine was significantly more accurate ($p < 0.01$). In some cases, such as bovine liver versus chicken breast, and chicken breast versus pig liver the obtained classification accuracies were practically 100% over almost all 50 rounds of leave-10%-out trials. Table 5.8 provides the selected features and acquired accuracies in our high-frequency tissue

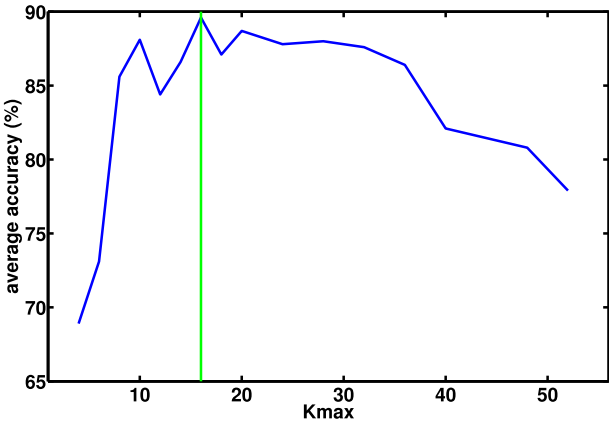

Figure 5.10: The average accuracy of classification over the six pairwise trials *vs.* the k_{max} value used for calculation of FD. Only the FD was used for the classification. This result was acquired using data at 55 MHz.

typing experiments on the six available tissue pairs.

It should be also noted that in the high-frequency data, the difference in classification accuracy between optimal combinations of feature vectors with three, four or five features was very subtle. Also, features that did not show a significant tissue typing value when extracted from low-frequency data, appeared useful in tissue typing at high-frequency. This is noticeable by examining the optimal feature vector found for the last experiment in Table 5.8 where a very high accuracy is obtained without FD or S6 being part of the feature vector. Similarly, for bovine liver versus pig liver, S6 and FD are absent. However, the combination of S1,S2,S3,S4 carries the information about the spectral slope (S6).

The difference between the average accuracy acquired on high-frequency data versus low-frequency data was significant (98% versus 95%, the difference is almost three times larger than the highest standard deviation in Table 5.8). This is even more evident when we consider the performance of FD, the best single tissue typing

Table 5.8: Tissue typing results on data acquired at 55 MHz. For each tissue pair, the results of the best performing set of features is reported. The results were significantly more accurate than the clinical frequency experiments ($p < 0.01$).

Tissue types	Selected features	Classification accuracy (STD)
Bovine liver - chicken breast	S1,S3,FD	99.9% (0.3)
Bovine liver - bovine muscle	S2,S3,S4,FD	97.9% (0.7)
Chicken breast - pig liver	S3,S4,S6,FD	99.4% (0.7)
Pig liver - bovine muscle	S1,S2,S3,S5,S6,FD	97.2% (0.7)
Bovine liver - pig liver	S1,S2,S3,S4	96.4% (0.9)
Chicken breast - bovine muscle	S1,S2,S5	98.0% (0.9)
Average over all six tissue pairs	**98.1%**	

feature, on the two datasets. While on average FD yields an accuracy of 78% when used as the only tissue typing feature for low frequency data, an accuracy of 90% is acquired with FD at 55 MHz.

Validation tests

To ensure that the class separability of the features originated from the tissue microstructure variations (and not from possibly different imaging conditions), we performed classifications in only one tissue type (negative control): we tried to distinguish ROIs from the two different A-lines that were available from two different pieces of the same tissue type using the fractal dimension of high frequency RF time series. These classification experiments resulted in an average accuracy of 53% (std: 4.3%). In other words, the proposed tissue typing parameters only separated data from different tissue types and failed to distinguish data acquired from different areas of the same tissue type. This is another indication of the link between tissue microstructure and variations of RF time series

We also performed a bootstrap test to ensure the validity of the classification

accuracies reported in this section. In this bootstrap test, we randomly mixed the feature vectors belonging to two classes of tissue. In other words, each ROI was given a wrong class label with probability of 0.5. This mixed dataset was used for leave-10%-out classification and validation. This process was repeated 1,000 times, each time with a new random mixture of class labels. Figure 5.11 shows the distribution of the acquired classification accuracies for the case of bovine liver versus chicken breast classification. The distribution is very close to a Gaussian with mean at 50.1% and standard deviation of 3.6%. In other words, when data is blindly combined and mixed, classification outcomes are poor and the very high classification accuracy acquired with the original data is definitely significant and originates from the difference in tissue types.

Four-class classification with high-frequency data

To further validate the tissue typing capability of the proposed features extracted from high-frequency ultrasound, we used the data from all four tissue types for training and the network was tested on all four classes as well. The network architecture consisted of a hidden layer with five neurons, and two neurons in the output layer. We used 75% of the data from each tissue type for training and 25% for testing. The training and testing procedure was performed 100 times with different random selections of train and validation data and the test accuracies were averaged. The average accuracy was 92.6% with a standard deviation of 6.6%.

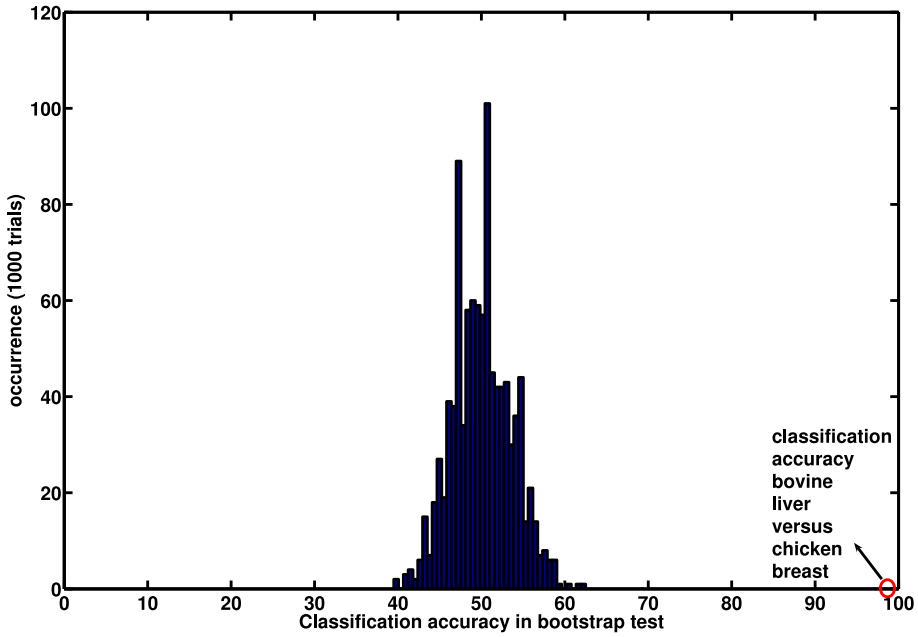

Figure 5.11: Result of the bootstrap test for analysis of validity of the classification results on bovine liver versus chicken breast. The histogram shows the distribution of the classification accuracies when the class labels of the ROIs of the two classes are randomly mixed. The original data yields an average classification accuracy of 99% which is significantly outside the distribution of the randomly mixed data.

5.5 Chapter summary and conclusions

This chapter described two different studies that provided experimental evidence for the utility of the tissue typing method based on the RF time series features proposed in this thesis. First, in a study that involved custom-made agar-gelatin based phantoms, we showed that the proposed RF time series features when used along with SVM or neural network classifiers, can differentiate phantoms with cell mimicking particles of different sizes. Two different types of microscopic glass beads with average diameters of 11 μm and 35 μm were used in these phantoms and we were able to distinguish

them with statistically significant accuracies of up to 80.5%.

Second, we performed an animal study involving four different animal tissue types that extended the proposed methodology to biological tissues. We demonstrated that a set of parameters extracted from RF time series are very efficient for tissue typing. These parameters included six spectral features and the fractal dimension of RF time series. Our exhaustive feature selection study pinpointed four to five of these features as the subset that produced the highest classification accuracy for each of the six tissue pairs. The classification accuracy averaged over all six analyzed tissue pairs was 95.1% for the data acquired at 6.6 MHz. We compared this result with the performance of the texture features extracted from windows of B-scan images equivalent to RF ROIs. The average classification accuracy using the B-scan features was 77.5%, significantly inferior to the results acquired from our proposed features.

In order to ensure that the results are not system specific and also to study the effects of increasing the ultrasound frequency on the outcome of our approach, we studied RF time series acquired on a high-frequency (55 MHz) ultrasound probe from the four animal tissue types. We found that using the high-frequency data, classification accuracies of up to 99.9% are achievable (an average accuracy of 98.1% over all six pairs).

The phantom and animal studies described in this chapter provided sufficient evidence to support the central idea of this research. They justified a large scale investigation involving human prostate tissue to achieve the ultimate goal of this thesis which is improving the diagnosis of prostate cancer. The next chapter will report that study.

Chapter 6

Ex-vivo Human Studies

The primary goal of this research is to enhance the clinical process of diagnosis of prostate cancer through augmenting ultrasound images with cancer probability information. Such information can assist a radiologist during the biopsy process to reduce the risk of false negative outcomes. In previous chapters, we laid the foundations of our proposed methodology for tissue typing based on RF time series, and provided experimental evidence that supported its utility through phantom and animal studies. In this chapter, we will provide the results of applying the methodology on human prostate tissue.

The overall format of the study involved collecting ultrasound RF time series from extracted prostate glands of patients who underwent prostatectomy. Histopathologic analysis of tissue was acquired at the same cross sections that were scanned. The proposed tissue typing features in Chapter 4 were extracted from the ultrasound data. A SVM classifier, trained to classify regions of interest described by tissue typing features in cancerous and normal classes, was used to create the cancer distribution probability maps. The gold standard used to train the classifier, and also to evaluate

its performance, was histopathology reports. The histopathology analysis was acquired after manual registration of ultrasound and images of whole mount pathology slides.

As part of the study reported in this chapter, we examined the effects of tissue depth, ultrasound acoustic power and frame rate on the performance of the methodology. The results of this analysis can be used for optimization of the imaging parameters during biopsy.

6.1 *Ex-vivo* human data

We performed a process of ultrasound and histopathology data collection from patients who chose prostatectomy as their treatment option at Kingston General Hospital during 2007. Data was collected from 35 patients. Patients' consents were acquired to perform ultrasound scanning on extracted prostate specimens prior to their participation in the study. After the surgery, the tissue was fixed in formaldehyde solution overnight, scanned the next day and sent back for histopathology analysis.

Extracted prostate specimens were suspended in a water bath, and were scanned along transverse planes, 4 mm apart (see Figure 6.1). The location of the first cross section was marked, by the pathologist, with two parallel needles, visible in ultrasound image as two lines. To ensure the validity of the manual registration, the needles were needed to mark the first cross section. Consequent cross sections were acquired at 4 mm intervals. The strong echoes from the needles rendered the data from the first cross section practically useless. However, the needles were needed to ensure that the location of the first cross section was preserved during the process. Four to six consequent cross sections of data were acquired from each specimen (depending on

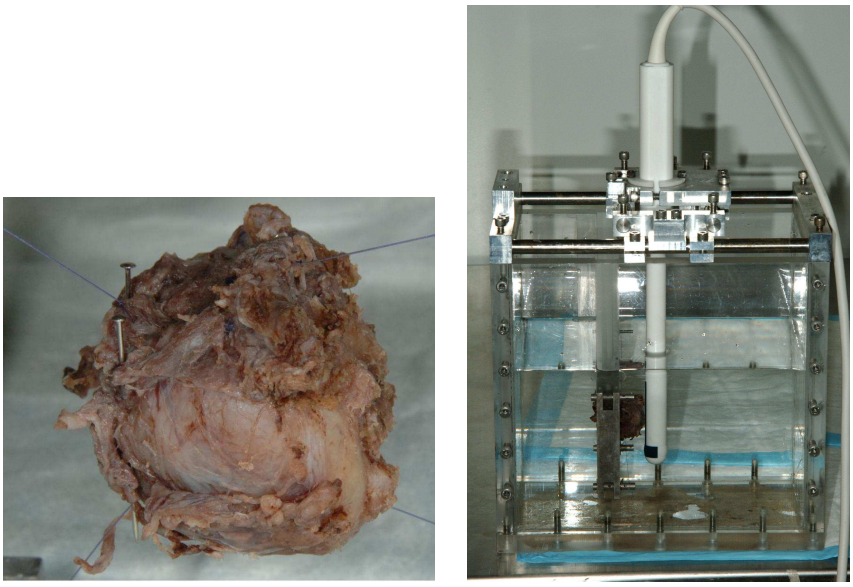

Figure 6.1: Experimental setup. Left: Two needles mark the location for the first cross section. Right: the prostate is suspended in a water bath and scanned at cross sections 4 mm apart.

the size of the specimen). Next, whole mount pathology slides were created from the specimens at approximately the same cross sections scanned, starting from the plane marked by the needles and continuing at parallel cross sections 4 mm apart. The slides were analyzed by a senior pathologist at Kingston General Hospital and cancerous areas were reported. The contours of tumors were directly marked on the slides by a senior pathologist. The slides were then photographed with a digital camera.

The ultrasound RF data was collected using a Sonix RP (Ultrasonix Inc., Richmond, BC, Canada) ultrasound machine. A transrectal probe (BPSL9-5/55/10) was used with the central frequency of 6.6 MHz. To form the RF time series, we acquired

112 frames of RF data, at the rate of 22 frames per second (fps) from each cross section of the tissue. Therefore, the length of RF time series in our human data was 112 for each tissue cross section. The maximum imaging depth was set to 4.5 cm. The sampling frequency of the RF data was 20 MHz. The probe was placed in direct contact with the tissue in water, and only one focal point was set at depth 1.5 cm in all cases. Prior to scanning, we measured the temperature of water to ensure that all tissue specimens were scanned at temperature range of $22 - 24°C$.

During each data collection session, the calibration data for Lizzi-Feleppa method was acquired from the surface of a flat glass plate in a water bath at the transducer focal zone, with minimum amplifier gain and flat TGC.

6.2 Histopathology to ultrasound registration

The process of registering the histopathology maps to the RF frames was performed manually. Due to the non-zero elevation beam width of the ultrasound beams and also inevitable errors caused by the low precision cutting process in the pathology laboratory, the accurate match between tumor boundaries in ultrasound and histopathology images was challenging. As the first step in the manual registration, the cross sections from histopathology and ultrasound were matched based on the order of scans starting at the cross section with the needles. Landmarks such as the urethra or the characteristic irregularities in the boundaries of prostate in both ultrasound and histopathology images were matched to ensure the correspondence of the cross sections (Figure 6.2). In some slides, we were unable to find and match such landmarks. Those slides were not included in the training data. The scale factors in ultrasound images and digital images of the pathology slides were then used to determine the

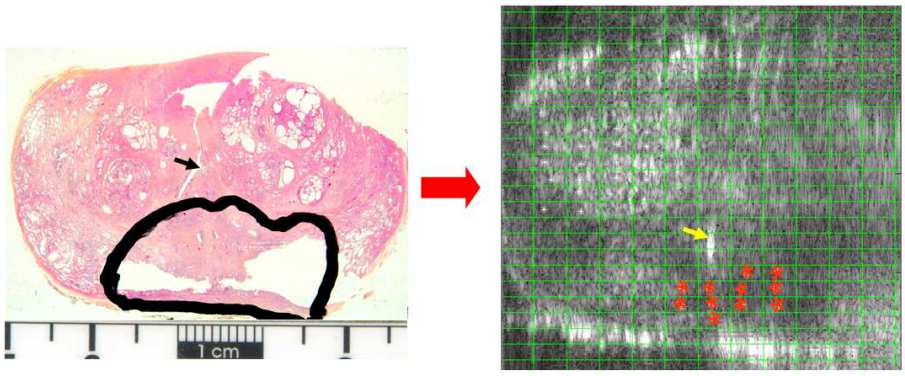

Figure 6.2: The histopathology results were reported as contours of tumors directly depicted on the whole-mount slides. These contours were used to manually mark the cancerous areas on the ultrasound images. Landmarks such as the urethra were used to determine the location of tumors in the ultrasound image (white arrow in both images above). ROIs were selected from areas residing in the center of the cancer contours.

approximate location of tumor in the ultrasound image. Since the determination of the exact boundaries of the tumors on ultrasound was subject to registration error, in selection of the cancerous areas we only chose the ROIs that resided within the central zones of the tumors and avoided using ROIs that were closer to the approximate boundaries. As a result, many of the slides with very small tumors could not be used for selection of the cancerous areas for the training set. The normal ROIs used for training were chosen from the areas of the peripheral zones of the specimens that were safely far from any marked malignancy.

This process amounted to 1824 normal and 1025 cancerous ROIs of size 1 $mm \times 3.5\ mm$ selected from 55 cross sections. This ROI size included segments of four RF A-lines, each of length 96 samples[1]. This specific choice of width was due to the fact

[1]During the manual selection process, the selected ROIs were of size 2 $mm \times 3.5\ mm$ (eight line segments of length 96 in RF space). These ROIs were each divided in two halves. The resulting ROIs of size 1 $mm \times 3.5\ mm$ were used as independent ROIs.

that the width of the tissue cores acquired in clinical biopsies is approximately 1 mm. The choice of the length was based on a compromise. Long ROI sizes would have further constrained using smaller tumors in the study. The length of 3.5 mm was chosen since it enabled us to select ROIs within tumors as small as 5 mm. Shorter ROIs, on the other hand, could limit the accuracy of the spectral frequency calculated for the extraction of Lizzi-Feleppa features from segments of RF scan lines in the ROI.

6.3 Features and classification

All three categories of features including RF time series features, Lizzi-Feleppa (LF) features and B-scan texture features described in Section 4.1 were extracted from the tissue ROIs. We separately performed an exhaustive search process to find the best subset of texture, LF and time series features that maximized the tissue typing accuracy for cancer detection. These three best subsets were combined and subjected to an additional exhaustive search. The outcome was the feature vector used to generate the cancer distribution probability maps. This two stage method of feature selection (aimed at optimizing both the dimension of the feature vector and the choice of features) was not guaranteed to provide the highest possible accuracy. An exhaustive search over all 22 features combined could have resulted in a better performing subset. However, it required examining $\sum_{n=0}^{22} C_n^{22} = 2^{22}$ subsets which was computationally infeasible. Feature space reduction based on Principal Component Analysis (PCA) was an alternative solution. We chose the two-stage method because it also enabled us to compare the performance of the three approaches for tissue typing. However, we also examined the PCA-generated feature vector. The performance of the best PCA-based feature vector was compared with the feature vector selected through the

exhaustive search (Section 6.5.2).

For reasons that were detailed in Section 4.3.5, we used the SVM classification approach for our human study. The entire dataset was normalized prior to training by setting the maximum value of each feature to 1 and the minimum to 0. For parameter selection (C and γ), we exhaustively searched the parameter space $\{C \in \{2^{-10}, 2^{-9}, ..., 2^{10}\}, \gamma \in \{2^{-10}, 2^{-9}, ..., 2^{10}\}\}$ followed by a search on $\{1 \leq C \leq 100, 1 \leq \gamma \leq 100\}$ with steps of length 1. This two step search is frequently used in studies involving SVM [47]. For each set of parameters, 10-fold cross-validation was performed: we trained the SVM using 90% of the available ROIs, classified the remaining 10%, and repeated the procedure for all 10 portions of the data. The computational expense of this exhaustive search was feasible on our parallel computing server (Sun Microsystems, Sun Fire V890, equipped with eight dual core processors running at 2.1 GHz frequency).

6.4 Cancer distribution probability maps

Cancer distribution probability maps were generated based on the outcome of the SVM classification. For generation of each map, the SVM classifier was trained on all the training data expect for the ROIs originating from the patient under study. Then, the proposed tissue typing features were extracted from data acquired from a cross section of interest in the patient under study. ROIs of size 1 $mm \times 3.5$ mm were classified and the posterior probability of cancer P_c was computed for each ROI using the method described in Section 4.3.3. For generation of the cancer distribution probability maps, we chose the threshold of $P_c > 0.4$ to color an ROI on the map. The color theme was yellow to red (where red stands for the highest probability of cancer).

The choice of the threshold was rather subjective. However, we found that with the threshold of $P_c > 0.4$, the visualized maps demonstrated all the major tumors in the dataset without a significant number of false positive detections.

It should be noted that the cancer distribution probability maps were acquired by tissue typing of the entire peripheral zone of the prostate. In other words, the test data used for each map was not limited to the ROIs that were manually registered and used for feature selection and training. The quantitative evaluation of the accuracy of the cancer distribution probability maps was, however, performed only on the ROIs for which a definitive label was available.

6.5 Results

6.5.1 Performance of different groups of features

The exhaustive search for the best subset within each of the three categories of features resulted in a two-dimensional feature vector among texture features (Mean and correlation at 0°), a two-dimensional feature vector among Lizzi-Feleppa features (LF1,LF3), and a six-dimensional feature vector (S2,S3,S4,S5,S6,FD) among the proposed time series features. As Table 6.1 demonstrates, while LF features show a superior performance in cancer diagnosis compared to texture features, time series features outperform both of them. The area under the ROC curve acquired was 0.87 for RF time series features, 0.78 for Lizzi-Feleppa features and 0.72 for the texture features.

Table 6.1: Comparison of the performance of texture, Lizzi-Feleppa, and RF time series features in classification of cancerous *vs.* normal human prostate tissue with 10-fold cross-validation. The numbers in parentheses are the standard deviations.

Feature Group	Area under ROC ROI size: 1 $mm \times 3.5$ mm (std)
Best subset of Texture features (Mean and correlation at 0°)	0.72 (0.008)
Best subset of Lizzi-Feleppa features (LF1,LF3)	0.78 (0.005)
Best subset of Time series features (S2,S3,S4,S5,S6,FD)	0.87 (0.006)
Best subset of the combination of the three groups above: (Mean,S2,S4,S6,FD,LF1,LF3)	**0.95 (0.004)**

6.5.2 Optimal combined feature vector

To acquire the best combination of features for the cancer distribution probability maps, we combined the selected features from the three groups into a ten-dimensional feature vector and performed the exhaustive search on them. As Figure 6.3 demonstrates, we found specific subsets with seven, eight and nine features equally and highly accurate in classification of ROIs. It was noticed that these specific subsets (which are detailed on Figure 6.3) provide the highest sensitivity and accuracy compared to the other subsets of their size. The seven-dimensional subset (Mean, S2,S4,S6,FD,LF1,LF3) was selected due to its smaller size. As the last row of Table 6.1 reports, an area under ROC curve of 0.95 was achieved on ten-fold validation using this seven-dimensional feature vector. The ROC curves acquired using different

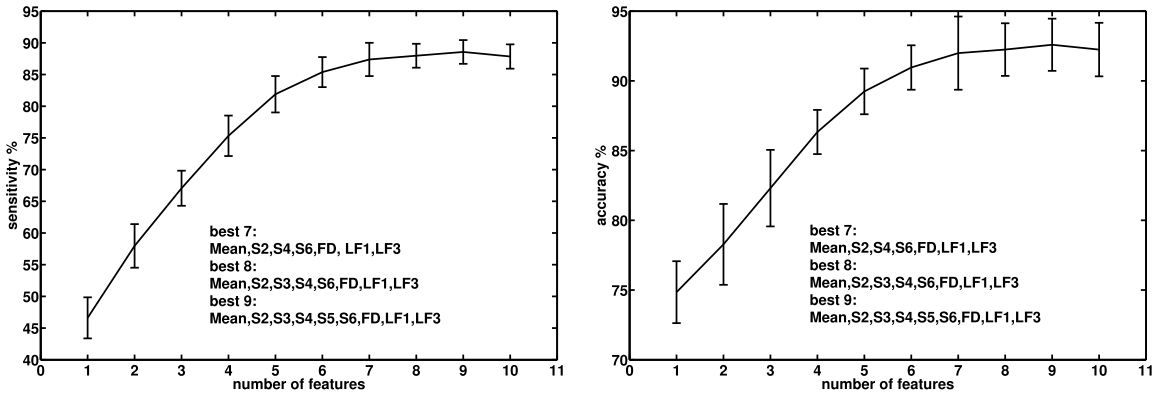

Figure 6.3: The combination of optimal subsets of features in the three tissue typing approaches resulted in ten features. The outcome of the exhaustive search on all possible subsets of these 10 features is depicted here. The subsets listed on the diagrams maximized the sensitivity and the accuracy in their respective sizes.

tissue typing methodologies are illustrated in Figures 6.4,6.5,6.6 and 6.7.

As discussed in Section 6.3, we also examined the PCA-based method for feature vector reduction. PCA is an orthogonal projection of feature vectors onto a lower dimensional space defined by the eigenvectors of the data covariance matrix. The new features are a linear combination of the old features. In the resulting feature vectors in the new space, the features are sorted in order of their contribution to the variance in the data. Therefore, in order to go from N features to M, where $M < N$, one needs to apply the PCA transform and use the first M features, with the largest contribution to the variance, in the new space as the reduced feature vector. We applied PCA to the 22-dimensional data space in our study. We tried inclusion of up to 10 components of PCA; it was noted that inclusion of more than 10 components of PCA did not result in a substantial improvement in the classification results. The area under ROC curve, acquired with a 10-dimensional feature vector, corresponding

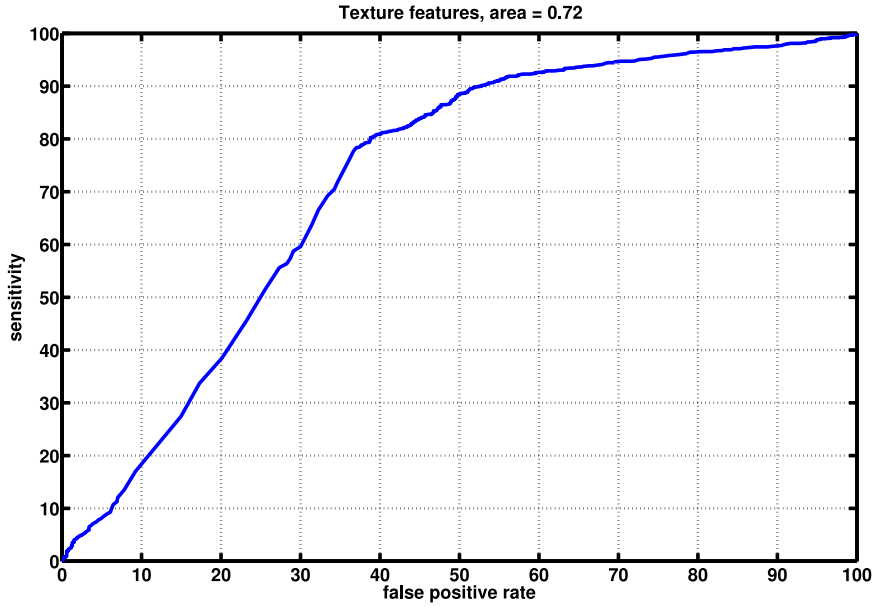

Figure 6.4: ROC curve resulting from 10-fold cross-validation with the selection of texture features. Note that at the sensitivity of 90%, the specificity was 45%.

to the first 10 principal components of the data was $0.91 \pm 0.003\%$ in 10 fold cross validation. This was slightly less accurate than the performance of the the feature vector resulting from exhaustive search in detection of cancer.

6.5.3 Cancer distribution probability maps

The cancer distribution probability maps were created by tissue typing of the entire peripheral zone of the prostate. In other words, the test data used for each colormap was not limited to the ROIs that were manually registered and used for feature selection and training. Figure 6.8 demonstrates some of the cancer distribution probability maps acquired using the described best seven-dimensional (Mean, S2,S4,S6,FD,LF1,LF3) feature vector and the coloring threshold of $P_c > 0.4$. The

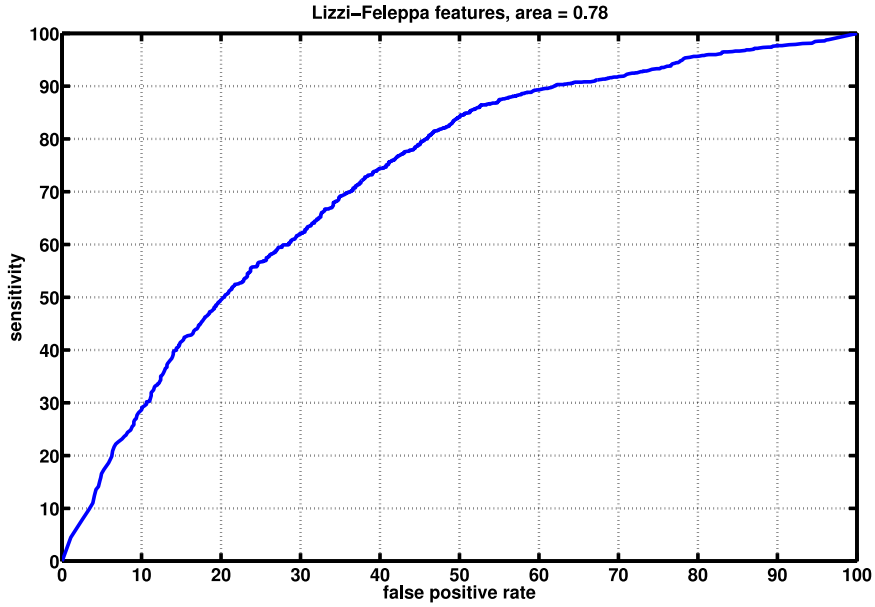

Figure 6.5: ROC curve resulting from 10-fold cross-validation with the selection of Lizzi-Feleppa features. Note that at the sensitivity of 90%, the specificity was 40%.

color theme was yellow to red (where red stood for the highest probability of cancer).

It should be noted that due to uncertainties in the registration, caused by the inevitable errors in the spatial measurements during the cutting process in pathology, by ultrasound beam thickness, and by elastic deformations of the tissue, the boundaries of the tumors in ultrasound and pathology images in Figure 6.8 are not expected to match precisely. Also, the rectangular shape of the ROIs limits the geometrical flexibility of the boundaries of tumors depicted in the colormaps.

6.5.4 Quantitative patient-based validations

When assessing the accuracy of a tissue typing approach, it is important that the test subsets be drawn from patients completely absent in the training data [101].

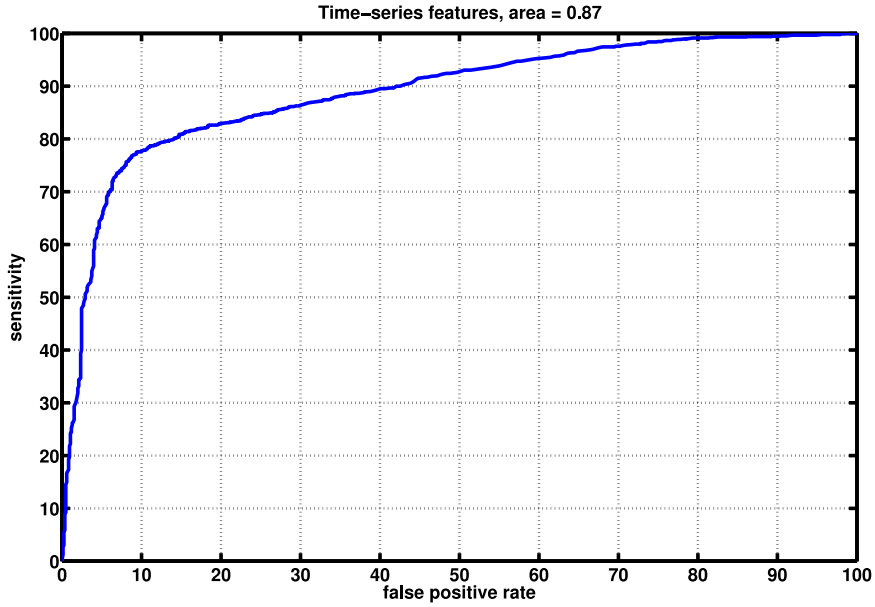

Figure 6.6: ROC curve resulting from 10-fold cross-validation with the selection of time series features. Note that at the sensitivity of 90%, the specificity was 60%.

Therefore, to gain a more realistic measure of the performance, we performed patient-based cross validation. The test data for this cross validation consisted only of the ROIs manually registered from ultrasound to histopathology (1824 normal and 1025 cancerous ROIs from 55 cross sections within the data). The test was performed in leave-one-patient-out manner. For each patient, we trained the SVM based on ROIs from all other patients and tested it on ROIs from the patient in question. With repeating this process for all the patients in the dataset, all the ROIs were included in the tests. The area under ROC curve for this patient-based validation was 0.82 with a standard deviation of $\pm 7\%$ over the patients in the dataset.

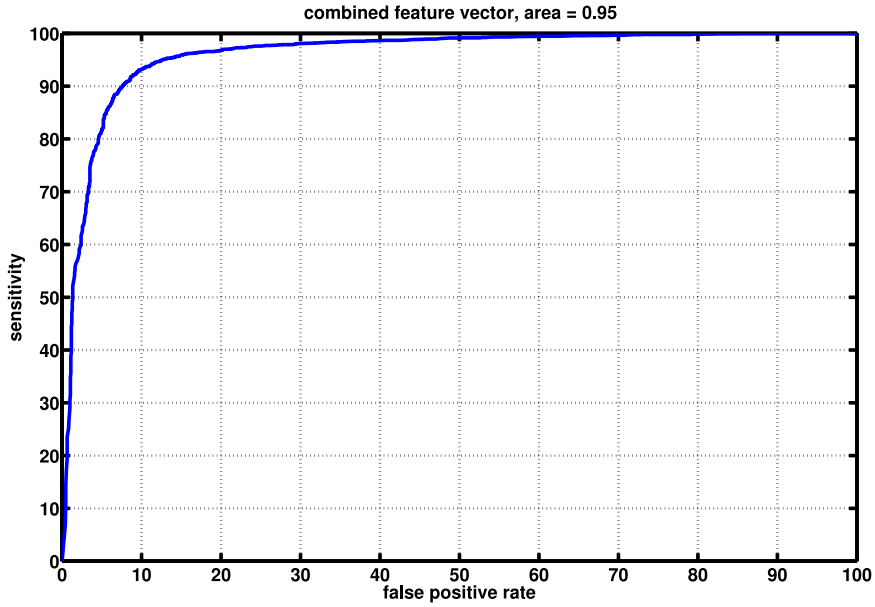

Figure 6.7: ROC curve resulting from 10-fold cross-validation with the combination of texture, LF, and time series features. Note that at the sensitivity of 90%, the specificity was over 90%.

6.6 Effects of imaging parameters on tissue typing accuracy

The results described in the previous section show that the RF time series features are powerful tissue typing parameters. While the LF and texture parameters have long been studied for their statistical distribution and physical interpretations [85, 129], time series features are new and hardly explored. In this section, we report the results of our analysis on some of the parameters that can potentially have an effect on the tissue typing capabilities of the RF time series.

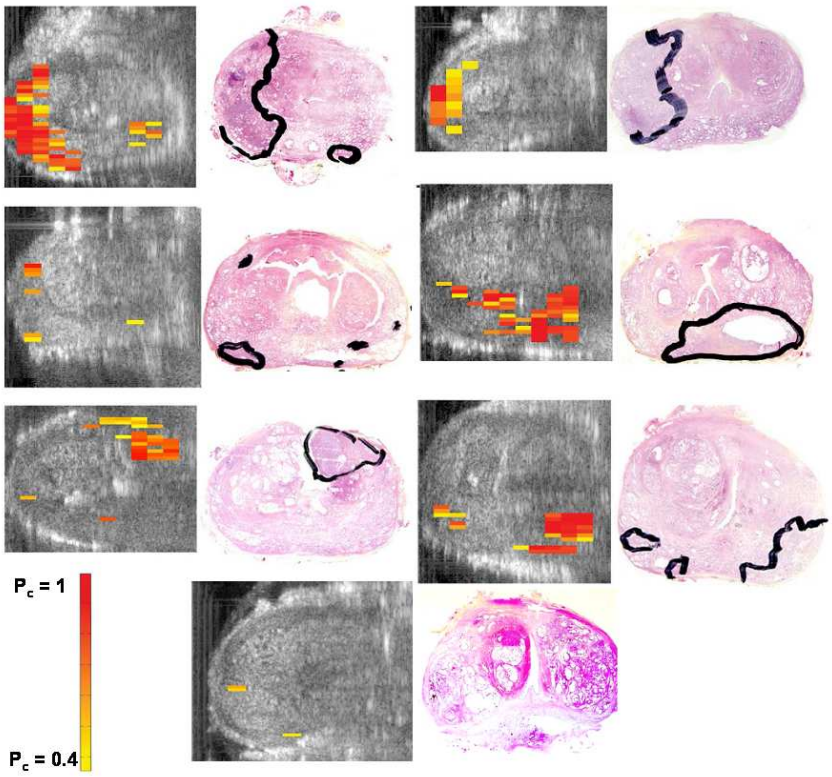

Figure 6.8: Cancer probability maps along with the closest matching histopathology slides for seven patients. The ultrasound probe is in touch with the left side of the gland in all cases.

6.6.1 The effect of ROI size

The resolution of the probabilistic cancer maps is determined by the size of ROI. One advantage of the RF time series features is that theoretically, the ROI size can be decreased arbitrarily. Clearly, at very small ROI sizes, the noise plays an increasingly important role and the accuracy is expected to drop. On the other hand, very large ROIs are bound to be inhomogeneous and affect the classification outcome. Our analysis confirmed this intuition. We performed 10-fold cross-validation experiments

with only RF time series features acquired from various ROI sizes. We studied ROIs which included segments of 1, 2, 4, and 8 RF A-lines. The most accurate classification result was acquired when ROIs consisting of only one RF A-line of length 96 were classified (area under ROC curve of 0.88 ± 0.002 for an ROI size of $0.25\ mm \times 3.5\ mm$ corresponding to 1×96 RF samples). This was only slightly more accurate than the performance of the classification acquired on ROIs of size $1\ mm \times 3.5\ mm$ primarily used in this research (0.87). The choice of the ROIs of width 1 mm can also be justified based on its similarity to the width of biospy cores. The lowest accuracy was acquired on the largest studied ROI size which included segments of 8 RF A-lines, each of length 96 and provided an area under ROC of 0.837 ± 0.01.

6.6.2 The effect of tissue depth

For ROIs of length $1\ mm \times 1.8\ mm$ or 48 samples long[2], and the imaging depth of $4.5\ cm$, we had ROIs at 24 discrete depth levels in the dataset. We performed a leave-one-patient-out SVM classification and validation using all the manually registered ROIs, and measured the accuracy at each depth. Our analysis showed that tissue typing based on RF time series features is more accurate in areas that are closer to the ultrasound probe. As the diagram in Figure 6.9 demonstrates, we witnessed a meaningful drop in the accuracy of our prostate tissue typing experiments (based on only the RF time series features) for ROIs that are more than 3 cm away from the probe. With the only transmit focal point set at 2 cm (in the prostate data), the ultrasound beams diverge increasingly at deeper areas of the tissue. Furthermore, the effects of amplifier noise are more prevalent in deeper areas. Therefore, data from the

[2]These ROIs were generated by vertically dividing the original ROIs of length $1\ mm \times 3.5\ mm$ in two equal halves.

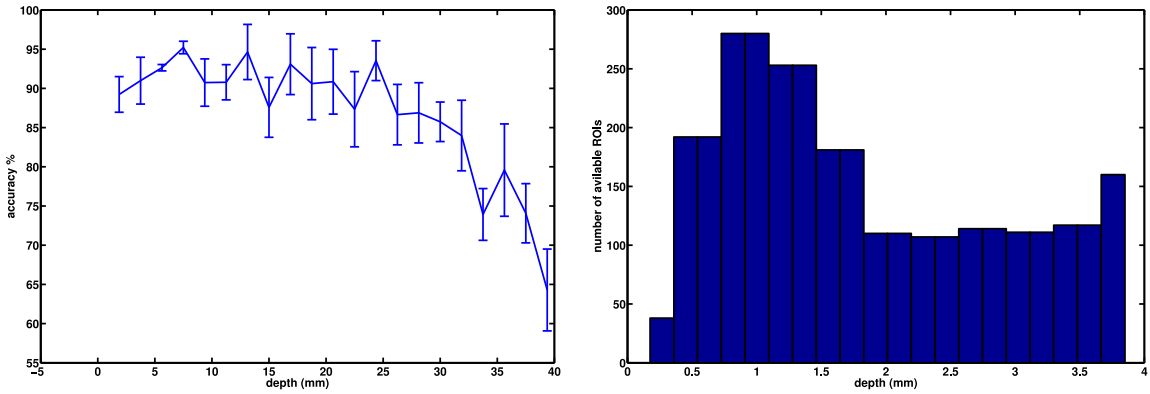

Figure 6.9: Left: the accuracy of tissue typing *vs.* the depth of the ROI. It is clear that the accuracy drops substantially with increasing depth of the tissue. Right: the histogram showing the number of ROIs in different depths.

deeper areas have higher levels of noise (noise is measured as $\sum_{i=1}^{i=112}(x_i - \overline{x})^2$ where $\overline{x}$ is the mean of the RF time series and x_i's are the samples of the RF time series; the length of the time series is 112). The tissue typing information is carried in time series variations, and the increasing levels of destructive noise in deeper areas of the tissue decreases the signal-to-noise ratio (SNR) in the received RF time series. From the clinical point of view, the depth-dependent accuracy of the approach does not pose a significant challenge. The reason is that the most cancer-prone area of the prostate gland is the peripheral zone which is also the target of inspection during biopsy. According to [114], up to 80% of cancer findings in prostate occur in the peripheral zone. The ultrasound probe is in touch with the peripheral zone of prostate during the biopsy process.

6.6.3 The effect of ultrasound power

A reduction in the acoustic output power of the ultrasound probe also reduces the signal-to-noise ratio in the RF time series. The ultrasound machine is normally operated at its highest acoustic power level to maximize the contrast and signal-to-noise ratio (all the results reported in previous sections were acquired at this level). To study the effects of ultrasound acoustic power applied, we repeated the 10-fold cross-validation experiment, based on only RF time series features, at two additional power settings. We found that a 2 dB reduction in the output power resulted in a drop of area under ROC curve from 0.87 ± 0.006 (Table 6.1) to 0.84 ± 0.009. A 6 dB reduction in the acoustic power output resulted in a more significant drop of the outcome to 0.76 ± 0.009. Figure 6.10 demonstrates a visual comparison of the noise levels at the three studied power settings (data acquired by mounting the probe in a large water container with no tissue involved). It is also notable that the noise level increases at deeper areas in all three settings.

According to these results, the tissue-dependent information has a direct relationship with the amount of energy applied to the tissue. This supports the explanation provided in Chapter 3 which suggested that the tissue typing information in RF time series originates from microstructural vibrations in biological tissue caused by the acoustic force from ultrasound beams. Obviously, this mechanism fades at lower levels of energy. Therefore, it is expected to witness a decay in the tissue typing information in the RF echoes originating from deeper regions of the tissue or lower levels of acoustic power. Our observations confirm this decay.

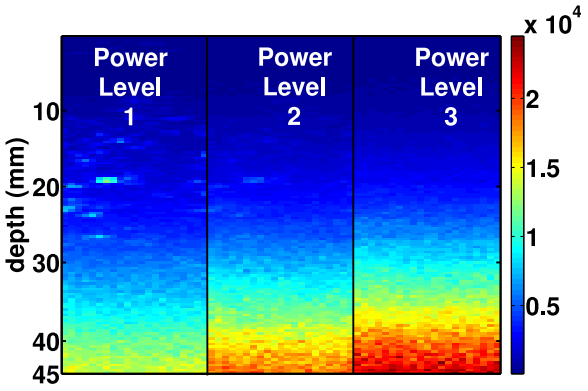

Figure 6.10: The noise level at different depths for three different decreasing transducer acoustic power settings (0 dB, -2 dB and -6 dB). The data was acquired by mounting the probe in a large water container with no tissue involved. The noise level is calculated based on the method described in Section 6.6.2 and mapped onto the ultrasound image. Noise amplitude increases at deeper areas and in lower power levels. The increased level of noise decreases the SNR in the backscattered echoes and reduces the accuracy.

6.6.4 The effect of frame rate

RF time series are generated by continuous scattering of ultrasound beams from tissue structures. The frame rate of the ultrasound machine determines the frequency at which this interaction occurs. Therefore, it is important to determine if our frame rate of 22 fps is sufficient for observing this interaction. To answer this question, we examined the tissue typing capabilities of our features acquired at the frame rate of 45 fps. No substantial change was observed in the results. This outcome indicates that the acquisition rate of 22 fps (which is a typical clinical frame rate) is sufficient for the analysis of RF time series to detect prostate cancer.

In case of phantom experiments (Section 5.2), it appeared that increasing the frame rate slightly improved the accuracy of the classification. The inter-phantom

classification experiments on particle size phantoms with features extracted from RF time series acquired at 15 fps, 22 fps and 45 fps resulted in accuracies of 74.2±4.5%, 79±3.1%, and 82.2±3.2%, respectively.

6.7 The histologic variations of prostate tissue

One of the most resource-intensive steps during this study was the histopathologic analysis of whole mount slides and marking the cancerous areas by an expert pathologist. The result of such analysis was provided in form of tumor contours marked on the slides. This level of analysis did not consider the vast variety of tissue types, such as benign malformations, that exist in tissue and can cause non-cancerous deviations from the normal microstructure[3]. This could affect the accuracy of the gold standard used for the study and eventually the final outcomes. This issue might have contributed to the false positive or false negative errors in some cases.

Specifically, any type of tissue that was not characterized as cancerous, was considered "normal" in our analysis. This could have increased the false positive rates in our results. To gain an insight to the effects of this limitation in our gold standard on the specificity of our results, we chose five slides in which our ultrasound-based analysis had resulted in false positive tumor detections. We acquired a more detailed histopathologic analysis on these slides. In two cases, our pathologist reported findings of prostatic intraepithelial neoplasia (PIN) in areas that matched with our false positive detections (Figure 6.11). PIN is an abnormal proliferation of cells that has been widely observed along with carcinoma of prostate. PIN findings demonstrate an

[3]A comprehensive list of such abnormalities and the histopathologic appearance of the tissue undergoing such conditions is outside the scope of this thesis. See [114] as a preliminary reference and [239] as a more comprehensive reference

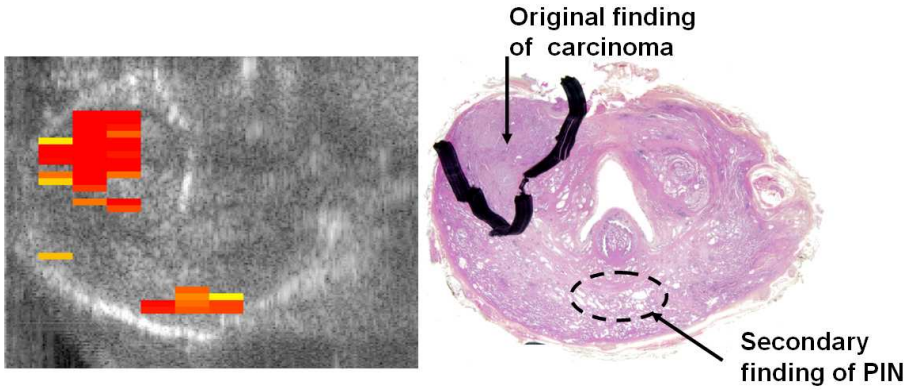

Figure 6.11: One of the false positive detections caused by the existence of prostatic intraepithelial neoplasia. The ultrasound-based method correctly found a tumor in the left anterior side of this specimen and also resulted in the detection of a tumor in the posterior of the gland which did not exist in the original histopathology report. Further histopathology analysis showed a combination of low and high grade PIN in the area that matched the false positive ultrasound-based finding.

entirely different microstructure from normal prostate cells. However, they are not classified as cancerous tissue. Therefore, isolated cases of PIN that did not accompany cancerous tumors were not originally marked by our pathologist. In two other cases, cystic tissue malformations were witnessed. No unusual finding was reported in the fifth slide.

One common histopathologic finding in prostate malignancies is that the small cancerous glands infiltrate the adjacent normal glands [114]. In other words, it is highly unlikely to find an area within prostate tissue that entirely consists of cancerous glands. The true ratio of cancerous glands to the normal glands in areas marked as cancer in our dataset was not determined. A closer analysis of four tumors in our slides showed that in some cases, this ratio was as low as 20% in specific areas of

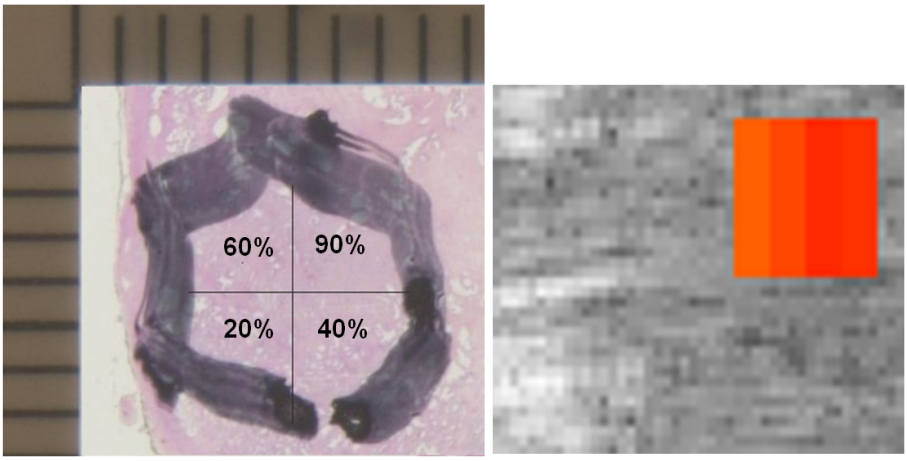

Figure 6.12: A case of low percentage of carcinoma in an area marked as cancer in histopathology slides. In this case, the ultrasound-detected tumor was significantly smaller than the tumor as marked by the expert on histopathology slide. In a detailed secondary analysis of the tumor, we divided it to four parts and asked the pathologist to determine the approximate percentage of cancerous glands in each quarter. This percentage was widely different in the four parts (the numbers are presented on the figure). It was noted that the ultrasound-based method was only sensitive in the upper right side of the tumor which had a higher percentage of cancerous glands.

tumors. An example is depicted in Figure 6.12. In this specific case, the ultrasound-based method showed a high sensitivity in the upper right side of the tumor where 90% of glands were cancerous. The size of the detected tumor in the ultrasound data was smaller than the tumor marked on the histopathology slide. It appears that in this case, and likely other cases with low percentage of cancerous glands, the limited information available in the gold standard histopathology dataset resulted in a limited sensitivity. Due to the limited accuracy of registration, it was not possible to quantify the effects of this limitation on the results.

6.8 Chapter summary and conclusions

This chapter presented the details of our *Ex-vivo* human study involving 35 patients undergoing prostatectomy. We described our ultrasound-based diagnostic approach based on the novel concept of ultrasound RF time series. We described a comprehensive methodology to acquire probabilistic cancer maps of prostate tissue from ultrasound RF time series. We found the features extracted from RF time series more accurate and sensitive than Lizzi-Feleppa features [55, 130] and B-scan texture features. Nevertheless, the latter groups of features complemented the RF time series features resulting in a very effective feature vector that provides an area under ROC curve of 0.95 in 10-fold cross-validation and 0.82 in leave-one-patient-out cross validation. Based on this hybrid feature vector, and an extension to the SVM classification approach [166], we created colormaps that accurately highlighted areas of tissue with high risk of cancer on ultrasound images.

We analyzed the effects of depth of tissue and acoustic power of the ultrasound on the diagnostic outcomes. This analysis showed that reduced acoustic energy levels applied to tissue at deeper areas or at lower ultrasound output power levels, reduce the tissue typing capabilities of RF time series features. An increase in the ultrasound frame rate from 22 fps to 45 fps did not create a substantial change in the outcomes suggesting that the typical clinical frame rate of 22 fps is sufficient for acquisition of RF time series for tissue typing.

An important issue affecting the outcomes of this study was the vast variety of microstructures observed within the two general categories of cancerous and non-cancerous tissue types. PIN (prostatic intraepithelial neoplasia) and BPH (benign

prostatic hyperplasia) are only two of the possible benign variations. Within the cancerous tumors, the cancerous and normal glands are present along with each other and the percentage of cancerous glands is widely different in tumors of different patients or even within different parts of one tumor. These realities suggest that the cellular microstructure of cancerous and normal tissues is a fuzzy concept. The histopathologic analysis used as the gold standard in our study did not take this fuzziness into account. We illustrated examples of limited sensitivity and specificity in our ultrasound-based diagnostic outcomes that are likely caused by this limitation.

The results of the proposed approach in detection of prostate cancer described in this chapter are promising. Furthermore, the RF time series approach has some advantages over the available ultrasound-based tissue typing methods. For example, since all samples of one RF time series originate from the same depth of the tissue, the need for compensation of signals for depth-dependent effects is eliminated. This is an advantage of our methodology compared to the conventional techniques, such as the Lizzi-Feleppa method, that extract features from a segment of one RF A-line. Also, our approach imposes very little overhead to the conventional ultrasound imaging. Unlike elastography, the proposed methodology does not require the compression and mechanical excitation of the tissue.

Chapter 7

Summary and Conclusions

7.1 Summary

This thesis introduced a new paradigm in ultrasound-based tissue typing. The objective of this research was to improve the clinical practice of biopsy for detection of prostate cancer. Studies show a 40-50% rate of repeated biopsies among patients with a negative outcome on the first trial [42, 154]. Therefore, there is a pressing need for the enhancement of the biopsy practice.

We reviewed the state of the art in computer-based methods for diagnosis of prostate cancer and concluded that a comprehensive solution for the low sensitivity and specificity of imaging methods for this application is still outstanding. Ultrasound-based methods for prostate cancer diagnosis are more desirable due to advantages such as non-ionizing nature of the beams, real-time and low cost procedure of ultrasound imaging, and the acceptance of ultrasound as the standard of care in the field.

Therefore, we focused on ultrasound and devised a novel tissue typing approach to augment the ultrasound images of prostate with cancer distribution information

and to enhance the biopsy process. The summary of the contributions are as follows:

- We introduced the concept of the ultrasound RF time series and provided analytical methods to extract efficient tissue typing parameters from RF time series. The core of the idea was that if a location in tissue undergoes sequential interactions with ultrasound, the time series of echoes from that location would carry "tissue typing" information. We introduced six tissue typing parameters extracted from frequency spectrum of ultrasound RF time series for tissue typing. We also showed that fractal dimension of RF time series can be used for tissue typing.

- We argued, based on the evidence available from the literature, that the long term average of the acoustic force applied by ultrasound beams to tissue is not zero but rather depends on the tissue type. Based on this finding we provided a possible explanation for the existence of tissue-type related information in ultrasound RF time series. We described simulation studies that confirmed the existence of information-rich variations in ultrasound RF echoes acquired from a specific location in a scattering media subject to ultrasound emissions. Nevertheless, our case for the feasibility of the proposed tissue typing method for detection of prostate cancer is primarily based on experimental studies.

- We showed that RF time series acquired from agar-gelatin based tissue mimicking phantoms, with difference only in the size of cell-mimicking microscopic glass beads, are distinguishable with statistically reliable accuracies up to 80.5%. This finding suggests that the differences in tissue microstructures affect the ultrasound RF time series features.

- We described animal tissue typing experiments. These experiments were performed using both a clinical ultrasound machine and a high-frequency machine. With nearly perfect classification results acquired on tissue ROIs as small as 20 microns scanned at 55 MHz, the outcome of our proposed tissue typing approach is comparable to the ultrasound biomicroscopy techniques [64].

- We reported an *ex-vivo* clinical study involving 35 patients in which the utility of RF time series features for detection of prostate tumors was confirmed. The outcomes were validated based on detailed histopathologic maps acquired from studied specimens. When a combination of RF time series features, B-scan texture features and Lizzi-Feleppa features were used, a feature vector for cancer detection was obtained that provided an area under ROC curve of 0.95 in 10-fold cross-validation and 0.82 in leave-one-patient-out cross validation. We created cancer distribution probability maps that highlighted areas of tissue with high risk of cancer on ultrasound images.

- We showed that reduced acoustic energy applied to tissue during scanning results in a statistically significant drop in the accuracy of the proposed tissue typing method: a finding that supports our hypothesis about the role of the radiation force of ultrasound in generation of tissue micro-vibrations during acquisition of RF time series.

7.2 Limitations

Although the results reported in this thesis are very promising, the proposed methodology suffers from some limitations which will pose challenges to the process of clinical

utilization. In order to acquire the RF time series, the radiologist needs to collect six to seven seconds of data. During this time, the radiologist's hands should not move or the probe should be fixed in position.

Even with a perfectly fixed ultrasound probe, the *in-vivo* imaging conditions are different from our experiments with extracted prostate specimens. In the live conditions, there are physiological movements at the microscopic level and also on the macroscopic level. On the microscopic level, as discussed in Chapter 3, the spontaneous cell movements and capillary level blood circulation depend on the tissue type and function. Therefore, we can assume that they will add to the information content of the RF time series. However, the macroscopic physiological motion, caused by breathing of the patient and arterial pulsations can significantly affect the process of RF time series acquisition.

Another practical consideration with the proposed tissue typing method is the computational complexity of the calculation of RF time series features. The analysis of RF time series is computationally more costly compared to the analysis of only one RF or B-scan frame. However, our implementations show that the feature values can be extracted from a 1 cm^2 area of the tissue in around one second on a single-CPU (P4, 3 GHz) computer. Therefore, the radiologist can choose a reasonably large area of the image and acquire the cancer distribution probability maps in a very short time during biopsy. Furthermore, parallel processing can increase the speed. We do not believe that computational cost is a major obstacle for development of a clinical biopsy assisting system based on the RF time series method.

A methodological limitation of the proposed technique is its dependence on supervised training of SVM or neural network classifiers. In order to acquire a generalizable

classifier, a large training dataset obtained *in-vivo* will be needed. Given the vast variety of possible pathological (benign or malignant) findings in the human prostate tissue, this training process can be prone to the type of deficiencies discussed in Section 6.7 which reduce the sensitivity and specificity of the diagnostic outcomes. It should be noted that the inhomogeneous nature of biological tissue is a challenge for all tissue typing methods.

7.3 Future Work

We are planning *in-vivo* studies that will determine the effectiveness of our proposed method in clinical practice. Data will be collected from patients during biopsy. The results will be validated based on the histopathological analysis of the biopsy cores. As discussed in the previous section, a probe fixation mechanism is a requirement for the success of the method.

One of our objectives during the *in-vivo* study is to examine the effects of spontaneous physiological motions and specifically, the effects of perfusion and blood circulation on RF time series. Based on the outcome of these studies, we will consider the possibility of combining the RF time series method with Doppler imaging which has shown some potential for diagnosis of prostate cancer (See Section 2.3).

An important improvement to this system can be achieved through consideration of the intrinsic fuzziness of the definition of "normal" and "cancer" in histopathological analysis of tissue types. A rule-based system can be designed in which the ROIs are classified using fuzzy logic principles. The design of this rule-based system will be a challenging task. This is because the stage of malignancy is not only a function of the percentage of cancerous glands in an area of the tissue, but also a function

of microstructural arrangement of the glands, the degree of glandular differentiation, the architecture of the neoplastic glands, and the enlargement of the nuclei. These features are used to define the grade of a tumor using the Gleason grading system [114]. On the other hand, benign malformations such as PIN or BPH are defined based on the features that are not similar to those of normal or cancerous tissue. A comprehensive tissue typing system should assign these malformations to separate classes.

The cancer distribution probability maps presented in this thesis have not been subject to any morphological manipulations. A system designed for clinical applications could benefit from inclusion of morphological operations such as closing of possible holes within colored areas or removal of isolated colored ROIs. Furthermore, the rectangular shape of ROIs defined in our method limits the flexibility of the algorithm in finding the accurate contour of the tumor. The implementation of the method can be enhanced by removal of this limitation and by defining ROIs of arbitrary shape.

In order to facilitate the clinical application of the proposed techniques, currently a software system is being developed to implement a client-server connection to the SonixRP (Ultrasonix, Richmond, BC) ultrasound machine and to collect the RF time series. The GUI of the software will provide a real-time B-scan image and a quasi-real-time view of the probability of malignancy in the tissue. The system will feature libraries of classifiers and feature extraction techniques and will be trained based on the data acquired from a large number of prostate cancer patients undergoing the biopsy procedure. At the current stage, the GUI is designed using Qt (Trolltech, Oslo, Norway), developed with Visual C++ in Microsoft Studio .Net environment.

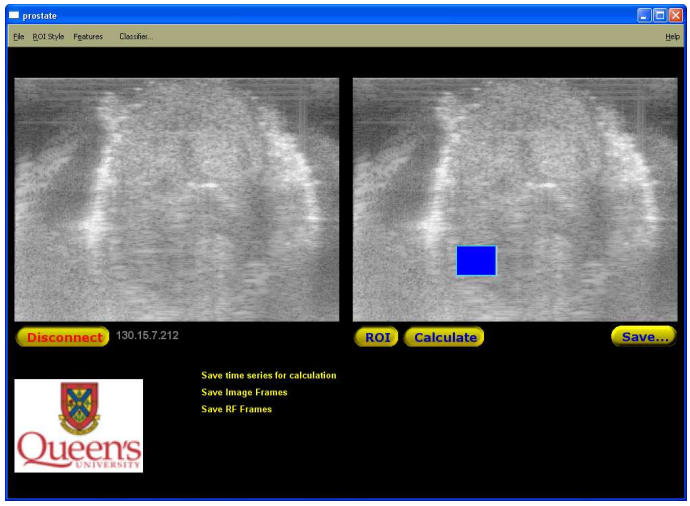

Figure 7.1: The GUI of a software system under development for real-time creation of cancer probability maps during biopsy.

The data collection and feature computation functions are already in place. Figure 7.1 demonstrates the proposed GUI.

Bibliography

[1] P. Abolmaesumi and M. R. Sirouspour, "Segmentation of prostate contours from ultrasound images," in *IEEE International Conference on Acoustics, Speech and Signal Processing (ICASSP)*, 2004, pp. 517–520.

[2] A. Accardo, M. Affinito, M. Carrozzi, and F. Bouquet, "Use of the fractal dimension for the analysis of electroencephalographic time series," *Biological Cybernetics*, vol. 77, no. 5, pp. 339–350, 1997.

[3] B. L. Adam, Y. Qu, J. W. Davis, M. D. Ward, M. A. Clements, L. H. Cazares, O. J. Semmes, P. F. Schellhammer, Y. Yasui, Z. Feng, and G. L. Wright, "Serum protein fingerprinting coupled with a pattern-matching algorithm distinguishes prostate cancer from benign prostate hyperplasia and healthy men," *Cancer Research*, vol. 62, no. 13, pp. 3609–3614, 2002.

[4] S. K. Alam, E. J. Feleppa, A. Kalisz, S. Ramchandran, R. D. Ennis, F. L. Lizzi, C. S. Wuu, and J. Ketterling, "Prostate elastographypreliminary in vivo results," in *SPIE Medical Imaging: Ultrasonic Imaging and Signal Processing*, W. F. Walker and S. Y. Emelianov, Eds., vol. 5750, 2005, pp. 339–345.

[5] P. H. Arger, B. Malkowicz, K. N. Van Arsdalen, C. M. Sehgal, A. Holzer, and S. M. Schultz, "Color and power Doppler sonography in the diagnosis of prostate cancer," *Journal of Ultrasound in Medicine*, vol. 23, no. 1, pp. 623–630, 2004.

[6] E. Balogh, A. Deguet, R. C. Susil, A. Krieger, A. Viswanathan, C. Menard, J. A. Coleman, and G. Fichtinger, "Visualization, planning, and monitoring software for MRI-guided prostate intervention robot," in *Medical Image Computing and Computer Assisted Intervention*, ser. LNCS, T. Dohi and R. Kikinis, Eds., vol. 3217. Berlin Heidelberg: Springer-Verlag, 2004, pp. 73–80.

[7] J. C. Bamber and R. J. Dickinson, "Ultrasonic b-scanning: a computer simulation," *Physics in Medicine and biology*, vol. 25, no. 3, pp. 463–479, 1980.

[8] P. H. Bartels, T. Gahm, and D. Thompson, "Automated microscopy in diagnostic histopathology: From image processing to automated reasoning," *International Journal of Imaging Systems and Technology*, vol. 8, no. 2, pp. 214–223, 1997.

[9] O. Basset, Z. Sun, J. L. Mestas, and G. Gimenez, "Texture analysis of ultrasonic images of the prostate by means of cooccurrence matrices," *Ultrasonic Imaging*, vol. 15, no. 3, pp. 218–237, 1993.

[10] M. Baumann, P. Mozer, V. Daanen, and J. Troccaz, "Towards 3d ultrasound image based soft tissue tracking: A transrectal ultrasound prostate image alignment system," in *Medical Image Computing and Computer Assisted Intervention*, ser. LNCS, N. Ayache, S. Ourselin, and A. Maeder, Eds., vol. 4792, 2007, pp. 26–33.

[11] F. Beckers, B. Verheyden, K. Couckuyt, and A. Aubert, "Fractal dimension in health and heart failure," *Biomedizinische Technik. Biomedical Engineering*, vol. 51, no. 4, pp. 194–197, 2006.

[12] T. A. Bigelow and W. D. O'Brien, "Scatterer size estimation in pulse-echo ultrasound using focused sources: calibration measurements and phantom experiments," *The Journal of the Acoustical Society of America*, vol. 116, no. 1, pp. 594–602, 2004.

[13] C. M. Bishop, *Pattern Recognition and Machine Learning*. NY: Springer Science, 2006.

[14] J. S. Bleck, U. Ranft, H. Gebel, M. Hecker, C. Westhoffbleck, Thiesemann, and S. Wagner, "Random field models in the texture analysis of ultrasonic images of liver," *IEEE Transactions on Medical Imaging*, vol. 15, no. 3, pp. 796–801, 1996.

[15] H. A. Bogers, J. P. M. Sedelaar, H. P. Beerlage, J. Rosette, F. M. J. Debruyne, H. Wijkstra, and R. G. Aarnink, "Contrast-enhanced three-dimensional power Doppler angiography of the human prostate: correlation with biopsy outcome," *Urology*, vol. 54, no. 1, pp. 97–104, 1999.

[16] P. Boyle and J. Ferlay, "Cancer incidence and mortality in europe, 2004," *Annals of Oncology*, vol. 16, no. 3, pp. 481–488, 2005.

[17] M. Braun, *Differential Equations and Their Applications : An Introduction to Applied Mathematics*, 4th ed., ser. Texts in Applied Mathematics. NY: Springer, 1993.

[18] M. K. Brawer, R. E. Deering, M. Brown, S. D. Preston, and S. A. Bigler, "Predictor of pathologic stage in prostatic carcinoma: the role of neovascularity," *Cancer*, vol. 73, no. 3, pp. 678–687, 1994.

[19] G. Brown, D. A. Macvicar, V. Ayton, and J. E. Husband, "The role of intravenous contrast enhancement in magnetic resonance imaging of prostatic carcinoma," *Clinical Radiology*, vol. 50, no. 2, pp. 601–606, 1995.

[20] E. Bullitt, I. Jung, K. Muller, G. Gerig, S. Aylward, S. Joshi, K. Smith, W. Lin, and M. Ewend, "Determining malignancy of brain tumors by analysis of vessel shape," in *Medical Image Computing and Computer Assisted Intervention*, ser. LNCS, C. Barillot, D. R. Haynor, and P. Hellier, Eds., vol. 3217, 2004, pp. 645–653.

[21] Canadian Cancer Society, "Canadian cancer statistics," [Online]. Available: http://www.cancer.ca/, Access Date, July 2008.

[22] B. Castaneda, K. Hoyt, M. Zhang, D. Pasternack, L. Baxter, P. Nigwekar, A. SantAgnese, J. Joseph, J. Strang, D. J. Rubens, and K. J. Parker, "Prostate cancer detection based on three dimensional sonoelastography," in *IEEE Ultrasonics Symposium*, 2007, pp. 1353–1356.

[23] J. Chappelowa, A. Madabhushia, M. Rosenb, J. Tomaszeweskic, and M. Feldman, "Multimodal image registration of ex vivo 4 tesla MRI with whole mount histology for prostate cancer detection," in *SPIE Medical Imaging: Image Processing*, J. P. W. Pluim and J. M. Reinhardt, Eds., vol. 6512, 2007, pp. 65 121S1–12.

[24] M. J. T. M. Cloostermans and J. M. Thijssen, "A beam corrected estimation of the frequency dependent attenuation of biological tissues from backscattered ultrasound," *Ultrasonic Imaging*, vol. 5, no. 2, pp. 136–147, 1983.

[25] N. A. Cohn, S. Y. Emelianov, M. A. Lubinski, and M. O'Donnell, "An elasticity microscope. part i: Methods, and. part ii: Experimental results," *IEEE Transactions on Ultrasonics, Ferroelectrics and Frequency Control*, vol. 44, no. 6, pp. 1304–1331, 1997.

[26] R. A. Cormack, A. V. D'Amico, N. Hata, S. Silverman, M. Weinstein, and C. M. Tempany, "Feasibility of transperineal prostate biopsy under interventional magnetic resonance guidance," *Journal of Urology*, vol. 56, no. 4, pp. 663–664, 2000.

[27] M. J. Costa, H. Delingette, S. Novellas, , and N. Ayache, "Automatic segmentation of bladder and prostate using coupled 3d deformable models," in *Medical Image Computing and Computer Assisted Intervention*, ser. LNCS, N. Ayache, S. Ourselin, and A. Maeder, Eds., vol. 4791, 2007, pp. 252–260.

[28] L. C. Costello and R. B. Franklin, "Citrate metabolism of normal and malignant prostate epithelial cells," *Urology*, vol. 50, no. 1, pp. 3–12, 1997.

[29] P. Courtis and A. Samani, "Detecting mechanical abnormalities in prostate tissue using FE-based image registration," in *Medical Image Computing and Computer Assisted Intervention*, ser. LNCS, N. Ayache, S. Ourselin, and A. Maeder, Eds., vol. 4792, 2007, pp. 244–251.

[30] A. V. D'Amico, C. M. Tempany, R. Cormack, N. Hata, M. Jinzaki, K. Tuncali, M. Weinstein, and J. P. Richie, "Transperineal magnetic resonance image guided prostate biopsy," *Journal of Urology*, vol. 164, no. 2, pp. 385–387, 2000.

[31] J. S. DaPonte, J. Parikh, J. Vitale, and J. Decker, "Ultrasonic image texture classification using Markov random field models," in *SPIE Conference on Applications of Artificial Neural Networks*, S. K. Rogers and D. W. Ruck, Eds., vol. 2243, 1994, pp. 266–271.

[32] N. A. Dawson and N. J. Vogelzang, *Prostate Cancer*. New-York: Wiley-Liss, 1994.

[33] S. M. Dhanasekaran, T. R. Barrette, D. Ghosh, R. Shah, S. Varambally, K. Kurachi, K. J. Pienta, M. A. Rubin, and A. M. Chinnaiyan, "Delineation of prognostic biomarkers in prostate cancer," *Nature*, vol. 412, no. 6849, pp. 822–826, 2001.

[34] S. DiMaio and S. Salcudean, "Needle insertion modelling for the interactive simulation of percutaneous procedures," in *Medical Image Computing and Computer Assisted Intervention*, ser. LNCS, T. Dohi and R. Kikinis, Eds., vol. 2489. Berlin Heidelberg: Springer-Verlag, 2002, pp. 253–260.

[35] M. Ding, C. Chen, Y. Wang, I. Gyacskov, and A. Fenster, "Prostate segmentation in 3D US images using the cardinal-spline-based discrete dynamic contour," in *SPIE Medical Imaging: Visualization, Image-Guided Procedures, and Display*, R. L. Galloway, Ed., vol. 5029, 2003, pp. 69–76.

[36] B. Djavan, A. Zlotta, C. Kratzik, M. Remzi, C. Seitz, C. C. Schulman, and M. Marberger, "PSA, PSA density, PSA density of transition zone, free/total PSA ratio, and PSA velocity for early detection of prostate cancer in men with serum PSA 2.5 to 4," *Urology*, vol. 54, no. 3, pp. 517–523, 1999.

[37] K. D. Donohue, L. Huang, T. Burks, F. Forsberg, and C. W. Piccoli, "Tissue classification with generalized spectrum parameters," *Ultrasound in Medicine and Biology*, vol. 27, no. 11, pp. 1505–1514, 2001.

[38] D. B. Downey, A. Fenster, and J. C. Williams, "Clinical utility of three-dimensional US," *Radiographics*, vol. 20, no. 2, pp. 559–571, 2000.

[39] S. Doyle, M. Hwang, K. Shah, A. Madabhushi, M. Feldman, and J. Tomaszeweski, "Automated grading of prostate cancer using architectural and textural image features," in *IEEE International Symposium on Biomedical Imaging: From Nano to Macro*, 2007, pp. 1284–1287.

[40] S. Doyle, A. Madabhushi, M. Feldman, and J. Tomaszeweski, "A boosting cascade for automated detection of prostate cancer from digitized histology," in *Medical Image Computing and Computer Assisted Intervention*, ser. LNCS, R. Larsen, M. Nielsen, and J. Sporring, Eds., vol. 4191, 2006, pp. 504–511.

[41] F. Dunn, *Ultrasonic Tissue Characterization*. Urbana, IL: Springer-Verlag, 1996.

[42] W. J. Ellis and M. K. Brawer, "Repeat prostate needle biopsy: who needs it?" *Journal of Urology*, vol. 153, no. 5, pp. 1496–1498, 1995.

[43] S. Y. Emelianov, X. C. M. O'Donnell, B. Knipp, D. Myers, T. W. Wakefield, and J. M. Rubin, "Triplex ultrasound: Elasticity imaging to age deep venous thrombosis," *Ultrasound in Medicine and Biology*, vol. 28, no. 6, pp. 757–767, 2002.

[44] R. Q. Erkamp, A. R. Skovoroda, S. Y. Emelianov, and M. O'Donnell, "Measuring the nonlinear elastic properties of tissue-like phantoms," *IEEE Transactions on Ultrasonics, Ferroelectrics, and Frequency Control*, vol. 51, no. 4, pp. 410–419, 2004.

[45] R. Esteller, G. Vachtsevanos, J. Echauz, and B. Litt, "A comparison of fractal dimension algorithms," *IEEE Transactions on Circuits and Systems*, vol. 48, no. 2, pp. 177–183, 2001.

[46] D. H. Evans and W. N. McDicken, *Doppler Ultrasound.* UK: John Wiley and Sons, 2000.

[47] R. E. Fan, P. H. Chen, and C. J. Lin, "Working set selection using the second order information for training SVM," *Machine Learning Research*, vol. 6, no. 1, pp. 1889–1918, 2005.

[48] R. Farjam, H. Soltanian-Zadeh, R. A. Zoroofi, and K. Jafari-Khouzani, "Tree-structured grading of pathological images of prostate," in *SPIE Medical Imaging: Image Processing*, J. M. Fitzpatrick and J. M. Reinhard, Eds., vol. 5747, 2005, pp. 840–851.

[49] M. Fatemi and J. F. Greenleaf, "Ultrasound-stimulated vibro-acoustic spectrography," *Science*, vol. 280, no. 5360, pp. 82–85, 1998.

[50] B. Fei, J. L. Duerk, D. T. Boll, J. S. Lewin, and D. L.Wilson, "Slice-to-volume registration and its potential application to interventional MRI-guided radio-frequency thermal ablation of prostate cancer," *IEEE Transactions on Medical Imaging*, vol. 22, no. 4, pp. 515–524, 2003.

[51] B. Fei, Z. Lee, D. T. Boll, J. S. L. Jeffery L. Duerk, D. Bruce Sodee, and D. L. Wilson, "Registration and fusion of SPECT, high-resolution MRI, and interventional MRI for thermal ablation of prostate cancer," *IEEE Transactions on Nuclear Science*, vol. 51, no. 1, pp. 177–183, 2004.

[52] E. J. Feleppa, S. Dasgupta, A. Kalisz, J. Ketterling, S. Ramachandran, C. R. Porter, M. Lacrampe, D. Dail, D. Sparks, and F. Arias-Mendosa, "New developments in tissue-type imaging (TTI) of prostate cancer: combined ultrasonic and magnetic-resonance methods," in *IEEE Ultrasonics Symposium*, vol. 2, 2005, pp. 831–834.

[53] E. J. Feleppa, S. Dasgupta, J. A. Ketterling, A. Kalisz, C. R. Porter, M. Lacrampe, D. Dail, T. Liu, F. Arias-Mendoza, and M. Mansukhani, "Tissue-type imaging (TTI) of prostate cancer based on combined ultrasonic and magnetic-resonance methods: Latest developments," in *IEEE Ultrasonics Symposium*, 2006.

[54] E. J. Feleppa, W. R. Fair, T. Liu, N. Fleshner, V. Reuter, A. Kalisz, M. Cookson, and A. Rosado, "3-D tissue typing of prostate tissue based on spectral parameters," in *IEEE Ultrasonics Symposium*, 1995, pp. 1171–1175.

[55] E. J. Feleppa, A. Kalisz, J. B. Sokil-Melgar, F. L. Lizzi, T. Liu, A. L. Rosado, M. C. Shao, W. R. Fair, Y. Wang, M. S. Cookson, V. E. Reuter, and W. D. W.

Heston, "Typing of prostate tissue by ultrasonic spectrum analysis," *IEEE Transactions on Ultrasonics, Ferroelectrics, and Frequency Control*, vol. 43, no. 4, pp. 609–619, 1996.

[56] E. J. Feleppa, J. A. Ketterling, A. Kalisz, S. Urban, C. Porter, J. Gillespie, B. P. Schiff, R. D. Ennis, C. S. Wuu, J. W. Moul, I. A. Sesterhenn, and P. J. Scardino, "Prostate imaging based on RF spectrum analysis and nonlinear classifiers for guiding biopsies and targeting radiotherapy," in *SPIE Medical Imaging: Ultrasonic Imaging and Signal Processing*, M. F. Insana and K. K. Shung, Eds., vol. 4325, 2001, pp. 371–379.

[57] E. J. Feleppa, J. A. Ketterling, A. Kalisz, S. Urban, C. R. Porter, J. W. Gillespie, P. B. Schiff, R. D. Ennis, and C. S. W. abd W R Fair, "Advanced ultrasonic tissue-typing and imaging based on radio-frequency spectrum analysis and neural-network classification for guidance of therapy and biopsy procedure," in *Computer-Assisted Radiology and Surgery*, ser. International Congress Series, H. U. Lemke, M. W. Vannier, K. Inamura, A. G. Farman, and K. Doi, Eds., vol. 1230, 2001, pp. 346–351.

[58] E. J. Feleppa, P. Lee, S. Urban, J. Ketterling, F. Arias-Mendoza, and G. Kutcher, "Progress in characterizing and imaging prostate tissues for guiding biopsies and planning and targeting treatment of prostate cancer," in *IEEE Ultrasonics Symposium*, 2003, pp. 1018–1021.

[59] E. J. Feleppa, T. Liu, A. Kalisz, A. Rosado, W. Larchian, W. R. Fair, H. Tsai, C. Porter, and V. Reuter, "2- and 3-D differentiation of cancerous from benign prostate tissue for diagnosis, monitoring, and planning based on spectrum

analysis," in *IEEE Ultrasonics Symposium*, 1997, pp. 1131–1135.

[60] E. J. Feleppa, C. R. Porter, J. Ketterling, P. Lee, S. Dasgupta, S. Urban, and A. Kalisz, "Recent developments in tissue-type imaging (TTI) for planning and monitoring treatment of prostate cancer," *Ultrasonic Imaging*, vol. 26, no. 3, pp. 163–172, 2004.

[61] A. Fenster, K. Surry, W. Smith, and D. Downey, "The use of three-dimensional ulstrasound imaging in breast biopsy and prostate therapy," *Measurement*, vol. 36, no. 3–4, pp. 245–256, 2004.

[62] G. Fichtinger, A. Krieger, R. C. Susil, A. Tanacs, L. L. Whitcomb, and E. Atalar, "Transrectal prostate biopsy inside closed MRI scanner with remote actuation, under real-time image guidance," in *Medical Image Computing and Computer Assisted Intervention*, ser. LNCS, T. Dohi and R. Kikins, Eds., vol. 2488, 2002, pp. 91–98.

[63] G. Fichtinger, J. Fiene, C. W. Kennedy, G. Kronreif, I. Iordachita, D. Y. Song, E. C. Burdette, and P. Kazanzides, "Robotic assistance for ultrasound guided prostate brachytherapy," in *Medical Image Computing and Computer Assisted Intervention*, ser. LNCS, N. Ayache, S. Ourselin, and A. Maeder, Eds., vol. 4791, 2007, pp. 119–127.

[64] F. S. Foster, C. J. Pavlin, K. A. Harasiewicz, D. A. Christopher, and D. H. Turnbull, "Advances in ultrasound biomicroscopy," *Ultrasound in Medicine and Biology*, vol. 26, no. 1, pp. 1–27, 2000.

[65] D. Freedman, R. J. Radke, T. Zhang, Y. Jeong, D. M. Lovelock, and G. T. Y. Chen, "Model-based segmentation of medical imagery by matching distributions," *IEEE Transactions on Medical Imaging*, vol. 24, no. 3, pp. 281–292, 2005.

[66] L. Gao, K. J. Parker, R. M. Lerner, and S. F. Levinson, "Imaging the elastic properties of tissue - a review," *Ultrasound in Medicine and Biology*, vol. 22, no. 8, pp. 959–977, 1996.

[67] J. M. Garcia-Segura, M. Sanchez-Chapado, C. Ibarburen, J. Viano, J. C. Angulo, J. Gonzalez, and J. M. Rodriguez-Vallejo, "In vivo proton magnetic resonance spectroscopy of diseased prostate: Spectroscopic features of malignant versus benign pathology," *Magnetic Resonance Imaging*, vol. 17, no. 5, pp. 755–765, 1999.

[68] A. Ghanei, H. Soltanian-Zadeh, A. Ratkewicz, and F. F. Yin, "A three-dimensional deformable model for segmentation of human prostate from ultrasound images," *Medical Physics*, vol. 28, no. 10, pp. 2147–2153, 2001.

[69] D. E. Goertz, "High-frequency color flow imaging of the microcirculation," *Ultrasound in Medicine and Biology*, vol. 26, no. 1, pp. 62–71, 2000.

[70] O. Goksel, R. Z. Azar, and S. E. Salcudean, "Simulation of ultrasound radio-frequency signals in deformed tissue for validation of 2d motion estimation with sub-sample accuracy," in *International Conference of the IEEE Engineering in Medicine and Biology Society*, 2007, pp. 87–90.

[71] O. Goksel, S. E. Salcudean, S. P. DiMaio, R. Rohling, and J. Morris, "3D needle-tissue interaction simulation for prostate brachytherapy," in *Medical Image Computing and Computer Assisted Intervention*, ser. LNCS, J. Duncan and G. Gerig, Eds., vol. 3749. Berlin Heidelberg: Springer-Verlag, 2005, pp. 827–834.

[72] L. G. Gomella, E. A. El-Gabry, S. E. Strup, and E. Halpern, "Ultrasound contrast agents for prostate imaging and biopsy," *Urologic Oncology*, vol. 6, no. 5, pp. 189–192, 2001.

[73] L. Gong, L. Ng, S. D. Pathak, I. Tutar, P. S. Cho, D. R. Haynor, and Y. Kim, "Prostate ultrasound image segmentation using level set-based region flow with shape guidance," in *SPIE Medical Imaging: Image Processing*, J. M. Fitzpatrick and J. M. Reinhard, Eds., vol. 5747, 2005, pp. 1648–1657.

[74] L. Gong, S. D. Pathak, D. R. Haynor, P. S. Cho, and Y. Kim, "Parametric shape modeling using deformable superellipses for prostate segmentation," *IEEE Transactions on Medical Imaging*, vol. 23, no. 3, pp. 340–349, 2004.

[75] T. E. B. Goossen, J. de la Rosette, C. A. Van De Hulsbergen, G. L. Leenders, and H. Wijkstra, "The value of dynamic contrast enhanced power Doppler ultrasound imaging in the localization of prostate cancer," *European Urology*, vol. 43, no. 2, pp. 124–131, 2003.

[76] J. F. Greenleaf, *Tissue Characterization with Ultrasound*. Boca Raton, FL: CRC Press, 1986.

[77] Y. Hamamoto, S. Uchimura, and S. Tomita, "On the behavior of artificial neural network classifiers in high-dimensional spaces," *IEEE Transactions on Pattern Analysis and Machine Intelligence*, vol. 18, no. 5, pp. 571–574, 1996.

[78] S. M. Han, H. J. Lee, and J. Y. Choi, "Prostate cancer detection using texture and clinical features in ultrasound image," in *IEEE International Conference on Information Acquisition*, 2007, pp. 547–552.

[79] R. M. Haralick, K. Shanmugam, and I. Dinstein, "Texture parameters for image classification," *IEEE Transactions on Systems, Man and Cybernetics*, vol. 3, no. 6, pp. 610–621, 1973.

[80] N. Hata, M. J. D. Kacher, R. Cormak, D. Gering, A. Nabavi, S. G. Silverman, A. V. D'Amico, R. Kikinis, F. A. Jolesz, and C. N. Tempany, "imaging-guided prostate biopsy with surgical navigation software: device validation and feasibility," *Radiology*, vol. 220, no. 2, pp. 263–268., 2001.

[81] W. R. Hedrick, D. L. Hykes, and D. E. Starchman, *Ultrasound physics and instrumentation.* St. Louis, Mo: Elsevier Mosby, 2005.

[82] G. Henderson, E. Ifeachor, N. Hudson, C. Goh, N. Outram, Wimalaratna, C. D. Percio, and F. Vecchio, "Development and assessment of methods for detecting dementia using the human electroencephalogram," *IEEE Transactions on Biomedical Engineering*, vol. 53, no. 8, pp. 1557–1668, 2006.

[83] T. Higuchi, "Approach to an irregular time series on the basis of the fractal theory," *Physica D: Nonlinear Phenomena*, vol. 31, no. 2, pp. 277–283, 1988.

[84] K. K. Hodge, J. E. McNeal, M. K. Terris, and T. A. Stamey, "Random systematic versus directed ultrasound guided transrectal core biopsies of the prostate," *Journal of Urology*, vol. 142, no. 1, pp. 71–75, 1989.

[85] A. G. Houston, S. B. Premkumar, D. E. Pitts, and R. J. Babaian, "Prostate ultrasound image analysis: localization of cancer lesions to assist biopsy," in *IEEE Symposium on Computer-Based Medical Systems*, 1995, pp. 94–101.

[86] N. Hu, D. B. Downey, A. Fenster, and H. M. Ladak, "Prostate boundary segmentation from 3D ultrasound images," *Medical Physics*, vol. 30, no. 7, pp. 1648–1659, 2003.

[87] A. L. Huynen, R. J. Giesen, J. J. Rosette, R. G. Aarnink, F. M. Debruyne, and H. Wijkstra, "Analysis of ultrasonographic prostate images for the detection of prostatic carcinoma: the automated urologic diagnostic expert system," *Ultrasound in Medicine and Biology*, vol. 20, no. 1, pp. 1–10, 1994.

[88] M. Inahara, "Clinical evaluation of transrectal power Doppler imaging in the detection of prostate cancer," *International Urology and Nephrology*, vol. 36, no. 2, pp. 175–180, 2004.

[89] E. P. Ives, I. Waldman, L. G. Gomella, and E. J. Halpern, "Preliminary experience with prostate elastography and comparison with biopsy results," in *Prostate Cancer Symposium*, 2005, p. 55.

[90] K. Jafari-Khouzani and H. Soltanian-Zadeh, "Multiwavelet grading of pathological images of prostate," *IEEE Transactions on Biomedical Engineering*, vol. 50, no. 6, pp. 697–704, 2003.

[91] A. Jain, A. Deguet, I. Iordachita, G. Chintalapani, J. Blevins, Y. Le, E. Armour, C. Burdette, D. Song, and G. Fichtinger, "Intra-operative 3D guidance in prostate brachytherapy using a non-isocentric C-arm," in *Medical Image Computing and Computer Assisted Intervention*, ser. LNCS, N. Ayache, S. Ourselin, and A. Maeder, Eds., vol. 4792, 2007, pp. 9–17.

[92] A. Jemal, "Cancer statistics, 2004," *CA: A Cancer Journal for Clinicians*, vol. 54, no. 1, pp. 8–29, 2004.

[93] A. Jemal, R. Siegel, E. Ward, T. Murray, J. Xu, and M. Thun, "Cancer statistics, 2007," *CA: A Cancer Journal for Clinicians*, vol. 57, no. 1, pp. 43–66, 2007.

[94] A. J. Jensen, *Imaging of Complex Media with Acoustic and Siesmic Waves*, ser. Topics in Applied Physics. Springer-Verlag, 2002, vol. 84, ch. Ultrasound and its modeling, pp. 135–164.

[95] J. A. Jensen, "Field: A program for simulating ultrasound systems," *Medical & Biological Engineering & Computing*, vol. 34, Supplement 1, Part 1, pp. 351–353, 1996.

[96] J. A. Jensen and I. Nikolov, "Fast simulation of ultrasound images," in *IEEE Ultrasonics Symposium*, 2000, pp. 1721–1724.

[97] J. A. Jensen and N. B. Svendsen, "Calculation of pressure fields from arbitrarily shaped, apodized, and excited ultrasound transducers," *IEEE Transactions on Ultrasonics, Ferroelectrics, and Frequency Control*, vol. 39, no. 2, pp. 262–267, 1992.

[98] J. Jossinet, E. Marry, and A. Montalibet, "Electrical impedance endotomography: Imaging tissue from inside," *IEEE Transactions on Medical Imaging*, vol. 21, no. 6, pp. 560–565, 2002.

[99] I. D. Kaplan, E. J. Holupka, P. Meskal, S. J. Soon, B. Saltzman, P. Church, and G. P. Kearney, "Intraoperative treatment planning for radioactive seed implant therapy for prostate cancer," *Urology*, vol. 56, no. 3, pp. 492–495, 2000.

[100] I. D. Kaplana, N. E. Oldenburga, P. Meskella, M. Blakeb, P. Churchc, and E. J. Holupkaa, "Real time MRI-ultrasound image guided stereotactic prostate biopsy," *Magnetic Resonance Imaging*, vol. 20, no. 3, pp. 295–299, 2002.

[101] A. Katouzian, S. Sathyanarayana, B. Baseri, E. E. Konofagou, , and S. G. Carlier, "Challenges in atherosclerotic plaque characterization with intravascular ultrasound (IVUS): From data collection to classification," *IEEE Transcations on Information Technology in Biomedicine*, vol. 12, no. 3, pp. 315–327, 2008.

[102] A. Katouzian, S. Sathyanarayana, W. Li, T. Thomas, and S. G. Carlier1, "Challenges in tissue characterization from backscattered intravascular ultrasound signals," in *SPIE Medical Imaging: Ultrasonic Imaging and Signal Processing*, S. Y. Emelianov and S. A. McAleavey, Eds., vol. 6513, 2007, pp. 65 130P1–65 130P10.

[103] M. Katz, "Fractals and the analysis of waveforms," *Computers in Biology and Medicine*, vol. 18, no. 3, pp. 145–156, 1988.

[104] F. A. Khan, M. E. Laniado, B. Holloway, and A. Kaisary, "MRI is too insensitive to stage early prostate cancer," *European Urology Supplements*, vol. 1, no. 1, p. 76, 2003.

[105] J. K. Kim, D. Y. Kim, Y. H. Lee, N. K. Sung, D. S. Chung, O. D. Kim, and K. Kim, "In vivo differential diagnosis of prostate cancer and benign prostatic hyperplasia: Localized proton magnetic resonance spectroscopy using external-body surface coil," *Magnetic Resonance Imaging*, vol. 16, no. 10, pp. 1281–1288, 1998.

[106] M. Kojima and H. Watanabe, "Preliminary results of power Doppler imaging in benign prostatic hyperplasia," *Ultrasound in Medicine and Biology*, vol. 23, no. 9, pp. 1305–1309, 1997.

[107] M. C. Kolios and R. E. Baddour, "Investigating the effect of cell size on the backscatter from suspensions of varying volume fractions," in *IEEE Ultrasonics Symposium*, 2006, pp. 637–640.

[108] E. E. Konofagou, "Quo vadis elasticity imaging?" *Ultrasonics*, vol. 42, no. 1, pp. 331–336, 2004.

[109] E. Konofagou, J. Thierman, and K. Hynynen, "A focused ultrasound method for simultaneous diagnostic and therapeutic applicationsa simulation study," *Physics in Medicine and Biology*, vol. 46, no. 11, pp. 2967–2984, 2001.

[110] E. E. Konofagou and K. Hynynen, "Localaized harmonic motion imaging: Theory, simulations and experiments," *Ultrasound in Medicine and Biology*, vol. 28, no. 10, pp. 1405–1413, 2003.

[111] S. Kravchick, S. Cytron, R. Peled, A. Altshuler, and D. Ben-Dor, "Using gray-scale and two different techniques of color Doppler sonography to detect prostate cancer," *Urology*, vol. 61, no. 5, pp. 977–981, 2003.

[112] A. Krieger, R. C. Susil, C. Menard, J. A. Coleman, G. F. E. Atalar, and L. L. Whitcomb, "Design of a novel MRI compatible manipulator for image guided prostate interventions," *IEEE Transactions on Biomedical Engineering*, vol. 52, no. 2, pp. 306–313, 2005.

[113] S. A. Kruse, J. A. Smith, A. J. Lawrence, M. A. D. A. Manduca, J. F. Greenleaf, and R. L. Ehman, "Tissue characterization using magnetic resonance elastography: preliminary results," *Physics in Medicine and Biology*, vol. 45, no. 6, pp. 1579–1590, 2000.

[114] Kumar, Abbas, Fausto, and Mitchell, *Basic Pathology*, 8th ed. PA, USA: Saunders, Elsevier, 2007.

[115] J. Kurhanewicz, M. G. Swanson, S. J. Nelson, and D. B. Vigneron, "Combined magnetic resonance imaging and spectroscopic imaging approach to molecular imaging of prostate cancer," *Journal of Magnetic Resonance Imaging*, vol. 16, no. 4, pp. 451–463, 2002.

[116] H. Ladak, F. Mao, Y. Wang, D. Downey, D. Steinman, and A. Fenster, "Boundary segmentation from 2D ultrasound images," *Medical Physics*, vol. 27, no. 8, pp. 1777–1788, 2000.

[117] H. M. Ladak, Y. Wang, D. B. Downey, and A. Fenster, "Testing and optimization of a semiautomatic prostate boundary segmentation algorithm using virtual operators," *Medical Physics*, vol. 30, no. 7, pp. 1637–1647, 2003.

[118] J. Lapointe, C. Li, J. P. Higgins, M. Van Der Rijn, E. Bair, K. Montgomery, M. Ferrari, L. Egevad, W. Rayford, U. Bergerheim, P. Ekman, A. DeMarzo, R. Tibshirani, D. Botstein, P. O. Brown, J. D. Brooks, and J. R. Pollack, "Gene expression profiling identifies clinically relevant subtypes of prostate cancer," *Proceedings of the National Academy of Science*, vol. 101, no. 3, pp. 811–816, 2004.

[119] E. LaTulippe, J. Satagopan, A. Smith, H. Scher, P. Scardino, V. Reuter, and W. L. Gerald, "Comprehensive gene expression analysis of prostate cancer reveals distinct transcriptional programs associated with metastatic disease," *Cancer Research*, vol. 62, no. 15, pp. 4499–4506, 2001.

[120] J. Z. Lee, S. Omata, B. Tillig, I. Perkash, and C. E. Constantinou, "Chronology and urodynamic characterization of micturition in neurohormonally induced experimental prostate growth in the rat," *Neurourology and Urodynamics*, vol. 17, no. 1, pp. 55–69, 1998.

[121] W. L. Lee, Y. C. Chen, and Hsieh, "Ultrasonic tissues classification by fractal feature vector based on m-band wavelet transform," *IEEE Transactions on Medical Imaging*, vol. 22, no. 3, pp. 382–392, 2003.

[122] Y. Li and J. A. Hossack, "Combined elasticity and 3D imaging of the prostate," in *SPIE Medical Imaging: Ultrasonic Imaging and Signal Processing*, W. F. Walker and S. Y. Emelianov, Eds., vol. 5750, 2005, pp. 7–15.

[123] H. Liebgott, O. Bernard, C. Cachard, and D. Friboulet, "Field simulation parameters design for realistic statistical parameters of radio - frequency ultrasound images," in *IEEE Ultrasonics Symposium*, 2007, pp. 2247–2250.

[124] G. P. Liney, M. L. Lindsay, W. Turnbull, D. J. Manton, A. J. Knowles, S. J. Blackband, and A. Horsman, "Proton MR T2 maps correlate with the citrate concentration in the prostate," *NMR in Biomedicine*, vol. 9, no. 2, pp. 59–64, 1996.

[125] G. P. Liney, L. W. Turnbull, and A. J. Knowles, "In vivo magnetic resonance spectroscopy and dynamic contrast enhanced imaging of the prostate gland," *Magnetic Resonance Imaging*, vol. 17, no. 5, pp. 755–765, 1999.

[126] M. Linzer and S. J. Norton, "Ultrasonic tissue characterization," *Annual reviews of Biophysics and Bioengineering*, vol. 11, no. 1, pp. 303–329, 1982.

[127] H. Liu, G. Cheng, D. Rubens, J. G. Strang, L. Liao, R. Brasacchio, E. Messing, and Y. Yu, "Automatic segmentation of prostate boundaries in transrectal ultrasound (TRUS) imaging," in *SPIE Medical Imaging: Visualization, Image-Guided Procedures, and Display*, M. Sonka and J. M. Fitzpatrick, Eds., vol. 4684, 2002, pp. 412–423.

[128] F. L. Lizzi, E. J. Feleppa, S. K. Alam, and X. C. Deng, "Ultrasonic spectrum analysis for tissue evaluation," *Pattern Recognition Letters*, vol. 24, no. 4–5, pp. 637–658, 2003.

[129] F. L. Lizzi, E. J. Feleppa, M. Astor, and A. Kalisz, "Statistics of ultrasonic spectral parameters for prostate and liver examination," *IEEE Transactions on*

Ultrasonics, Ferroelectrics, and Frequency Control, vol. 44, no. 4, pp. 935–942, 1997.

[130] F. L. Lizzi, M. Greenebaum, E. J. Feleppa, M. Elbaum, and D. J. Coleman, "Theoretical framework for spectrum analysis in ultrasonic tissue characterization," *Journal of the Acoustic Society of America*, vol. 73, no. 3, pp. 1366–1373, 1983.

[131] F. L. Lizzi, M. Ostromogilsky, E. J. Feleppa, , and M. Yaremko, "Relationship of ultrasonic spectral parameters to features of tissue microstructure," *IEEE Transactions on Ultrasonics, Ferroelectrics and Frequency Control*, vol. 34, no. 3, pp. 319–329, 1986.

[132] R. Llobet, J. C. Perez-Cortes, A. H. Toselli, and A. Juan, "Computer-aided detection of prostate cancer," *International Journal of Medical Informatics*, vol. 76, no. 7, pp. 547–556, 2007.

[133] A. Lorenz, H. J. Sommerfeld, M. Garcia-Schurmann, S. Philippou, T. Senge, and H. Ermert, "A new system for the acquisition of ultrasonic multicompression strain images of the human prostate in vivo," *IEEE Transactions on Ultrasonics, Ferroelectrics and Frequency Control*, vol. 46, no. 5, pp. 1147–1154, 1999.

[134] A. Madabhushi, M. D. Feldman, D. N. Metaxas, J. Tomaszeweski, and D. Chute, "Automated detection of prostatic adenocarcinoma from high-resolution ex-vivo MRI," *IEEE Transactions on Medical Imaging*, vol. 24, no. 12, pp. 1611–1625, 2005.

[135] E. L. Madsen, M. A. Hobson, H. Shi, T. Varghese, and G. R. Frank, "Tissue-mimicking agar/gelatin materials for use in heterogeneous elastography phantoms," *Physics in Medicine and Biology*, vol. 50, no. 23, pp. 5597–5618, 2005.

[136] B. B. Mandelbrot, *Gaussian Self-Affinity and Fractals.* Harrisonburg, VA: Springer, 2002.

[137] A. Manduca, T. Oliphant, M. Dresner, J. Mahowald, S. Kruse, E. Amromin, J. Felmlee, J. Greenleaf, and R. Ehman, "Magnetic resonance elastography: Non-invasive mapping of tissue elasticity," *Medical Image Analysis*, vol. 5, no. 4, pp. 237–254, 2001.

[138] L. D. Marchi, N. Testoni, and N. Speciale, "Prostate tissue characterization via ultrasound speckle statistics," in *IEEE International Symposium on Signal Processing and Information Technology*, 2006, pp. 208–211.

[139] D. J. Marsh, J. L. Osborn, and A. J. Cowley, "1/f fluctuations in arterial pressure and regulation of renal blood flow in dogs," *The American Journal of Physiology*, vol. 258, no. 5, pp. F1394–400, 1990.

[140] S. McAleavey, S. White, and M. Menon, "Magnetically vibrated brachytherapy seeds: Ferromagnetic core models and image reconstruction methods," in *IEEE Ultrasonics Symposium*, 2006, pp. 1103–1106.

[141] M. M. Mohamed, T. K. Abdel-galil, M. A. Salama, E. F. Elsaadany, M. Kamel, A. Fenster, D. B. Downey, and K. Rizkalla, "Prostate cancer diagnosis based on gabor filter texture segmentation of ultrasound image," in *IEEE Canadian*

Conference on Electrical and Computer Engineering, vol. 3, 2003, pp. 1485–1488.

[142] S. S. Mohamed and M. M. A. Salama, "Computer-aided diagnosis for prostate cancer using support vector machine," in *SPIE Medical Imaging: Visualization, Image-Guided Procedures, and Display*, R. L. Galloway and K. R. Cleary, Eds., vol. 5744, 2005, pp. 898–906.

[143] M. Moradi, P. Mousavi, and P. Abolmaesumi, "Computer-aided diagnosis of prostate cancer with emphasis on ultrasound-based approaches: A review," *Ultrasound in Medicine and Biology*, vol. 33, no. 7, pp. 1010–1028, 2007.

[144] A. P. Moskalik, "Prostate cancer diagnosis and staging by sonography: Correlation of histopathologic measures with quantitative 3D Doppler ultrasound," Ph.D. dissertation, University of Michigan, Ann Arbor, MI, 2000.

[145] A. Moskalik, P. L. Carson, J. M. Rubin, R. L. Bree, J. B. Fowlkes, M. A. Rubin, K. Wojno, S. Manley, and J. E. Montie, "Analysis of three-dimensional ultrasound Doppler for the detection of prostate cancer," *Urology*, vol. 57, no. 6, pp. 1128–1132, 2001.

[146] U. G. Mueller-Lisse and M. Scherr, "1H magnetic resonance spectroscopy of the prostate," *Der Radiologe*, vol. 43, no. 6, pp. 481–488, 2003.

[147] Y. Murayama and S. Omata, "Fabrication of micro tactile sensor for the measurement of micro-scale local elasticity," *Sensors and Actuators A*, vol. 109, no. 3, pp. 202–207, 1997.

[148] J. Nakashima, A. Tanimoto, Y. Imai, M. Mukai, Y. Horiguchi, K. Nakagawa, M. Oya, T. O. K. Marumo, and M. Murai, "Endorectal MRI for prediction of tumor site, tumor size, and local extension of prostate cancer," *Urology*, vol. 64, no. 1, pp. 101–105, 2004.

[149] N. D. Nanayakkara and J. K. Samarabandu, "Automatic prostate boundary detection in ultrasound images using multiresolution deformable models and fuzzy logic," in *SPIE Conference on Image Processing: Algorithms and Systems II*, E. R. Dougherty, J. T. Astola, and K. O. Egiazarian, Eds., vol. 5014, 2003, pp. 290–296.

[150] P. A. Narayana and J. Ophir, "On the validity of the linear approximation in the parametric measurement of attenuation in tissues," *Ultrasound in Medicine and Biology*, vol. 9, no. 4, pp. 357–361, 1983.

[151] J. A. Noble and D. Boukerroui, "Ultrasound image segmentation: A survey," *IEEE Transcations on Medical Imaging*, vol. 25, no. 6, pp. 987–1010, 2006.

[152] D. A. Noe, *The Logic of Laboratory Medicine*, 1st ed. US: Urban and Schwarzenberg, 1985.

[153] S. M. Noworolski, R. G. Henry, D. B. Vigneron, and J. Kurhanewicz, "Dynamic contrast-enhanced MRI in normal and abnormal prostate tissues as defined by biopsy, MRI, and 3D MRSI," *Magnetic Resonance in Medicine*, vol. 53, no. 2, pp. 240–255, 2005.

[154] G. J. Odowd, M. C. Miller, R. Orozco, and R. W. Veltri, "Analysis of repeat biopsy results within one year after a noncancer diagnosis," *Urology*, vol. 55, no. 4, pp. 533–559, 2000.

[155] K. Okihara, H. Watanabe, and M. Kojima, "Kinetic study of tumor blood flow in prostatic cancer using power Doppler imaging," *Ultrasound in Medicine and Biology*, vol. 25, no. 1, pp. 89–94, 1999.

[156] S. Omata and C. E. Constantinou, "Modeling of micturition characteristics based on prostatic stiffness modulation induced using hormones and adrenergic antagonists," *IEEE Transactions on Biomedical Engineering*, vol. 42, no. 8, pp. 843–848, 1995.

[157] B. J. Oosterveld, J. M. Thijssen, P. C. Hartman, R. L. Romijn, and G. J. Rosenbusch, "Ultrasound attenuation and texture analysis of diffuse liver disease: methods and preliminary results," *Physics in Medicine and Biology*, vol. 36, no. 8, pp. 1039–1064, 1991.

[158] J. Ophir, I. Cespedes, H. Ponnekanti, Y. Yazdi, and X. Li, "Elastography: a method for imaging the elasticity in biological tissues," *Ultrasonic Imaging*, vol. 13, no. 2, pp. 111–134, 1991.

[159] S. Park, S. R. Aglyamov, and S. Y. Emelianov, "Elasticity imaging using conventional and high-frame rate ultrasound imaging: Experimental study," *IEEE Transactions on Ultrasonics, Ferroelectrics and Frequency Control*, vol. 54, no. 11, pp. 2246–2256, 2007.

[160] S. D. Pathak, V. Chalana, D. R. Haynor, and Y. Kim, "Edge-guided boundary delineation in prostate ultrasound images," *IEEE Transactions on Medical Imaging*, vol. 19, no. 12, pp. 1211–1219, 2000.

[161] H. Pauli and H. P. Schwan, "Mechanism of absorption of ultrasound in liver tissue," *Journal of the Acoustic Society of America*, vol. 50, no. 2B, pp. 692–699, 1971.

[162] C. Pellot-Barakat, F. Frouin, M. F. Insana, and A. Herment, "Ultrasound elastography based on multiscale estimations of regularized displacement fields," *IEEE Transactions on Medical Imaging*, vol. 23, no. 2, pp. 153–163, 2004.

[163] M. Perrotti, K. R. Han, R. E. Epstein, E. C. Kennedy, F. Rabbani, K. Badani, A. J. Pantuck, R. E. Weiss, and K. B. Cummings, "Prospective evaluation of endorectal magnetic resonance imaging to detect tumor foci in men with prior negative prostatic biopsy: a pilot study," *Journal of Urology*, vol. 162, no. 4, pp. 1314–1317, 1999.

[164] A. Pesavento, C. Perrey, M. Krueger, and H. Ermert, "A time-efficient and accurate strain estimation concept for ultrasonic elastography using iterative phase zero estimation," *IEEE Transactions on Ultrasonics, Ferroelectrics, and Frequency Control*, vol. 46, no. 5, pp. 1057–1067, 1999.

[165] A. Petrosian, "Kolmogorov complexity of finite sequences and recognition of different preictal EEG patterns," in *IEEE Symposium on Computer-Based Medical Systems*, 1995, pp. 212–217.

[166] J. C. Platt, *Advances in Large Margin Classifier.* Cambridge, MA: MIT Press, 2000, ch. Probabilistic outputs for support vector machines and comparison to regularized likelihood methods.

[167] T. C. Potdevin, A. P. Moskalik, J. B. Fowlkes, R. O. Bude, and P. L. Carson, "Doppler quantitative measures by region to discriminate prostate cancer," *Ultrasound in Medicine and Biology*, vol. 27, no. 10, pp. 1305–1310, 2001.

[168] A. Prando and A. Wallace, "Helical CT of prostate cancer: early clinical experience," *American Jouranl of Roentgenology*, vol. 175, no. 2, pp. 343–345, 2000.

[169] J. J. Prete, B. R. Prestidge, W. S. Bice, and D. F. D. L. A. Hotchkiss, "Comparison of MRI- and CT-based post-implant dosimetric analysis of transperineal interstitial permanent prostate brachytherapy," *Radiation Oncology Investigations*, vol. 6, no. 2, pp. 90–96, 1998.

[170] M. B. Priestley, *Spectral Anlysis and Time Series.* UK: Academic Press, 1981.

[171] S. S. Rao, *Mechanical Vibrations.* Reading, MA: Addison-Wessley, 1995.

[172] C. Rasch, I. Barillot, P. Remeijer, A. Touw, M. Van Herk, and J. V. Lebesque, "Definition of the prostate in CT and MRI: a multi-observer study," *International Journal of Radiation Oncology Biology Physics*, vol. 43, no. 1, pp. 57–66, 1999.

[173] M. D. Rifkin, *Ultrasound of the Prostate, Imaging in the Diagnosis and Therapy of Prostate Disease.* PA: Lippincott - Raven Publishers, 1997.

[174] H. Rivaz, E. Boctor, P. Foroughi, R. Zellars, G. Fichtinger, and G. Hager, "Ultrasound elastography: a dynamic programming approach," *IEEE Transactions on Medical Imaging*, 2008, in print, available online.

[175] H. Rivaz and R. Rohling, "A hand-held probe for vibro-elastography," in *Medical Image Computing and Computer Assisted Intervention*, ser. LNCS, J. Duncan, Ed., vol. 3749, 2005, pp. 613–620.

[176] M. J. Roobol, I. W. Van Der Cruijsen, and F. H. Schroder, "No reason for immediate repeat sextant biopsy after negative initial sextant biopsy in men with PSA level of 4.0 ng/ml or greater," *Urology*, vol. 63, no. 5, pp. 892–897, 2004.

[177] F. Rosenblatt, *Principles of Neurodynamics: Perceptions and the theory of brain mechanisms.* Washington: Spartan Books, 1962.

[178] D. E. Rumelhart, G. E. Hinton, and R. J. Williams, *Parallel Distributed Processing: Explorations in the Microstructure of Cognition.* MA: MIT Press, 1986, vol. 1, ch. Learning internal representations by error propagation, pp. 318–362.

[179] S. E. Salcudean, D. French, S. Bachmann, R. Zahiri-Azar, X. Wen, and W. Morris, "Viscoelasticity modeling of the prostate region using vibro-elastography," in *Medical Image Computing and Computer Assisted Intervention*, ser. LNCS, R. Larsen, M. Nielsen, and J. Sporring, Eds., vol. 4190, 2006, pp. 389–396.

[180] J. L. Sauvain, P. Palascak, D. Bourscheid, C. Chabi, A. Atassi, J. M. Bremon, and R. Palascak, "Value of power Doppler and 3D vascular sonography as a

method for diagnosis and staging of prostate cancer," *European Urology*, vol. 44, no. 1, pp. 21–31, 2003.

[181] H. Schder, , and S. M. Larson, "Positron emission tomography for prostate, bladder, and renal cancer," *Seminars in Nuclear Medicine*, vol. 34, no. 4, pp. 274–292, 2004.

[182] U. Scheipers, H. Ermert, H. J. S. M. Garcia-Schurmann, T. Senge, and S. Philippou, "Ultrasonic multifeature tissue characterization for prostate diagnosis," *Ultrasound in Medicine and Biology*, vol. 20, no. 8, pp. 1137–1149, 2003.

[183] U. Scheipers, A. Lorenz, A. Pesavento, H. Ermert, H. J. Sommerfeld, M. Garcia-Schurmann, K. Kuhne, T. Senge, and S. Philippou, "Ultrasonic multifeature tissue characterization for the early detection of prostate cancer," in *IEEE Ultrasonics Symposium*, 2001, pp. 1265–1268.

[184] U. Scheipers, C. Perrey, S. Siebers, C. Hansen, and H. Ermert, "A tutorial on the use of roc analysis for computer-aided diagnostic systems," *Ultrasonic Imaging*, vol. 27, no. 3, pp. 181–198, 2005.

[185] M. L. Schiebler, M. D. Schnall, H. M. Pollack, R. E. Lenkinski, J. E. Tomaszewski, A. J. Wein, R. Whittington, W. Rauschning, and H. Y. Kressel, "Current role of MR imaging in the staging of adenocarcinoma of the prostate," *Radiology*, vol. 189, no. 2, pp. 339–352, 1993.

[186] G. Schmitz, H. Ermert, and T. Senge, "Tissue-characterization of the prostate using radio frequency ultrasonic signals," *IEEE Transactions on Ultrasonics, Ferroelectrics and Frequency Control*, vol. 46, no. 1, pp. 126–138, 1999.

[187] F. H. Schroder, M. Roobolbouts, A. N. Vis, V. D. T. Kwast, and R. Kranse, "Prostate specific antigen based early detection of prostate cancer, validation of screening without rectal examination," *Urology*, vol. 57, no. 1, pp. 83–90, 2001.

[188] F. Schroeder and P. Boyle, "Screening for prostate cancer: Necessity or nonsense?" *European Journal of Cancer*, vol. 5, pp. 656–561, 1993.

[189] J. P. Sedelaar, T. E. B. Goossen, H. Wijkstra, and J. J. de la Rosette, "Reproducibility of contrast-enhanced transrectal ultrasound of the prostate," *Ultrasound in Medicine and Biology*, vol. 27, no. 5, pp. 595–602, 2001.

[190] D. Shen, Z. Lao, J. Zeng, H. Edward, H. G. Fichtinger, and C. Davatzikos, "A statistical atlas of prostate cancer for optimal biopsy," in *Medical Image Computing and Computer Assisted Intervention*, ser. LNCS, W. J. Niessen and M. A. Viergever, Eds., vol. 2208, 2001, pp. 416–424.

[191] D. Shen, Z. Lao, J. Zeng, W. Zhang, I. A. Sesterhenn, L. Sun, J. W. Moul, E. H. Herskovits, G. Fichtinger, and C. Davatzikos, "Optimized prostate biopsy via a statistical atlas of cancer spatial distribution," *Medical Image Analysis*, vol. 8, no. 2, pp. 139–150, 2004.

[192] D. Shen, Y. Zhan, and C. Davatzikos, "Segmentation of prostate boundaries from ultrasound images using statistical shape model," *IEEE Transactions on Medical Imaging*, vol. 22, no. 4, pp. 439–551, 2004.

[193] K. Shinohara, T. M. Wheeler, and P. T. Scardino, "The appearance of prostate cancer on transrectal ultrasonography: Correlation of imaging and pathological examination," *Journal of Urology*, vol. 142, no. 1, pp. 76–82, 1989.

[194] H. Shono, C. K. P. A. L. Goldberger, M. Shono, and H. Sugimori, "A new method to determine a fractal dimension of non-stationary biological time-serial data," *Computers in Biology and Medicine*, vol. 30, no. 4, pp. 237–245, 2000.

[195] O. Shvarts, K. R. Han, M. Seltzer, A. J. Pantuck, and A. S. Belldegrun, "Positron emission tomography in urologic oncology," *Cancer Control.*, vol. 9, no. 4, pp. 335–342, 2002.

[196] D. Singh, P. G. Febbo, K. Ross, D. G. Jackson, J. Manola, C. Ladd, P. Tamayo, A. A. Renshaw, A. V. D'Amico, J. P. Richie, E. S. Lander, M. Loda, P. W. Kantoff, T. R. Golub, and W. R. Sellers, "Gene expression correlates of clinical prostate cancer behavior," *Cancer Cell*, vol. 1, no. 2, pp. 203–209, 2002.

[197] D. G. Smith, S. R. Potter, B. R. Lee, H. W. Ko, W. R. Drummond, J. K. Telford, and A. W. Partin, "In vivo measurement of tumor conductiveness with the magnetic bioimpedance method," *IEEE Transactions on Biomedical Engineering*, vol. 47, no. 10, pp. 1403–1405, 2000.

[198] Y. Smith, G. Zajicek, M. Werman, G. Pizov, and Y. Sherman, "Similarity measurement method for the classification of architecturally differentiated images," *Computers and Biomedical Research*, vol. 32, no. 1, pp. 1–12, 1999.

[199] A. Sofer, J. Zeng, and S. K. Mun, "Optimal biopsy protocols for prostate cancer," *Annals of Operations Research*, vol. 119, no. 1–4, pp. 63–74, 2003.

[200] C. Stock, M. Hruza, J. Cresswell, and J. J. Rassweiler, "Transrectal ultrasound-guided biopsy of the prostate: Development of the procedure, current clinical

practice, and introduction of self-embedding as a new way of processing biopsy cores," *Journal of Endourology*, vol. 22, no. 6, pp. 1321–1329, 2008.

[201] R. Stotzka, R. Mnner, P. H. Bartels, and D. Thompson, "A hybrid neural and statistical classifier system for histopathologic grading of prostate lesions," *Analytical and Quantitative Cytology and Histology*, vol. 17, no. 3, pp. 204–218, 1995.

[202] R. C. Susil, K. Camphausen, P. Choyke, E. R. McVeigh, G. S. Gustafson, H. Ning, R. W. Miller, C. N. C. Ergin Atalar, and C. Menard, "System for prostate brachytherapy and biopsy in a standard 1.5 T MRI scanner," *Magnetic Resonance in Medicine*, vol. 52, no. 3, pp. 683–688, 2004.

[203] M. G. Swanson, D. B. Vigneron, Z. L. Tabatabai, R. G. Males, L. Schmitt, P. R. Carroll, J. K. James, R. E. Hurd, , and J. Kurhanewicz, "Proton HR-MAS spectroscopy and quantitative pathologic analysis of MRI/3D-MRSI-targeted postsurgical prostate tissues," *Magnetic Resonance in Medicine*, vol. 50, no. 5, pp. 944–954, 2003.

[204] A. Tabesh, V. P. Kumar, H. Y. Pang, D. Verbel, A. Kotsianti, M. Teverovskiy, and O. Saidi, "Automated prostate cancer diagnosis and gleason grading of tissue microarrays," in *SPIE Medical Imaging: Image Processing*, J. M. Fitzpatrick and J. M. Reinhard, Eds., vol. 5747, 2005, pp. 58–70.

[205] H. Takagi, M. J. Sato, T. Yanagida, and M. Ueda, "Functional analysis of spontaneous cell movement under different physiological conditions," *PLoS ONE*, vol. 3, no. 7, pp. 1–7, 2008.

[206] J. Tang, S. Li, J. Li, Y. Luo, J. Xu, Y. Zhang, X. Li, H. Shi, and G. Zhang, "Correlation between prostate cancer grade and vascularity on color Doppler imaging: preliminary findings," *Journal of Clinical Ultrasound*, vol. 31, no. 2, pp. 61–68, 2003.

[207] L. S. Taylor, B. C. Porter, G. Nadasdy, P. A. Santagnese, D. Pasternack, Z. Wu, R. B. Baggs, D. J. Rubens, and K. J. Parker, "Three-dimensional registration of prostate images from histology and ultrasound," *Ultrasound in Medicine and Biology*, vol. 30, no. 2, pp. 161–168, 2004.

[208] S. Theodoridis and L. koutroumbas, *Pattern Recognition*. San Diego, CA: Academic Press, 1999.

[209] P. Tiwari, A. Madabhushi, and M. Rosen, "A hierarchical unsupervised spectral clustering scheme for detection of prostate cancer from magnetic resonance spectroscopy (MRS)," in *Medical Image Computing and Computer Assisted Intervention*, ser. LNCS, N. Ayache, S. Ourselin, and A. Maeder, Eds., vol. 4792, 2007, pp. 278–286.

[210] S. Tong, D. Downey, H. N. Cardinal, and A. Fenster, "Three-dimensional ultrasound prostate imaging system." *Ultrasound in Medicine and Biology*, vol. 22, no. 6, pp. 735–746, 1996.

[211] G. R. Torr, "The acoustic radiation force," *American Journal of Physics*, vol. 52, no. 5, pp. 402–408, 1984.

[212] A. Tsai, A. Yezzi, W. Wells, C. Tempany, D. Tucker, A. Fan, W. E. Grimson, and A. Willsky, "A shape-based approach to the segmentation of medical imagery using level sets," *IEEE Transactions on Medical Imaging*, vol. 22, no. 2, pp. 137–154, 2003.

[213] M. J. F. Valckx and M. J. Thijssen, "Characterization of echocardigraphic image texture by coocurence matrix parameters," *Ultrasound in Medicine and Biolology*, vol. 23, no. 4, pp. 559–571, 1997.

[214] F. A. Van Dorsten, M. Van Der Graaf, M. R. W. Engelbrecht, G. J. L. H. Van Leenders, A. Verhofstad, M. Rijpkema, J. J. M. C. H. De La Rosette, J. O. Barentsz, and A. Heerschap, "Combined quantitative dynamic contrast-enhanced MR imaging and 1H MR spectroscopic imaging of human prostate cancer," *Journal of Magnetic Resonance Imaging*, vol. 20, no. 2, pp. 279–287, 2004.

[215] M. P. R. Van Gellekom, M. A. Moerland, J. J. Battermann, and J. J. W. Lagendijk, "MRI-guided prostate brachytherapy with single needle methoda planning study," *Radiotherapy and Oncology*, vol. 71, no. 3, pp. 327–332, 2004.

[216] V. N. Vapnik, *The Nature of Statistical Learning Theory.* NY: Springer, 1995.

[217] J. Veltman, T. E. B. Goossen, P. Laguna, H. Wijkstra, and J. de la Rosette, "New technical improvements for TRUS in the diagnosis of prostate cancer," *European Urology Supplements*, vol. 1, no. 6, pp. 8–14, 2002.

[218] J. T. M. Verhoeven and J. M. Thijssen, "Potential of fractal analysis for lesion detection in echocardiographic images," *Ultrasonic Imaging*, vol. 15, no. 1, pp. 304–323, 1993.

[219] S. Viswanatha, M. Rosenb, and A. Madabhushia, "A consensus embedding approach for segmentation of high resolution in vivo prostate magnetic resonance imagery," in *SPIE Medical Imaging: Computer-Aided Diagnosis*, M. L. Giger and N. Karssemeijer, Eds., vol. 6915, 2008, pp. 69 150U1–12.

[220] R. F. Wagner, S. W. Smith, J. M. Sandrik, and H. Lopez, "Statistics of speckle in ultrasound b-scans," *IEEE Transactions on Sonics and Ultrasonics*, vol. 30, no. 3, pp. 156–163, 1983.

[221] G. Wan, Z. Wei, L. Gardi, D. B. Downey, and A. Fenster, "Brachytherapy needle deflection evaluation and correction," *Medical Physics*, vol. 32, no. 4, pp. 902–909, 2005.

[222] Y. Wang, N. Cardinal, D. Downey, and A. Fenster, "Semi-automatic 3D segmentation of the prostate using 2d ultrasound images," *Medical Physics*, vol. 30, no. 5, pp. 887–897, 2003.

[223] M. Watanabe, K. Ohnishi, and H. Hayami, "Study on blood flow images in prostatic cancer during therapy by 2D-Doppler flow mapping," *Japanese Journal of Medical Ultrasound (Suppl. I)*, vol. 17, no. 1, pp. 443–444, 1990.

[224] N. Weidner, P. R. Carroll, J. Flax, W. Blumenfeld, and J. Folkman, "Tumor angiogenesis correlates with metastasis in invasive prostate carcinoma," *American Journal of Pathology*, vol. 143, no. 2, pp. 401–409, 1993.

[225] J. B. Welsh, L. M. Sapinoso, A. I. Su, S. G. Kern, J. Wang-Rodriguez, C. A. Moskaluk, H. F. Frierson, and G. M. Hampton, "Analysis of gene expression identifies candidate markers and pharmacological targets in prostate cancer," *Cancer Research*, vol. 61, no. 16, pp. 5974–5978, 2001.

[226] L. Weng, J. M. Reid, P. M. Shankar, and K. Soetanto, "Ultrasound speckel analysis based on the k distribution," *Journal of the Acoustic Society of America*, vol. 89, no. 6, pp. 2292–2295, 1991.

[227] L. A. Wirtzfeld, G. Wu, M. Bygrave, Y. Yamasaki, H. Sakai, M. Moussa, J. I. Izawa, D. B. Downey, N. M. Greenberg, A. Fenster, J. W. Xuan, and J. C. Lacefield, "A new three-dimensional ultrasound microimaging technology for preclinical studies using a transgenic prostate cancer mouse model," *Cancer Research*, vol. 65, no. 14, pp. 6337–6345, 2005.

[228] T. F. Wu, C. J. Lin, and R. C. Weng, "Probability estimates for multi-class classification by pairwise coupling," *Journal of Machine Learning Research*, vol. 5, no. 1, pp. 975–1005, 2004.

[229] S. Xu, J. Kruecker, P. Guion, N. Glossop, Z. Neeman, P. Choyke, A. K. Singh, , and B. J. Wood, "Closed-loop control in fused MR-TRUS image-guided prostate biopsy," in *Medical Image Computing and Computer Assisted Intervention*, ser. LNCS, N. Ayache, S. Ourselin, and A. Maeder, Eds., vol. 4791, 2007, pp. 128–135.

[230] K. K. Yu and H. Hricak, "Imaging prostate cancer," *Radiologic clinics of North America*, vol. 38, no. 1, pp. 59–85, 2000.

[231] J. Yuan and Y. Zhang, "Spectral analysis of combustion noise and flame pattern recognition," *Applied Statistics*, vol. 49, no. 4, pp. 509–515, 2000.

[232] A. Zaim, Y. Taeil, and R. Keck, "Feature-based classification of prostate ultrasound images using multiwavelet and kernel support vector machines," in *International Joint Conference on Neural Networks*, 2007, pp. 278–281.

[233] M. Zappa, "Over-diagnosis of prostate carcinoma by screening: An estimate based on the results of the Florence Screening Pilot Study," *Annals of Oncology*, vol. 9, no. 12, pp. 1297–300, 1998.

[234] Y. Zhan, M. Feldman, J. Tomaszeweski, C. Davatzikos, and D. Shen, "Registering histological and mr images of prostate for image-based cancer detection," in *Medical Image Computing and Computer Assisted Intervention*, ser. LNCS, R. Larsen, M. Nielsen, and J. Sporring, Eds., vol. 4191, 2006, pp. 620–628.

[235] Y. Zhan, Y. Ou, M. Feldman, J. Tomaszeweski, C. Davatzikos, and D. Shen, "Registering histologic and mr images of prostate for image-based cancer detection," *Academic Radiology*, vol. 14, no. 11, pp. 1367–1381, 2007.

[236] Y. Zhan and D. Shen, "Deformable segmentation of 3-D ultrasound prostate images using statistical texture matching method," *IEEE Transactions on Medical Imaging*, vol. 25, no. 3, pp. 256–272, 2006.

[237] Y. Zhan, D. Shen, J. Zeng, L. Sun, G. Fichtinger, J. Moul, and C. Davatzikos, "Targeted prostate biopsy using statistical image analysis," *IEEE Transactions on Medical Imaging*, vol. 26, no. 6, pp. 779–788, 2007.

[238] X. Zhang, M. Zeraati, R. R. Kinnick, J. F. Greenleaf, and M. Fatemi, "Vibration mode imaging," *IEEE Transactions on Medical Imaging*, vol. 26, no. 6, pp. 843–852, 2007.

[239] M. Zhou and C. Magi-Galluzzi, *Genitourinary Pathology*, ser. Foundations in Diagnostic Pathology Series. NY: Elsevier, 2006.

[240] Y. Zhu, S. Williams, and R. Zwiggelaar, "Computer technology in detection and staging of prostate carcinoma: A review," *Medical Image Analysis*, vol. 10, no. 2, pp. 178–199, 2006.